/
Article / Book Information

( )	
Title(English)	Evaluation of Experimental Full-Scale Steel Building Collapse Caused by Two-Directional Column Deteriorations
( )	TRAN TUAN NAM
Author(English)	TRAN TUAN NAM
( )	: , : , : 10204 , :2016 3 26 , : , : , , , ,
Citation(English)	Degree:, Conferring organization: Tokyo Institute of Technology, Report number: 10204 , Conferred date:2016/3/26, Degree Type:Course doctor, Examiner:,,,,
( )	
Type(English)	Doctoral Thesis

TOKYO INSTITUTE OF TECHNOLOGY

INTERDISCIPLINARY GRADUATE SCHOOL OF SCIENCE AND ENGINEERING

DEPARTMENT OF BUILT ENVIRONMENT

Evaluation of Experimental Full-Scale Steel Building Collapse Caused by Two-Directional Column Deteriorations

Tran Tuan Nam

Academic advisor: Prof. Kazuhiko Kasai

Dissertation submitted for the degree of

Doctor of Engineering

January 2016

ACKNOWLEDGEMENTS

CONTENTS

CHAPTER 1

INTRODUCTION

Chapter 1

INTRODUCTION

1.1 Collapse test of full-scale steel building

In September 2007, a full-scale four-story steel building was tested to collapse using strong ground motions at E-Defense, the world's largest three-dimensional shake table located in Miki City, Hyogo Prefecture, Japan. This test was a part of an experimental project focused on steel buildings conducted at the E-Defense shake table facility [1]. Some seismic collapse experimental projects on steel structures were previously conducted; however, only the pseudo-dynamic loading was applied [2], or a planar small scaled frame specimen was tested [3]. The objectives of this E-Defense collapse test were to evaluate the structural and functional performance of the full-scale steel building under the dynamic input of three-directional ground motions.

The building was designed following current Japanese specifications and practices (post 1995 Kobe earthquake). As a result of recently adopted improvements, there is a small likelihood that moment connections would fracture even under exceedingly large ground motions. However, strain hardening in the beam plastic hinges could increase story shear forces, which in turn increases the forces developed in the columns. If the columns are not designed for the increased forces, i.e., if the width-to-thickness ratio of the cross section is not sufficiently small to resist the increased forces, then local buckling could occur in the columns. Strength deterioration in lower story columns could shift the control mechanism of the frame from the overall sway mechanism to a soft-story collapse mechanism. Based on these conditions and detailed investigations [4], a soft-story collapse mechanism originating from

the deterioration in column strength was analytically identified as the most likely scenario for collapse of a moment frame constructed according to the current Japanese seismic code. Therefore, the building specimen was expected to show this type of collapse mechanism. The ground acceleration histories recorded at the JR Takatori station during the 1995 Hyogo-ken Nanbu earthquake [5] were used as the input for the shake table experiments at various scales (herein referred to as Takatori motion). The experimental results show that a soft-story collapse mechanism occurred as expected under the 100% Takatori motion due to local buckling and leading to the deterioration of columns in the first story.

1.2 Background of study

The experimental structural responses of the building specimen under the weak, strong and collapse shaking levels were formerly reported in [6–8], and non-structural responses observed in the test were particularly described in [9]. On the other hand, the experiment has attracted interest from research and practice communities [10–16] in studying and establishing an effective model to simulate the collapse behavior of the building specimen. Some other researchers [17–18] conducted a synthesis of experimental and analytical studies to evaluate the collapse response.

Two-dimensional (2D) numerical methods were adopted by Maison *et al.* [17] and Lignos *et al.* [18]. They closely simulated the history of the displacement component in the longitudinal direction of the frames that developed the largest responses. Those approaches both considered column deterioration after buckling, but the reduction of yield moment capacity due to varying axial force was not considered. However, in fact, the seismic building overturning moment can increase compression force in columns, which should adversely affect the yielding strength as well as the deteriorating capacity. Although the global responses in one direction (*i.e.* the collapse direction) can be closely simulated by those models, the two-directional responses of local members cannot be properly simulated or reflected.

Detailed three-dimensional (3D) finite element models for the column, therefore, would be more appropriate, since test results indicated large seismic compression force up to about 0.4 times the axial yield capacity. Tada *et al.* [11] utilized the Collaborative Structural Analysis system to conduct pseudo 3D analyses by combining 2D frames, where the local buckling region was modeled in detail by the finite element analysis program MARC. Pan *et al.* [12] discretized the members by numerous finite elements and used ABAQUS. As other finite element approaches, Miyamura *et al.* [13] used E-Simulator, and Isobe *et al.* [14] used an adaptive ASI-Gauss finite element code.

The detailed finite element methods mentioned above require large modeling and computational efforts, and may not be needed for the most of structural components responding elastically or even inelastically as long as simpler analysis techniques are available. The methods are also very inconvenient for estimation of member forces or sectional forces, essential for designing or evaluating. For these reasons, the approach combining finite elements with simple fiber beam elements would be an attractive choice, such as Yu *et al.* [15] and Chen *et al.* [16]. The element for the column was formulated to simulate local buckling and consequent degradation. PISA3D and OpenSEES were used, respectively.

1.3 Objective of study

In order to understand the experimental collapse behavior, it is necessary to study local responses and deteriorations of members subjected to biaxial bending, and relate them with different stages of the global responses including the progress and mechanism of collapse. All of the analytical studies indicated that the local buckling of columns governed the building collapse. However, most of them focused on the accuracy of simulating time histories and peaks of global responses, but did not report the physical aspect of local buckling except for Tada *et al.* [11] and Yu *et al.* [15], who showed deteriorating behavior of one selected column.

Furthermore, the experimental studies focused on the physics of collapse behavior. Maison *et al.* [17] evaluated the collapse response on global perspective only. Yamada *et al.* [7] and Shimada *et al.* [8] examined local behavior of beams, panel zones and columns, and discussed the deterioration of columns by local buckling as well as the interaction of the varying column axial force and biaxial bending moment. Out of six columns, the studies selected to discuss two members developing smaller magnitudes and variations of axial forces compared with the corner columns.

This study thereby attempts to identify the plastification progress occurring in the frame at different shaking levels and subsequently recognize weakened elements. Different deteriorating processes of all six first-story columns which carried the largest, moderate or smallest axial forces that are either compression or tension loads as well as correspondingly different shear forces are compared and clarified in detail. Moreover, the columns were subjected to a major few cycles in a particular direction and later to the largest cycle in a significantly rotated direction, and their consequent progress of two-directional deteriorations will be discussed in the study. In addition to the discussion on total earthquake input energy after Shimada *et al.* [8], this study further explores the building response in terms of instantaneous input energy, because a large amount of which could result in a sudden large response velocity and consequently a rapid increase of story displacement, thereby causing the structural collapse.

On the other hand, in order to establish an effective model to analyze the experimental behavior of the building specimen, this study utilizes a simplified analytical technique considering the so-called "fiber hinge element" to simulate steel column local buckling. Fundamental studies on fiber beam element approaches to simulate local buckling were previously reported. For instance, Uriz *et al.* [19] modeled buckling behavior of steel braces using the formulation by Spacone *et al.* [20]. Similar approaches were also taken by Liang *et al.* [21], Hajjar *et al.* [22], Varma *et al.* [23], and Uy [24], who proposed the prediction rules for buckling strength of concrete-filled steel tube

columns in relation with width-to-thickness b/t ratios. However, the rules were on member buckling strength, not the post-buckling degradation. In contrast, Kunnath *et al.* [25] after Monti and Nuti [26] developed a phenomenological material model in conjunction with fiber section implicitly including geometric effects of longitudinal re-bar buckling in an RC member. In their approach, the ratio of tie spacing and bar diameter was a key parameter to characterize the re-bar hysteresis degradation.

In this study, a phenomenological fiber hinge model is developed to simulate biaxial bending of a steel tube column, based on calibrations considering the column's experimental response, existing prediction rule for local buckling of steel stub columns, and FEM analysis. This approach would be in the same category as for the phenomenological material model mentioned above, but uses b/t ratio of steel tube column section. Because the concentrations of plasticity and local buckling occur at the ends of frame members, the fiber hinge element is used only at the column ends, unlike the fiber beam element approaches [19–25] discretizing the column section throughout the member length. The fiber hinge element has zero length but considers a yield-zone length for the fiber to simulate elastoplastic and local buckling behaviors. Other portions of the frame are modeled by the beam, truss, and spring elements.

The main objective of the study is to clarify two-directional column behavior and deteriorations, as well as consequent three-dimensional collapse of the full-scale four-story steel building via analyses utilizing the fiber hinge elements. The columns were under varying axial load and biaxial bending moment, deteriorating due to local buckling, and causing collapse of the building.

Accuracy of the analysis method is demonstrated via nonlinear dynamic simulations of the isolated column element as well as the four-story building considering small to large excitations as explained earlier. The fiber hinge element is extremely efficient and accounts for accumulated column damage

based on the strain history of each fiber. The analysis using the element simulates closely the column behavior due to the axial load and biaxial bending moment whose relative magnitude differing considerably by the locations of the column. Moreover, the analysis results interpret different deterioration patterns of the columns and effects of complex loading such as compression and tensile axial load applied alternately, additional high frequency axial load caused by vertical accelerations, and the cycle-by-cycle shifting of the bending moment's principal direction. Unlike the past analytical studies mainly focusing on global behavior, this study clearly shows comparison between the simulated and experimental responses of local frame members.

1.4 Scope of study

In Chapter 1, the study background, objective and scope were presented. The remainder of the dissertation is organized as follows.

- Chapter 2 introduces an overview of the building specimen and input ground motion considered in the test. The change of building dynamic properties at various shaking levels is discussed, whereby the local plastifications of frame components as well as the softening of the bolted column base due to column uplift are clarified. Also, the progress of two-directional soft-story collapse mechanism is summarized and visualized by absolute displacement orbit.

- Chapter 3 details the deteriorating and damaging sequence of all six first-story columns during collapse excitation level. This chapter also interprets the building responses in terms of energy input and dissipation, thereby suggesting the importance of instantaneous input energy in seismic design and structural evaluation.

- Chapter 4 explains the methodology of simulating two-directional column deteriorations by adopting fiber hinge element. The factor calibration for

modeling fiber properties is presented. This chapter also demonstrates several cyclic column analyses using some proposed biaxial loading patterns together with constant axial load. Some other complex loading schemes such as compressive and tensile axial load applied alternately, with additional high frequency axial load caused by vertical accelerations, as well as the cycle-by-cycle shifting of the bending moment's principal directions are also presented in this chapter.

- Chapter 5 describes the agreement between the simulated global/local and corresponding experimental responses throughout small to large and collapse excitation levels, achieved on variety of quantities such as story drift ratios, accelerations, base shear, energy dissipation, progress of local deterioration in the first-story columns and global soft-story collapse mechanism. The study also predicts some hypothetical responses of the building which were not tested or measured in the experiment.

- Chapter 6 characterizes for cyclic deteriorations of columns and soft story, on some aspects such as moment-deformation hysteresis shape, two-directional correlative deteriorations, effect of varying axial load condition, and soft story behavior governed by columns.

- Chapter 7 summarizes and concludes the study.

CHAPTER 2

BUILDING RESPONSES AT VARIOUS EXCITATION LEVELS

Chapter 2

BUILDING RESPONSES AT VARIOUS EXCITATION LEVELS

2.1 Building specimen

- The building specimen [Figure 2.1(a)] is a full-scale four-story steel moment frame whose plan dimension is 6 ×10 m, and the total height from the upper surface of the stiff foundation to the roof is 14.375 m [Figure 2.1(b)]. The total weight of the building is 2,019 kN.

- SN400B and BCR295 steel were used for the beams and columns, respectively. The section shapes and material properties are given in Tables 2.1 and 2.2, respectively. ALC (autoclaved lightweight concrete, designated as autoclaved aerated concrete in the US) external cladding panels were placed on three sides of the structure.

- The frame should remain elastic and the story drift ratio should be less than 1/200 for Level-1-designed earthquake loads, which is equivalent to a base shear coefficient of 0.2. At the plastic collapse state of the frame, the base shear coefficient according to static pushover analyses [6] is approximately 0.5 in both the X and Y directions, *i.e.* greater than 0.3 to meet the requirement of Level 2 design.

- The columns are constructed using cold-formed square tubes 300×300×9 with relatively large width-to-thickness ratios (b/t = 33). They are permitted by the code but with a tolerance of 20% increased design

seismic load to compensate for the increased likelihood of local buckling and consequent strength degradation in the columns. The post-collapsed configuration of the building specimen and the damage due to local buckling at column end in the first story level are shown in Figures 2.1(c)–(d), respectively.

- The columns are welded to 50-mm-thick baseplates (SN490C). Each baseplate is bolted using 8 anchor bolts of M36 (ABR490, 900 mm length) to fixtures attached to the shake table [Figure 2.1(e)]. A pretension force of approximately 100 kN (30% yield axial force) is applied to each anchor bolt. The design strength of the column base connection when under compression load is between 1.3 and 1.8 times the design strength of the columns. Moreover, the behavior of the column base should depend on not only compressive axial load but also tension load, which should significantly reduce the column base moment capacity. In addition, the behavior also depends on the relative strength of the column section, which should reflect the effects of the axial force. These are discussed using the test results later in this work (Section 2.3.3).

- The beams are constructed using hot-rolled wide flanges. Welding details with no weld access hole, which were recommended after the Kobe earthquake [27], are adopted for the beam-to-column connections [Figure 2.1(f)]. This is a premium detail used to ensure the ductile deformation capacity and strain hardening of the beams.

- The metal decks are connected to the beams through studs that are welded to the beam top flanges. Wire meshes are placed above the metal deck sheets, and concrete is placed on site. Fully composite action is expected between the steel beams and the concrete slab.

- The strong column–weak beam philosophy is employed. Specifically, at each story, the summation of the design column strength is greater than either 1.5 times the summation of the design strength of the beams or 1.3 times the summation of the design strengths of the panel zones.
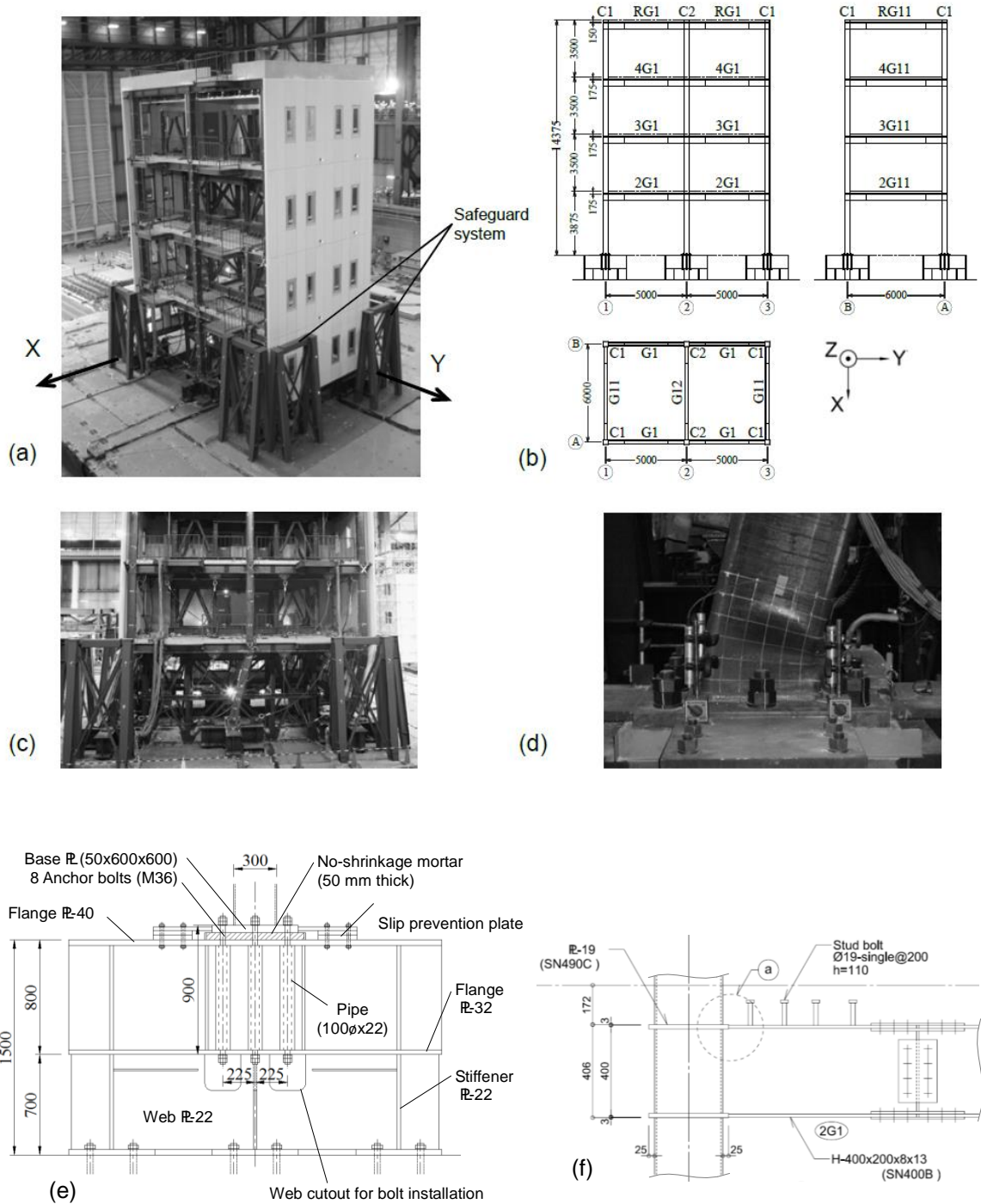
Figure 2.1 Building specimen: (a) overview, (b) elevation and plan, (c) post-collapsed configuration, (d) hinging of first-story column ends at 100% Takatori motion level due to local buckling, (e) column base detail, and (f) beam-to-column panel zone.

Table 2.1 Sections and materials of the steel frame

| Beam (SN400B) | | | | Column | |
Floor	G1	G11	G12	Story	C1,C2
R	H-346×174×6×9	H-346×174×6×9	H-346×174×6×9	4	RHS-300×300×9
4	H-350×175×7×11	H-350×175×7×11	H-340×175×9×14	3	RHS-300×300×9
3	H-396×199×7×11	H-400×200×8×13	H-400×200×8×13	2	RHS-300×300×9
2	H-400×200×8×13	H-400×200×8×13	H-390×200×10×16	1	RHS-300×300×9

H- height × width × web thickness × flange thickness   RHS- height × width × thickness

Table 2.2 Material properties by coupon test (unit: MPa)

	Yield stress		Tensile strength	
Base plate (PL-50)	378		501	
Anchor bolt (M36)	336		507	
Column 2~4 story RHS-300×300×9	332		419	
Column 1,4 story RHS-300×300×9	330		426	
Beam	**Flange**	**Web**	**Flange**	**Web**
H-340×175×9×14	309	355	443	468
H-346×174×6×9	333	382	461	483
H-350×175×7×11	302	357	441	466
H-390×200×10×16	297	317	451	458
H-396×199×7×11	311	369	460	486
H-400×200×8×13	326	373	454	482

The safeguard system used to protect the shake table from damage during the collapse test consists of diagonal wires attached to the perimeter frame of the first and second stories to prevent inter-story drift beyond 1/3.5 rad. Moreover, the supporting tables were placed on the floor slab of each story to support the upper floor slab from dropping, wherein a 200-mm vertical gap was reserved between the supporting table surface and the bottom beam flange of the upper floor. In addition, a surrounding fence [shown in Figure 2.1(a)] was used to prevent the first-story drift ratio from exceeding 0.02 rad at the collapse state.

Regarding measurement system, the structure was densely instrumented with three-dimensional accelerometers, strain gauges and displacement transducers, which collected adequate data for a full characterization of the response history and dynamic characteristics of the building specimen. Moreover, a system of three-dimensional displacement transducers was also

instrumented to measure extremely large story drifts during collapse (see [6] and [8] for detailed descriptions of the sensor allocation layout).

2.2 Input ground motion

During the shaking experiment, the building specimen was subjected to a series of white noise motions and progressively increasing scaled Takatori motion from 5 to 100%. The EW, NS, and UD components of the ground motion were considered for the X, Y, and Z directions, respectively, and are plotted in Figure 2.2(a).

The elastic response pseudo-acceleration spectra [Figure 2.2(b)] mostly envelope a Maximum Considered Earthquake (MCE) that is the usual basis of collapse safety checks in the western United States. The pseudo-acceleration spectra are almost equal to the MCE spectrum at periods of 0.76 and 0.80 sec, i.e., the fundamental periods of the building in the Y and X directions, respectively [6].

Figure 2.2(c) contrasts the elastic response displacement spectra, represented by solid lines, with the inelastic response displacement spectra based on the present building strength, represented by broken lines. Note that two types of design yield strengths of $0.5\,W$ and actual strength, according to experimental results, of $0.65\,W$ (where W is the building weight) are applied for the inelastic spectra. Between 0.7 and 1.0 sec, the elastic response displacement spectra in both the X and Y directions are similar. However, the inelastic displacement spectrum in the Y direction becomes much greater than that in the X direction and also remarkably larger than its elastic displacement spectrum. A very large story drift displacement is expected in the Y direction. Accordingly, the ground motion applied to the present specimen may be substantially more damaging in the Y direction compared to the elastic structure, thus suggesting the likely collapse direction along the Y direction.
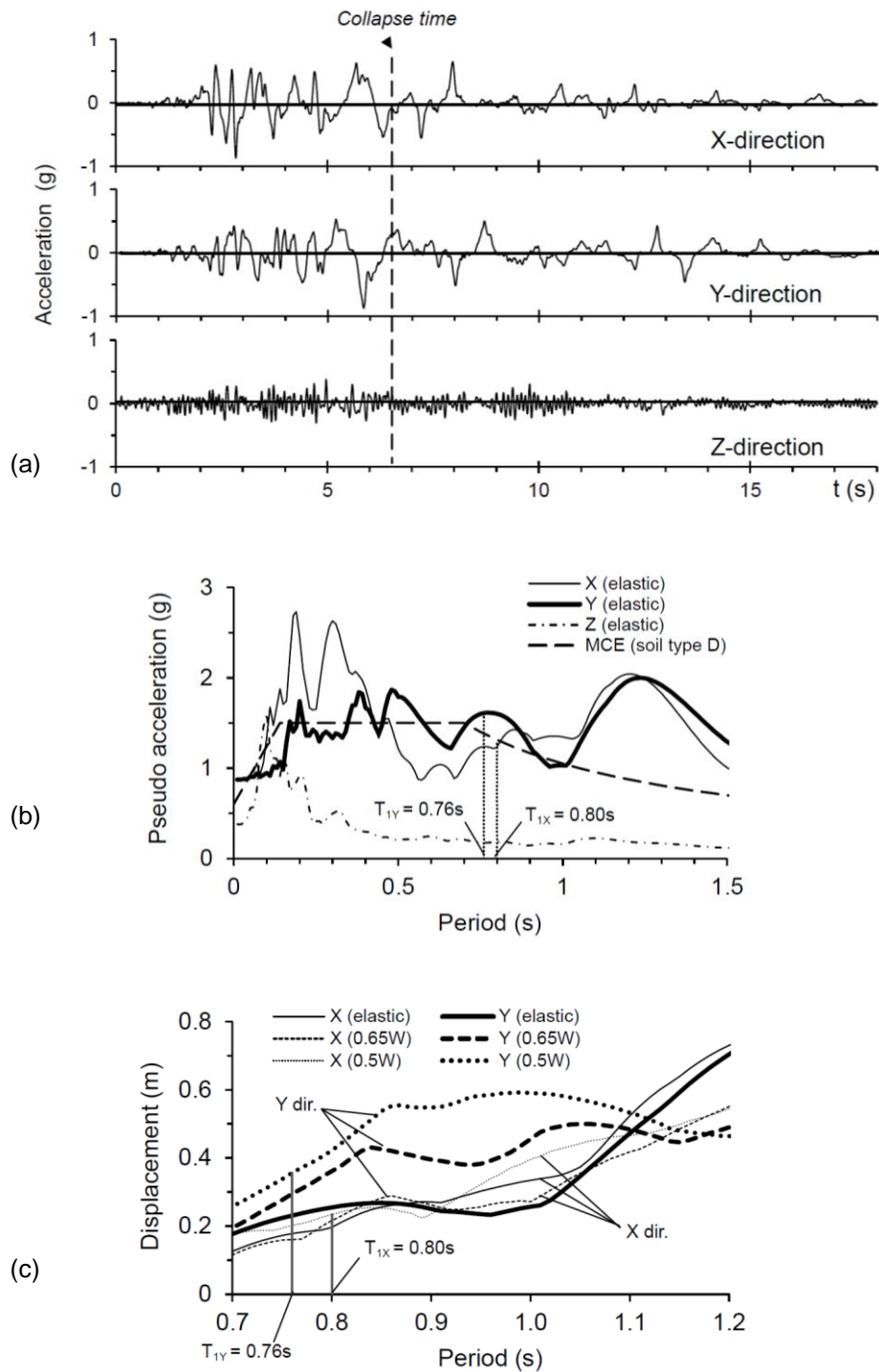
Figure 2.2 (a) Time-histories of input accelerations, (b) elastic pseudo acceleration spectra, (c) elastic vs. inelastic displacement spectra for 100% Takatori motion at 5% damping (inelastic model: yield strength = 0.5W and 0.65W, where W is the building weight).

## 2.3 Effect of local plastifications on building dynamic properties

2.3.1 Dynamic building properties at various shaking levels

The building survived excitations having scale factors up to 60% and collapsed at 100% Takatori motion level via a soft-story mechanism in the first story. This section focuses on the four cases of 20, 40, 60 and 100% Takatori motion levels. The dynamic properties of the building at each excitation level were obtained based on the frequency-domain method by Kasai *et al.* [28] using an appropriate transfer function between the horizontal and vertical accelerations of each story and the horizontal and vertical accelerations, including the inevitable rocking response of the shake table. The identification results for the building's elastic response at 20% Takatori motion is illustrated in Figure 2.3, where the natural periods in the X direction (T_{1X}) and in the Y direction (T_{1Y}) are found to be 0.825 and 0.776 sec, respectively. The natural period for the Z direction, not shown in the figure, is found to be 0.095 sec.

This method is applied to other tests to characterize the increasing trend of the natural periods and damping ratios with increasing excitation level [Figures 2.4(a)–(b)]. The natural period and damping ratio (identified using a free vibration test before main excitation) are also included in the trend curves. In response to small shaking levels, T_{1Y} was smaller than T_{1X}. However, as the building experiences higher excitation levels, T_{1Y} increases more significantly than does T_{1X} and gradually becomes almost equal to T_{1X} (as shown in Figure 2.4(a), T_{1Y}=0.888 sec and T_{1X}=0.897 sec at 60% Takatori motion level). Figures 2.5(a)–(b) show the normalized amplitude of the story modal drift displacement of the first mode in the X and Y directions. Modal drift amplitudes of the first story in the Y direction increase remarkably at the 60% Takatori motion level, suggesting the dominant yielding along the Y direction, wherein a concentration is observed at the first story.
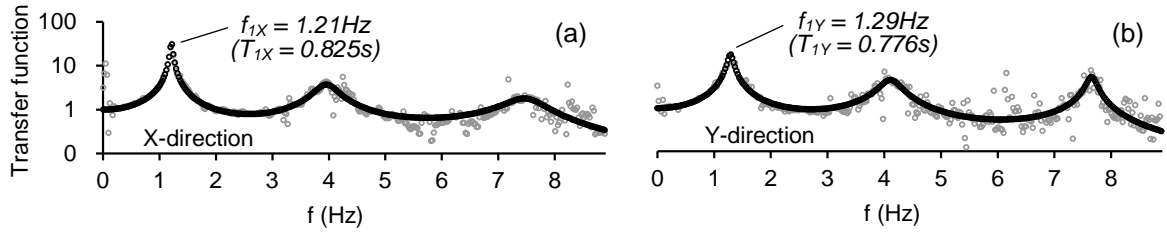
Figure 2.3 Empirical transfer function amplitude derived from accelerations at roof and shake table levels in the (a) X and (b) Y directions (20% Takatori level).
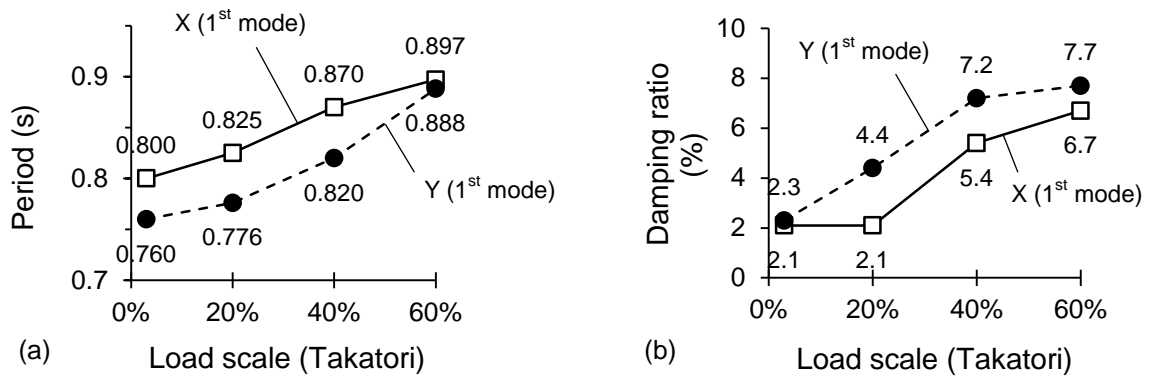
Figure 2.4 (a) Natural period and (b) damping ratio identified using curve-fitting method.
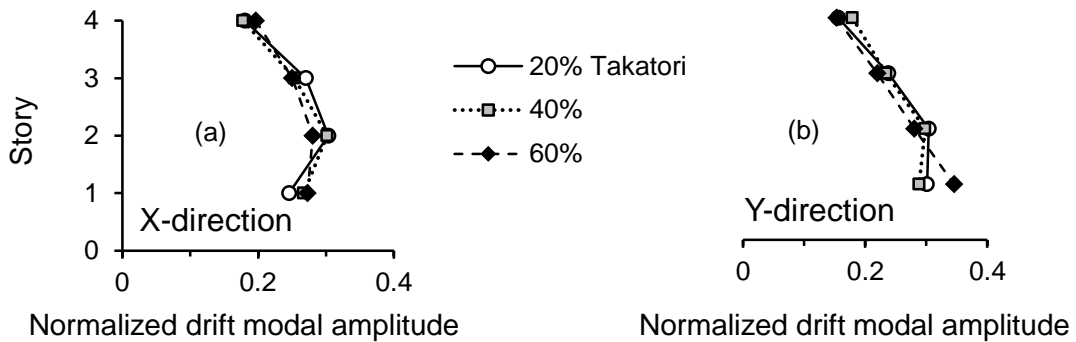
Figure 2.5 Normalized modal story drift identified using curve-fitting method (1st mode).

2.3.2 Plastification of frame components in the first story

To clarify the dominant yielding in the Y direction identified above, Figure 2.6 shows the frame moment diagram of two longitudinal frames at 6.05 sec for the 60% Takatori test when the first-story drift ratio reached a peak value of 0.02 rad in the Y direction. The two longitudinal frames along lines A and B [Figure 2.1(b)] are denoted as 'frame A' and 'frame B', respectively. The member moments are obtained in the same way as described in previous references [6–8]. The equilibrium error at the frame joints is less than 10% of the counteracting moments. The ratio of each member moment to its corresponding plastic moment, such as M_{pc}, M_{pp} and M_{pb} for *columns, panel zones* and *bare beams*, respectively, is also indicated. Note that M_{pc} corresponds to the case without axial forces. Columns in the second story showed moment ratios significantly below 1.0, meaning that they were elastic even under the axial force to be discussed later. An inelastic response was observed mostly by the column bottom ends and panel zones in the first story.

A full picture of the plastification of the first-story frame components with increasing shaking levels is given in Figure 2.7. At each shaking level, the peak moments M_X of the following members are plotted: six panel zones, six column top ends, six column bottom ends, four beam ends close to exterior joints and four beam ends close to interior joints [Figures 2.7(a)–(e)]. The solid lines and white symbols represent components of frame A, whereas the broken lines and gray symbols represent members of frame B. Four beams located on frames A and B, namely, A1-2, A2-3, B1-2 and B2-3, as shown in the floor plan view, are considered. Note that the letter A or B in the beam name indicates the line that the beam lies along, and the digits (e.g., 1-2) indicate the two ends of each beam.

The moments of all columns were similar up to the 60% Takatori motion level. When increased to 100% and prior to the building's collapse, the moments at the top ends of columns B2 and B3 decrease, whereas others

continued to increase [Figure 2.7(b)]. The moments at the bottom ends, however, decreased for all columns [Figure 2.7(c)]; in particular, the column bottom moments of frame B (represented by the broken lines) degraded more significantly than did those of frame A (solid lines). Note also that the bottom moment of column A1 at small excitation levels was much smaller than those of other columns due to the largest tension force and consequent softening of column base connection, which will be discussed in Section 2.3.3.

The panel zones yielded very early from the 40% Takatori motion level and deformed significantly at the 60% Takatori level [Figure 2.7(a)], where all panel zone moments, defined as panel shear force times the panel depth, exceeded M_{pp}, and the peak shear strain of the interior panel zone was 0.012 rad, i.e., approximately 2/3 of the peak r_Y. In contrast to the panel zones, all of the beam ends near interior joints were elastic throughout the tests [Figure 2.7(e)]. The moments of the beam ends near exterior joints [Figure 2.7(d)] are larger because only one beam resists moments transmitted from the columns.

This larger moment, however, was not large enough to cause beam yielding under positive bending because the beam's positive bending strength due to the composite action of the concrete slab $M_{pb,com}$ is 1.51 times the bare beam strength M_{pb} (further discussions on experimental behavior of composite beams are given in Appendix B). The most widely observed trend in all of the curves of the beams and panel zones is that the moment magnitudes of every component increased progressively from 20 to 60% Takatori motion levels but then stopped increasing at the 100% Takatori motion level due to column strength degradation, as mentioned above.

In summary, plastification in the first story occurred at columns and panel zones rather than at beams. In particular, panel zones were the earliest plastified components in the frame at the 40% Takatori level. During the response at the 60% Takatori level, a mechanism based on the yielding of panel zones and column bases at the first story was observed, leading to the soft-story collapse scenario at 100% Takatori motion level.
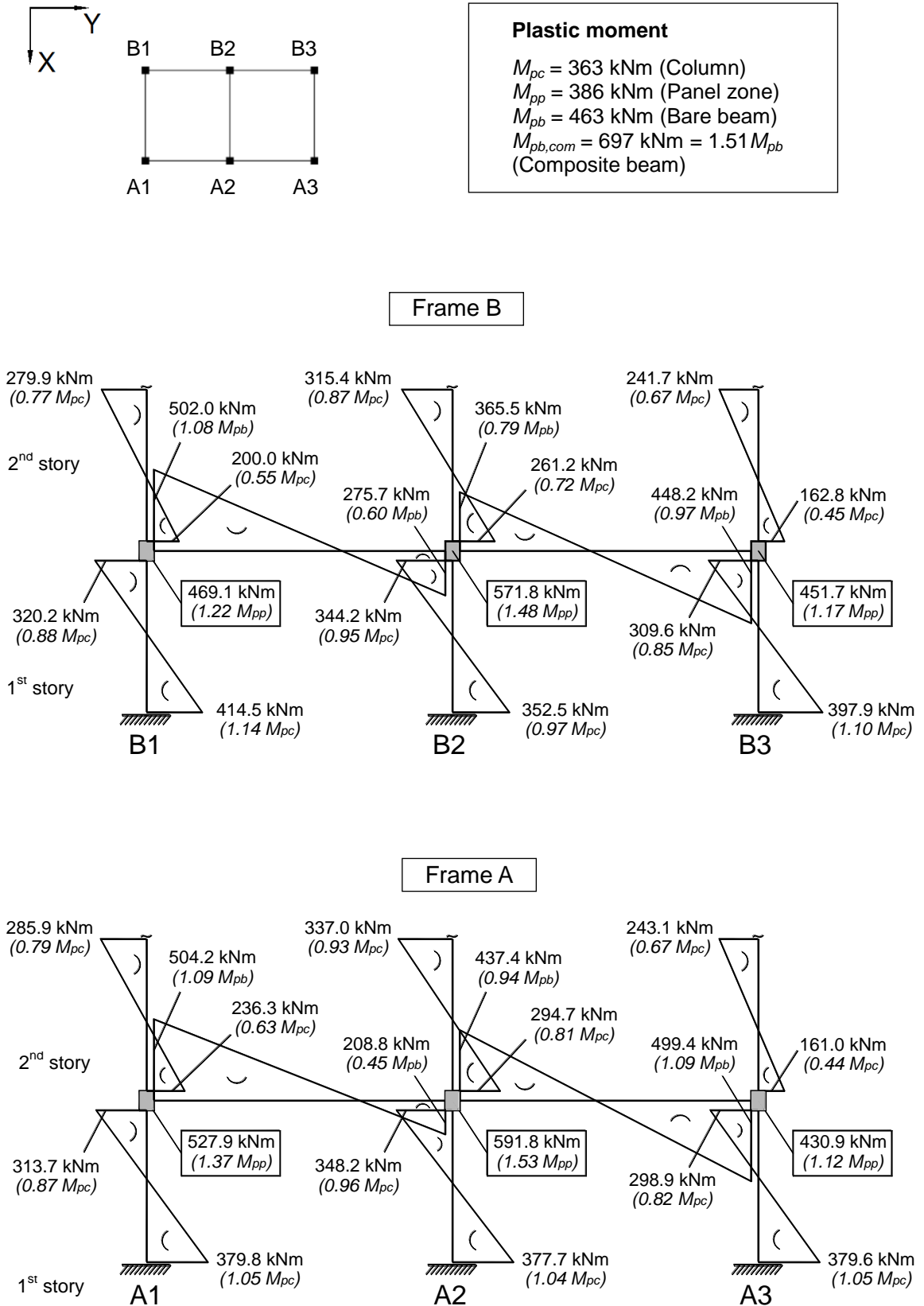
Figure 2.6 Frame moment diagram (at peak first-story drift, 60% Takatori)
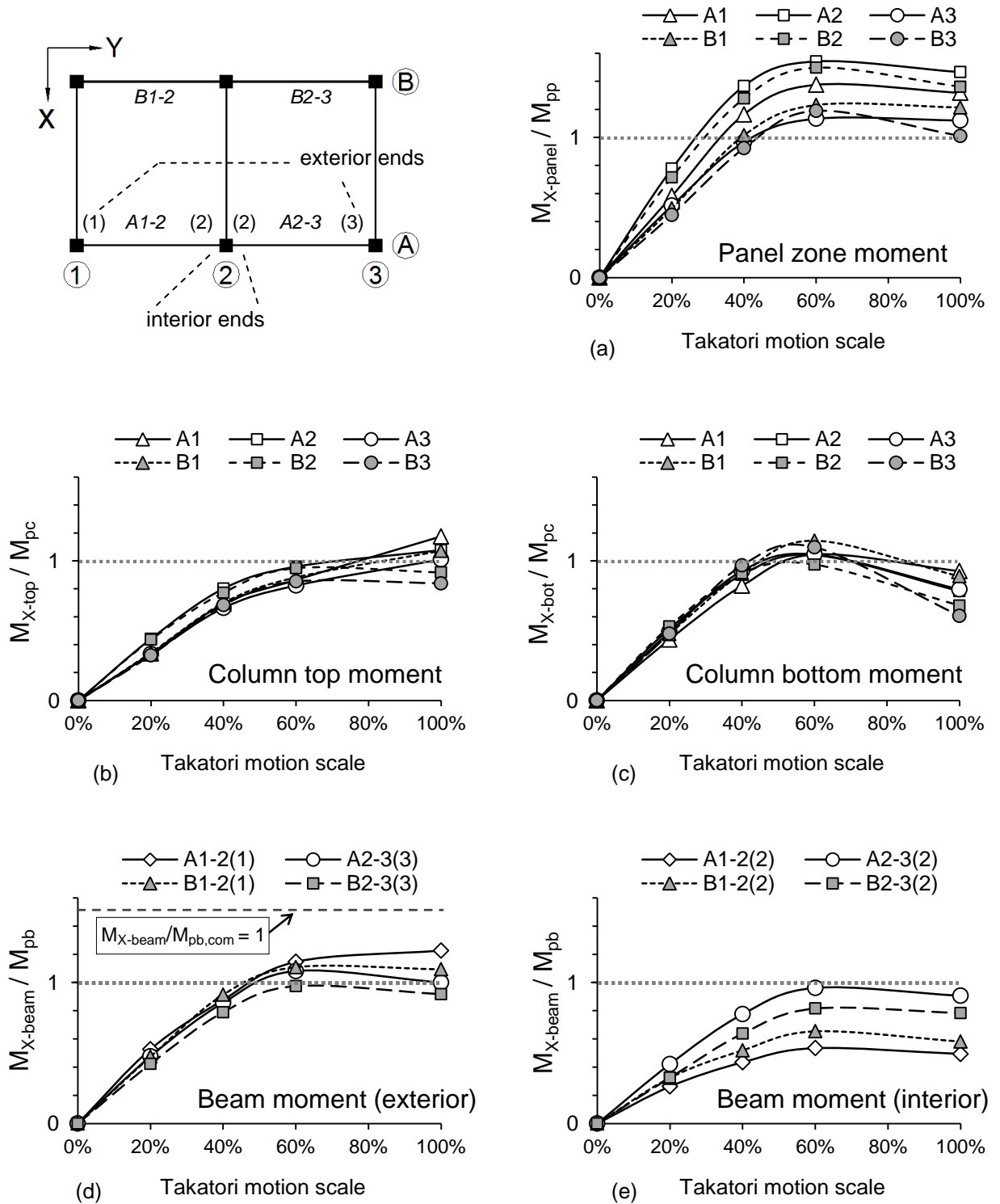
Figure 2.7 Peak normalized moment in columns, panel zones and beams

2.3.3 Softening of bolted column base due to column uplift

The design of the column base connection was simplified by ignoring several important factors, as suggested in Section 2.1. One of the important factors is the effect of the tension load produced by the seismic overturning moment, especially at the exterior corner columns. The time histories of the axial forces of corner columns A1 and B3 for the 60% Takatori motion level are selected and plotted in Figure 2.8(a) because the seismic axial forces, excluding the gravity load effect, were the largest in those columns due to the major direction of story drift oriented diagonal in plan, as will be presented in Section 2.4.

In the building vibration history, alternating fluctuations were observed for each half cycle, with peak values varying from $-0.26N_y$ to $+0.27N_y$ and from $-0.31N_y$ to $+0.28N_y$ for columns A1 and B3, respectively, where positive N indicates tension and $N_y = 3366$ kN is the column yield axial force. Note that the column axial force fluctuated as a result of not only the overturning moment but also the vertical response acceleration with a period of approximately 0.01 sec, which is equal to the building's natural period in the Z direction.

The time histories of the bending moments at the bottom of those two columns are plotted in Figure 2.8(b). The moment histories were very similar, except for local differences at peaks, thus suggesting the effect of base softening, as will be explained later. Because the story displacement was mainly oriented diagonal in plan with an orientation angle of approximately 45° with respect to the +Y-axis (Section 2.4), the *base plate rotational angle, first-story drift ratio,* and *column bottom moment* with respect to the axis oriented with angle 45°, namely, $\theta_{45\text{-base}}$, r_{45}, and $M_{45\text{-bot}}$, respectively [Figure 2.8(b), right], are discussed.

The seismic tension force [Figure 2.8(a)] together with $M_{45\text{-bot}}$ [Figure 2.8(b)] caused the anchor bolts to stretch [Figure 2.8(c)]. Note that the anchor bolt located outmost in the diagonal direction among the 8 bolts for each column base [Figure 2.8(c) right] shows the largest tension force due to $M_{45\text{-bot}}$, and the initial pretension strain of 0.3 times the anchor bolt yield strain is included. At the 60% Takatori motion level, those anchor bolts nearly achieved yield strain (1650μ). The anchor bolt stretch behavior was consistent with the rotation of the base plates, as illustrated by Figure 2.9(a). Because the stretching of the anchor bolt and base plate rotation of column A1 occurred in alternate half cycles with those of column B3 during the oscillatory story displacement, the axes in Figure 2.9 for column B3 are reversed to demonstrate the similarity of the stiffness changes between those columns.
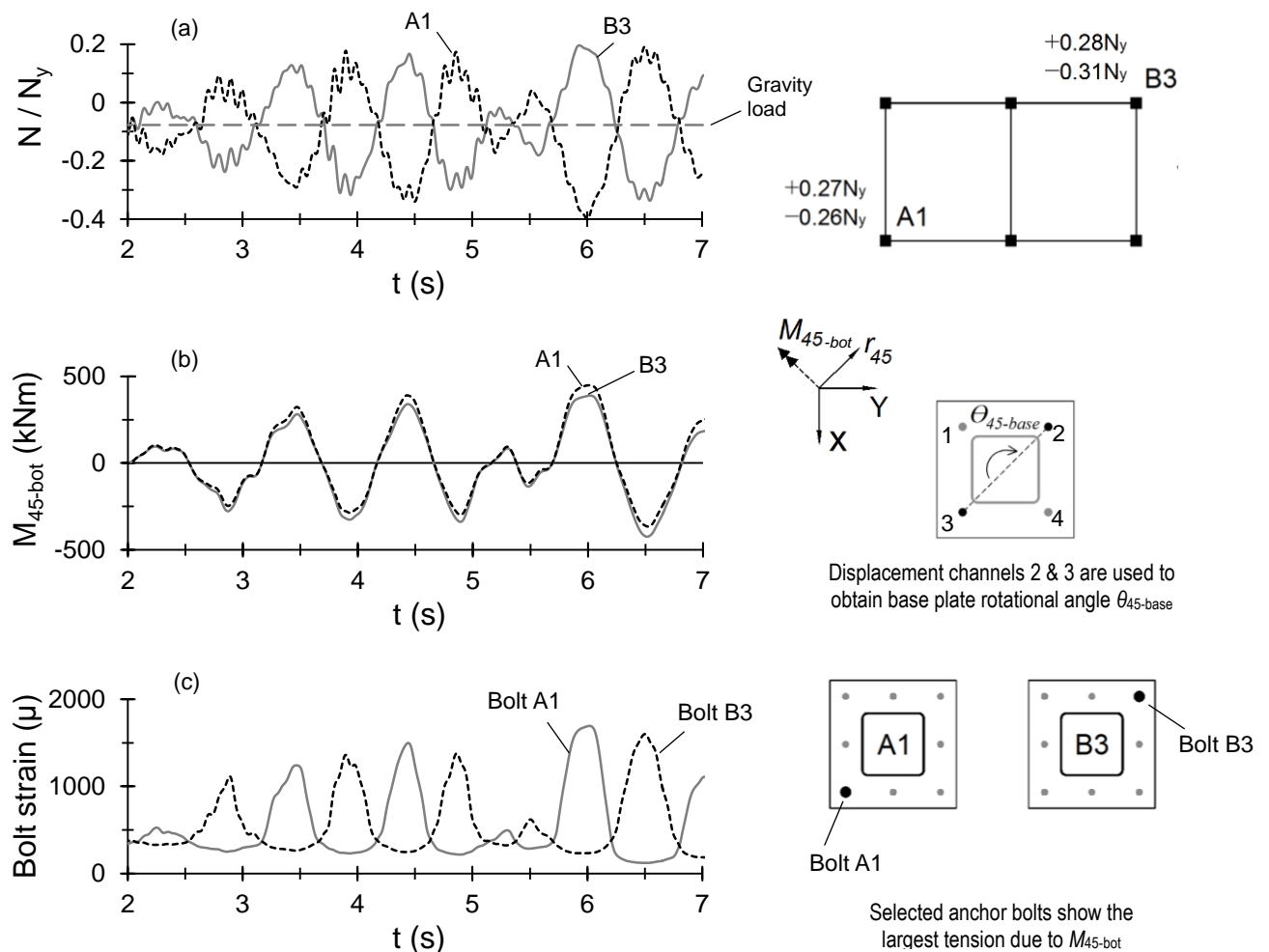
Figure 2.8 Time histories of (a) column axial forces, (b) column bottom moments, and (c) anchor bolt strains (60% Takatori level).
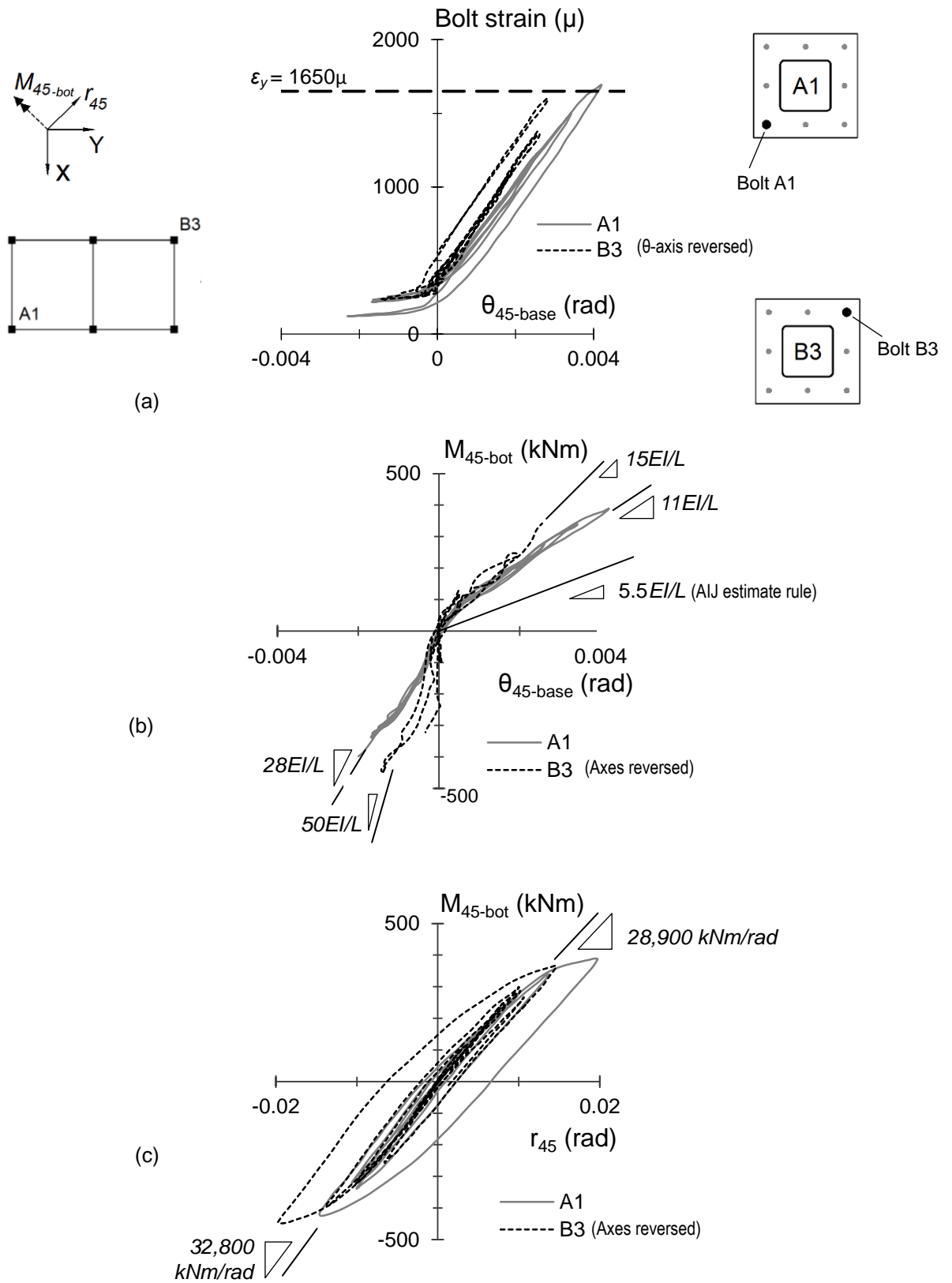
Figure 2.9 Hysteretic relation: (a) anchor bolt strain vs. base plate rotational angle, (b) column bottom moment vs. base plate rotational angle, (c) column bottom moment vs. first-story drift ratio (60% Takatori level).

Consequently, softening of the column base connections due to tension uplift can be recognized via the hysteretic relation between $M_{45\text{-bot}}$ and $\theta_{45\text{-base}}$ as well as the least-square average slope [Figure 2.9(b)]. The common rotational stiffness when the column is under compression was greater than 28 times the column flexural stiffness EI/L, where I is column moment of inertia and L is column height. This is like a rigid connection, since the stiffness greater than $10\,EI/L$ is usually considered rigid for the member connection. In response to tension load causing base uplift, the secondary rotational stiffness of column bases A1 and B3 was reduced to approximately $11\,EI/L$ and $15\,EI/L$, respectively, but they could be still considered rigid as noted above. It is also larger than $5.5\,EI/L$, estimated according to the specification by the Architectural Institute of Japan [29], where less stiff concrete foundation is accounted for instead of the steel one used for the building specimen. The secondary stiffness shown in the hysteretic curve was stable, meaning that the column base was softened but did not yield.

Column base softening also caused a slight change in the elastic stiffness in the hysteretic relation between $M_{45\text{-bot}}$ and r_{45}, for example, on the positive side (28,900 kNm/rad) compared to the negative side (32,800 kNm/rad) in the case of column A1 [Figure 2.9(c)]. Both the panel zone and column bottom end yielded, but during unloading, they began to exhibit elastic behavior. Thus, the difference in stiffness should have been caused by column base softening. Both columns showed very similar behavior but in alternate half cycles. As a result, $M_{45\text{-bot}}$ of column A1 became smaller than that of column B3 on the positive side and vice versa [Figure 2.8(b)].

In summary, softening of the bolted column base due to column uplift slightly effected the column bottom moment. However, although the base connection softened, the behaviors of the anchor bolt strains and base plate rotations were almost elastic in response to 60% Takatori motion level. The hysteretic behavior at the column bottoms was therefore mainly due to yielding of the column section.

2.4 Direction and magnitude of first-story drift displacement

If the structure is perfectly elastic, its magnitude of response should be proportional to the scale of input motion. Therefore, the experimental responses at 20% Takatori level is utilized as a common base for comparison, and the responses at the other higher Takatori levels are scaled down to that base. Figure 2.10 shows the first-story drift, u_X and u_Y, normalized to those measured at 20% Takatori motion level; they are scaled down α times, where α = 1, 1/2, 1/3, and 1/5 for 20, 40, 60, and 100% Takatori motion levels, respectively. The displacement histories for the levels of 20, 40, and 60% were similar, thus indicating a quasi-linear-elastic behavior; however, from 4.5 sec, the history for the 60% Takatori level became different, with a longer vibration period due to yielding and consequent softening of the first story. For the 100% Takatori motion level, the response was markedly different leading up to collapse, indicating a softening of the structure caused by only a few large displacement excursions.
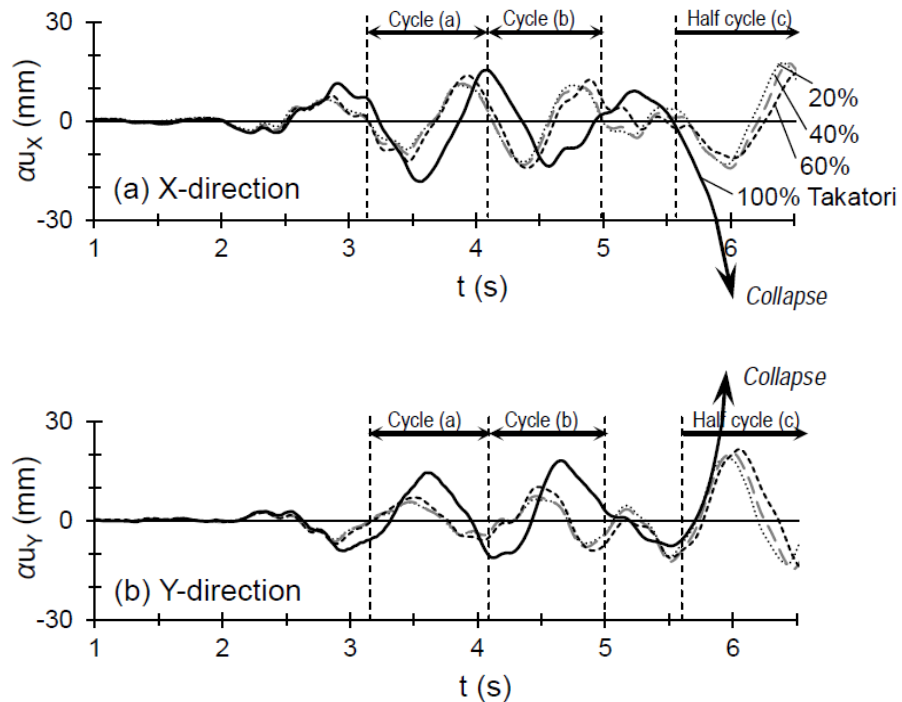
Figure 2.10 Normalized first-story drift time histories (scale factor α = 1, 1/2, 1/3 and 1/5 for 20%, 40%, 60% and 100% Takatori levels, respectively) and definitions of cycles (a), (b) and (c).
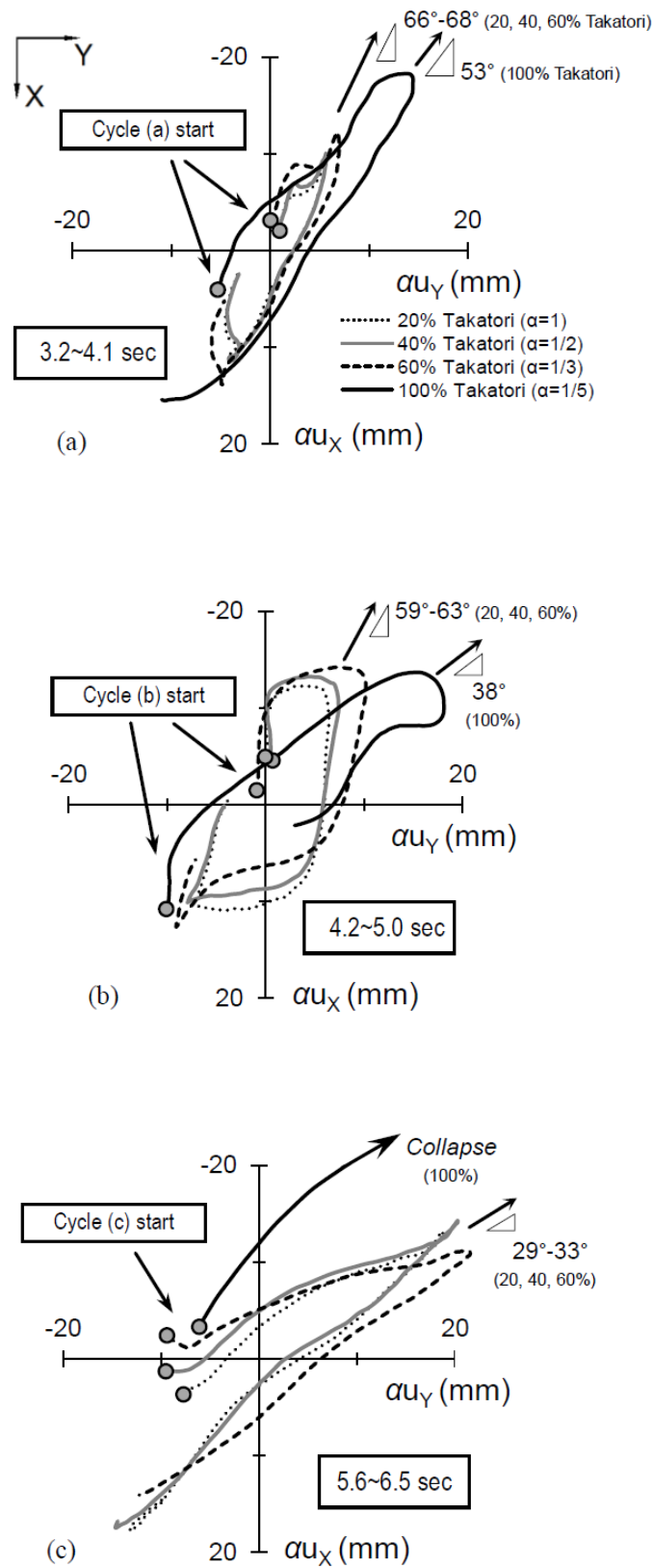
Figure 2.11 Segments of normalized first-story displacement orbit for three main cycles: (a) 3.2~4.1 sec, (b) 4.2~5.0 sec, and (c) 5.6~6.5 sec; scale factor α = 1, 1/2, 1/3 and 1/5 for 20, 40, 60 and 100% Takatori levels, respectively.

Based on Figure 2.10, three main cycles are now defined with durations of (a) 3.2~4.1 sec, (b) 4.2~5.0 sec, and (c) 5.6~6.5 sec, respectively. Each cycle is defined as the period whereby u_X makes a full loop from zero to zero. Figure 2.11 shows the breakdown segments of the normalized first-story drift orbit as three main cycles (a), (b), and (c), respectively.

The arrow in the figure indicates the main orientation of each cycle defined here as the coordinate consisting of the maximum values of both u_X and u_Y. In each cycle, the arrow remained quite similar for Takatori motion levels up to 60%. Especially, the 20 and 40% Takatori orbits were almost identical, thereby suggesting an almost linear behavior at the 40% Takatori level.

On the other hand, for the 60% Takatori level in the two cycles (a) and (b) [Figures 2.11(a)–(b), respectively], the inelasticity was apparently displayed where the peak $+au_Y$ became considerably larger. This indicates a non-proportional increase of the drift with respect to the Takatori motion level, and softening of the story due to yielding in the cycle (b) at 60% Takatori level. In the cycle (c) at the same Takatori level, its peak actual story drift ratio reached 0.02 rad, which must have caused damage in the Y direction.

This also must have reduced the stiffness of the structure, since during the cycles (a) and (b) at the 100% Takatori level, the story drift did not follow the arrow of the previous scaled motions with the orientation angles of approximately 66-68° [Figure 2.11(a)] and 59-63° [Figure 2.11(b)] with respect to the $+u_Y$ axis, respectively, but tended to yield toward the Y direction with the smaller orientation angles of nearly 53° [Figure 2.11(a)] and 38° [Figure 2.11(b)], respectively. The Y direction was also the eventual collapse direction of the building in the cycle (c) [Figure 2.11(c)].

2.5 Two-directional soft-story behavior

The previous section discussed the first-story drift displacement. This section presents the motion trajectories of the entire system, including shake table and all stories (Figure 2.12). As presented earlier, the first-story drift orbit in the case of 100% Takatori motion level did not perform a full loop during the half cycle (c) 5.6~6.5 sec [Figure 2.11(c)] but expand unboundedly in the +Y direction until the building completely settled on the supporting table and collided against the surrounding fence at 6.57 sec. Therefore, the time duration of the third cycle toward collapse is selected as an example in Figure 2.12. The story-drift velocity can be estimated based on the 0.1-sec increments marked by circles on the displacement orbit.

The axes of the 20% Takatori level graph [Figure 2.12(a)] are scaled up five times to match those of the 100% Takatori level graph [Figure 2.12(b)]. The broken line stands for the shake table motion. From inside to outside, the solid lines indicate absolute displacements of the first-, second-, third-story and roof levels. The broken lines are similar in two graphs, thus showing that the magnitude of the input ground displacement and velocity histories produced by the shake table were consistently proportional at two motion levels. The difference is found only in terms of superstructure displacement, characterizing the nonlinear collapse response of the building.

When subjected to the 20% Takatori level, the superstructure absolute displacement almost followed the shake table motion. Between 5.9 and 6.5 sec, the superstructure completed a half cycle of displacement in the same manner as the shake table input motion. At 5.9 sec, the building had translated to the farthest distance, reversed and progressively sped up until 6.2 sec, and finally slowed down until 6.5 sec.
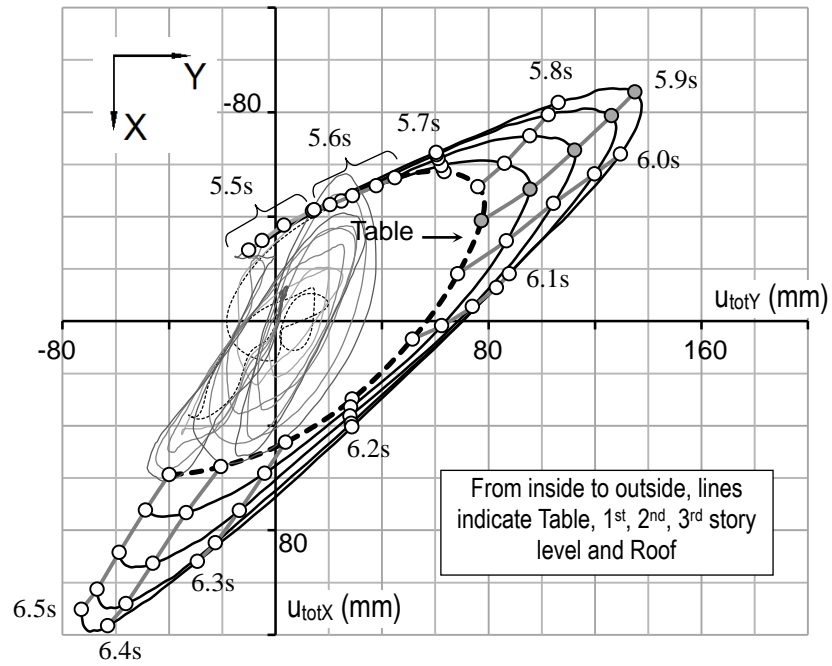
(a) 20% Takatori level
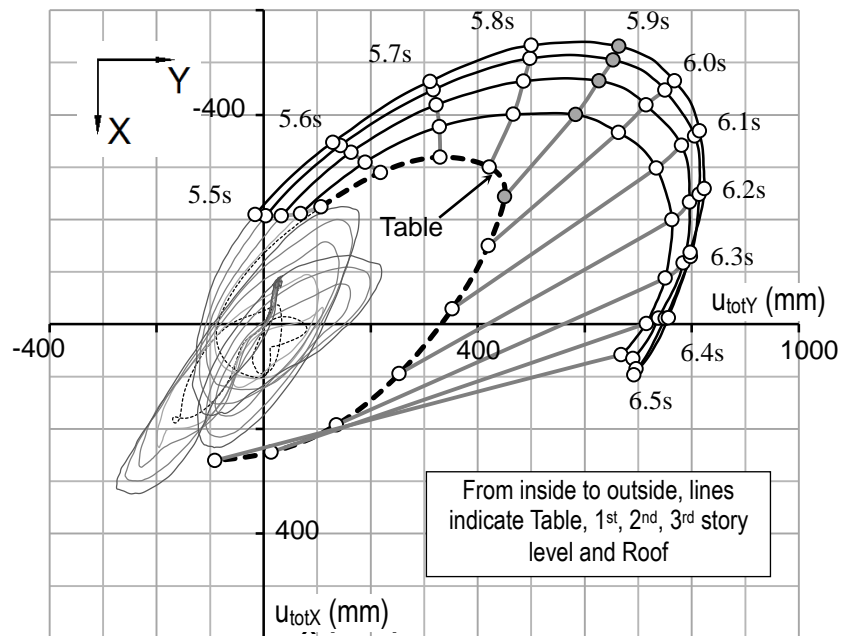
(b) 100% Takatori level

Figure 2.12 Plan view of the absolute displacement of the building and shake table at 0.1-sec increments (5.5~6.5 sec).
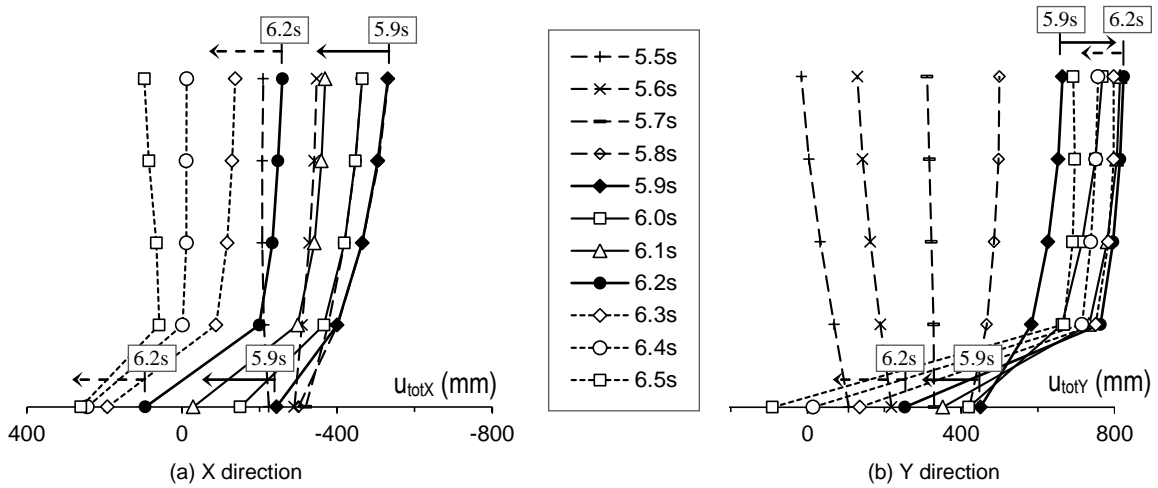
Figure 2.13 Elevation view of the absolute displacement of the building and shake table at 0.1-sec increments (100% Takatori level, 5.5~6.5 sec).

However, within the same duration for the 100% Takatori motion level, the building behaved in a completely different way due to the sudden increase in deformation at the first story. Along the X direction [Figure 2.13(a)], the deformation magnitude appeared to increase nonlinearly at the first story from 5.9 sec. The response velocity of the first story was smaller than the input ground velocity, and the structure was likely shaken suddenly. Shaking action is more apparent in the Y direction [Figure 2.12(b)] from 5.9 to 6.2 sec, where the shake table already had reversed motion but the first story had kept moving forward, as indicated by the opposite arrows in the figure. The soft-story collapse mechanism induced by column deterioration was formally initiated at approximately 5.9 sec in the Y direction. Deformations then progressively concentrated in the first story because it experienced softening. Story-drift deformation increased unbounded in the first story but decreased in the other upper stories until the entire structure settled on the supporting table and collided with the surrounding fence.

2.6 Summary

This chapter described the building specimen design and input ground motions, and also summarized the building responses during the test. The study identified the plastification progress occurring in the frame at different shaking levels, and subsequently recognized the weakened elements and damaging side of the building in accordance with the cyclic change of story drift displacement.

- The 100% Takatori motion level applied to the present specimen was predicted to be substantially more damaging in the Y direction than in the X direction based on the inelastic response spectra. This was consistent with the building response observed in the test. In contrast, peak responses of equal magnitude were predicted using elastic response spectra as well as total energy spectra [8] obtained based on the elastic assumption. Both spectra with the elastic assumption are often used to interpret inelastic responses, found to be questionable here.

- In response to the 60% Takatori motion level, the column bending moment together with the tension load due to overturning moment effect caused base plate uplift, thereby reducing the rotational stiffness of the column base connection. However, this was not sufficient to cause either semi-rigid rotational behavior of the base or tension fracture of the anchor bolt. The design of the column base connection for the present building specimen did not explicitly guarantee such behavior because it did not consider the effects of tension load. Due to a lack of clear design method that could consider complex effects of anchor bolt fracture and end plate deformation under tension or shear load, as well as local buckling at a column section subject to compression load, further study is needed in this area.

- Along with the increase in the scaled Takatori motions, the natural period also increased due to the plastification of frame components.

Concentration of the drift in the first story occurred at the 60% Takatori level and involved significant inelastic deformation of the panel zones and columns. In contrast, the beams remained nearly elastic throughout the tests because their overstrength due to the composite action of the concrete slab is approximately 1.5 times the bare beam strength.

- The cycle-by-cycle shifting of displacement direction was clarified in this chapter and will be utilized for further discussion on both global and local responses of the building specimen during collapse excitation level presented hereafter in the following chapter.

CHAPTER 3

BUILDING COLLAPSE CAUSED BY COLUMN
DETERIORATIONS

Chapter 3

BUILDING COLLAPSE CAUSED BY COLUMN DETERIORATIONS

3.1 Local buckling and deterioration of first-story columns

The strength loss of columns is not only due to axial compression increase but also caused by local buckling effect. In the previous experimental reports [6–8], the interaction of M_Y and M_X was discussed, but the simultaneous effect of axial force and local buckling on column moment was not efficiently represented. Therefore, in order to clarify the strength loss due to local buckling, this study utilizes factor R proposed by Inoue [44] for square tube columns, counting for the simultaneous interaction of axial force and biaxial moments (as shown in Equation 1, where N_y is yield axial strength, and M_p is plastic moment in case of zero axial force) in relation with story drift ratio r (Equation 2) characterizing the magnitude of column deformation. According to Inoue [44], $R = 1$ shows the interaction of N, M_Y, and M_X at the yield surface in the case of $N/N_y \leq 0.5$, consistent with the experimental case being evaluated. If the column is stable, its magnitude of factor R should increase in accordance with the increase of story drift r.

$$R = \frac{4}{3}\left(\frac{N}{N_y}\right)^2 + \frac{M_Y}{M_p} + \frac{3}{4}\left(\frac{M_X}{M_p}\right)^2 \quad \text{if } M_Y/M_X \geq 1 \qquad \text{(1-a)}$$

$$\text{or} \quad R = \frac{4}{3}\left(\frac{N}{N_y}\right)^2 + \frac{M_X}{M_p} + \frac{3}{4}\left(\frac{M_Y}{M_p}\right)^2 \quad \text{if } M_Y/M_X < 1 \qquad \text{(1-b)}$$

$$r = \sqrt{r_X^2 + r_Y^2} \qquad\qquad\qquad (2)$$

Figure 3.1 shows the (a) 1st-story drift ratio orbit, and time histories of (b) axial force, (c) bottom moment, (d) combined strength factor R of all six columns, and (e) 1st-story drift ratio r at 100% Takatori level. Because the building eventually collapsed toward the $+r_Y$ direction, the study selects to investigate the development of R during the segment showing r_Y increase at each cycle, thereby the deterioration can be detected whenever the reduction of R occurs. Three segments denoted by ①, ② and ③ [Figure 3.1(a)] are highlighted, and the other timing regions are shaded.

In the segment ① of cycle (a), reductions of factor R occurred early to columns B2 and B3 at 3.33 sec and 3.37 sec, respectively [Figure 3.1(d)], and later to columns A2, A3, B1 when r exceeded 0.02 rad. Displacement loading was still in progress [Figure 3.1(e)], but moments of those columns decreased [Figure 3.1(c)] except column A1. In the subsequent segments ② and ③ of cycles (b) and (c), although the magnitude of r remained similar, the peak values of factor R gradually declined, indicating the cumulative deterioration caused by local buckling.

As shown in Table 3.1, at the time of peak building overturning moment, the factors R of all six columns at 100% Takatori level were smaller than those at 60% Takatori level although the axial force did not differ considerably between two levels. The severity of deterioration is easily recognized in the reducing sequence from columns B3, B2,… to A1. They are closely related to their axial compressive magnitudes [Figure 3.1(b)].
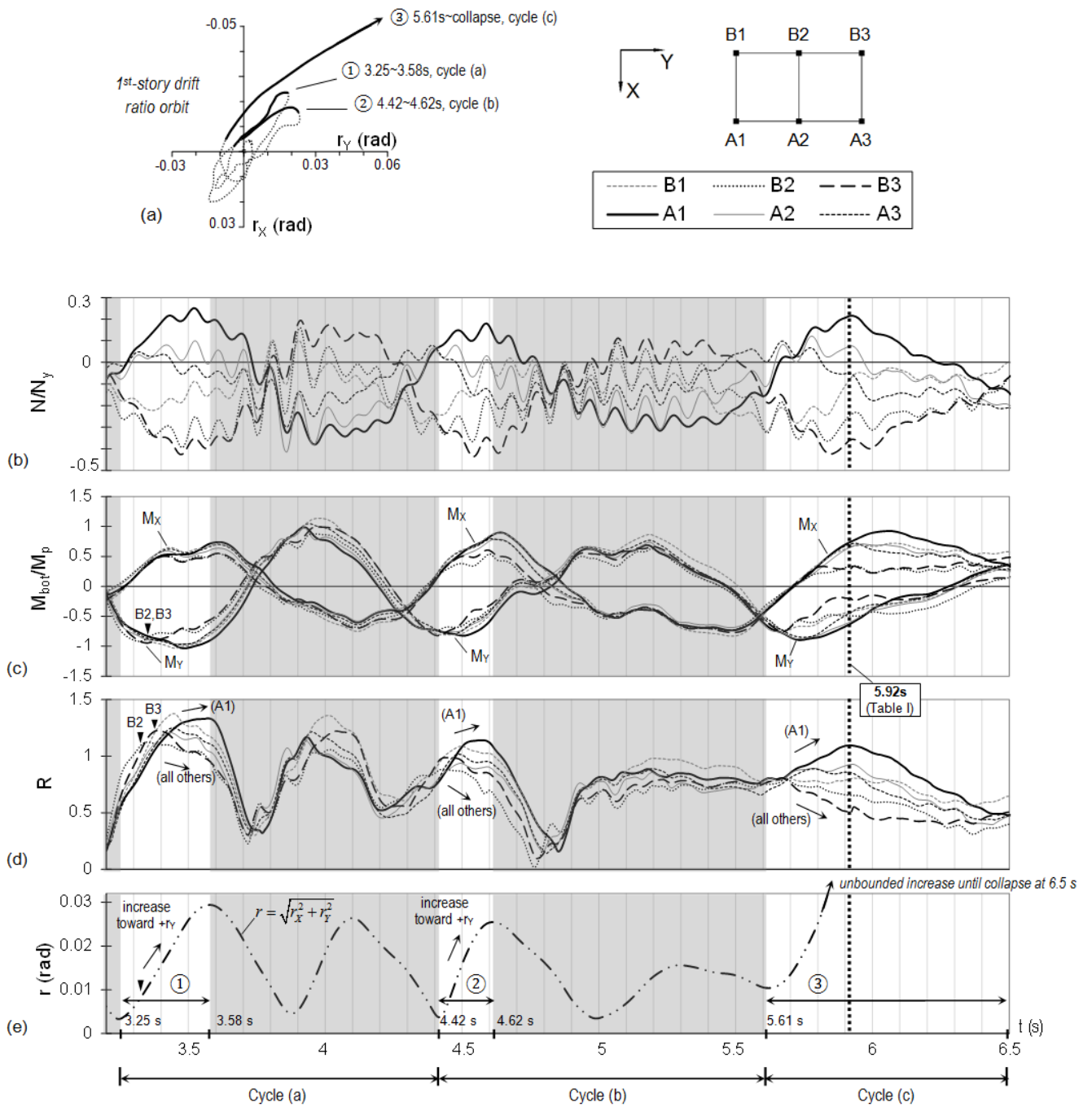
Figure 3.1 (a) 1st-story drift ratio orbit, and time histories of (b) axial forces, (c) bottom moments, (d) combined strength factor R of 1st-story columns, and (e) 1st-story drift ratio $r = \sqrt{r_X^2 + r_Y^2}$ (100% Takatori level)

Table 3.1 Axial force N/Ny and combined strength factor R of all six columns at the time of peak overturning moment (60 and 100% Takatori levels) [N_y = 3366 kN]

	60% Takatori (6.01s)		100% Takatori (5.92s)	
	N/N_y	R	N/N_y	R
A1	+0.18	1.25	+0.22	1.10
A2	−0.06	1.18	+0.08	0.93
A3	−0.16	1.22	−0.05	0.86
B1	+0.00	1.34	−0.07	0.80
B2	−0.26	1.22	−0.24	0.65
B3	−0.40	1.16	−0.36	0.54
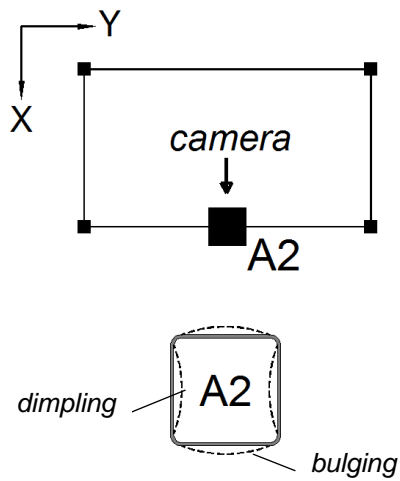
3.6 sec (cycle a)

4.7 sec (cycle b)

5.7 sec (cycle c)

6.3 sec (before collapse)

Figure 3.2 Video snapshots at the base showing buckling modes of column A2 (100% Takatori).
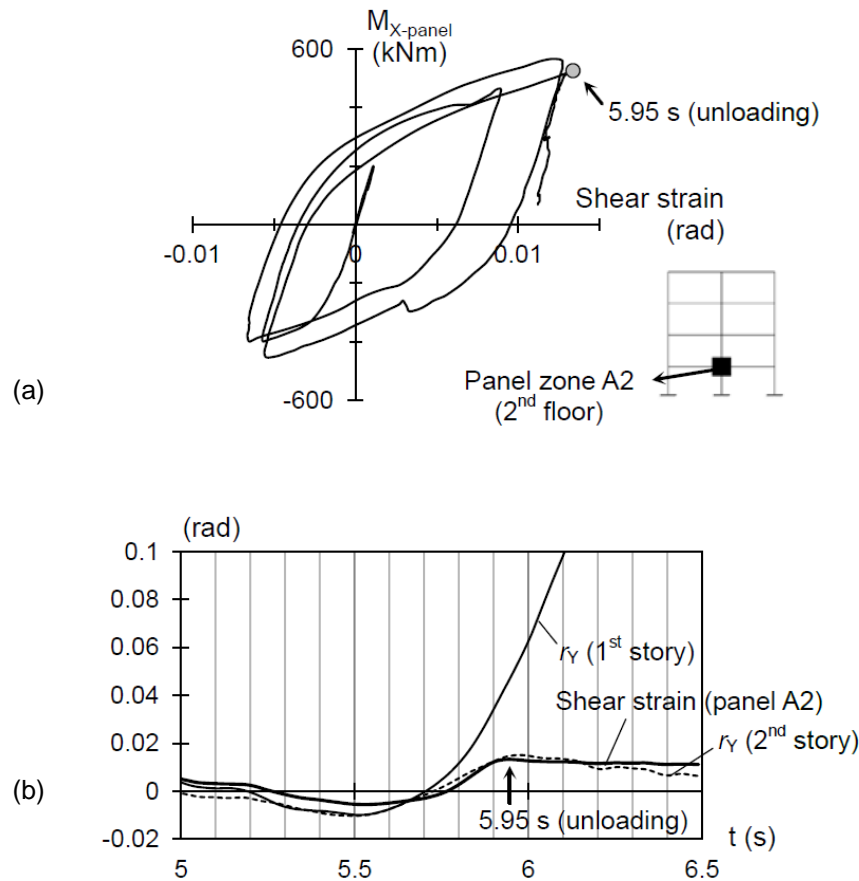
Figure 3.3 (a) Hysteretic behavior, and (b) deformation history of 2nd-floor panel zone A2 (100% Takatori level).

Local buckling due to the combined axial force and moment was one cause of column deterioration. To illustrate the local buckling behavior during the 100% Takatori excitation, Figure 3.2 shows video snapshots of the base of column A2, which provided the best image quality. Note that the column surface shown in the photos is from the viewpoint of the camera, as indicated in Figure 3.2-top. Local buckling could be easily recognized at the column surface which bulged out significantly from the first cycle and then further developed in subsequent cycles, confirming the deterioration at the very early time of excitation.

The deteriorated moment capacity of the first-story column due to local buckling became incapable of resisting the moment transferred from the panel

zone, which was located above and significantly yielded but exhibited a large increase in resistance due to strain hardening [Figure 3.3(a)]. Figure 3.3(b) shows the time histories of the panel zone shear strain and drift ratios of the first and second stories. As the story drifts continued increasing from 5.71 sec, the panel zone experienced strain hardening, and its capacity exceeded the buckling capacity of the columns. Then, local buckling occurred at the column ends. The panel zone and the second story were unloaded at 5.95 sec [Figure 3.3(b)] and returned to being elastic [Figure 3.3(a)], causing substantially more drift demand to the first-story column until collapse.

Figure 3.4 shows the hysteretic curves of the column B3's bottom moments $M_{Y\text{-bot}}$ and $M_{X\text{-bot}}$ at 100% Takatori motion level. The low-pass filtered version of column axial force (*dotted line*, in respect to secondary vertical axis) is also displayed in the figure, thereby showing the deterioration of $M_{Y\text{-bot}}$ mainly occurring under compressive load condition when the building deformed in the negative r_X direction. Note that the axial force is low-pass filtered to eliminate the high-frequency fluctuation due to vertical acceleration, in order to provide an easily identified hysteretic curve in Figure 3.4. Three points of timing when $M_{Y\text{-bot}}$ started decreasing due to local buckling: 3.35 sec (marked by △), 4.40 sec (□) and 5.68 sec (○) at three main cycles (a), (b) and (c), respectively, are therefore selected to show; and both moments and axial forces at those instants are also indicated in Figure 3.4. Because the principal direction of biaxial bending moment in cycle (a) was close to the X direction, $M_{Y\text{-bot}}$ early reached to peak capacity and then deteriorated due to local buckling. $M_{X\text{-bot}}$ developed later but could not achieve high capacity as well as linear relation with the increasing story drift r_Y because of the change in column cross section due to damage by local buckling. A similar situation repeated in the subsequent cycles (b) and (c). The column was subjected to quite large compressive force of approximately $-0.25 N_y$ when the local buckling and deterioration of $M_{Y\text{-bot}}$ started occurring.
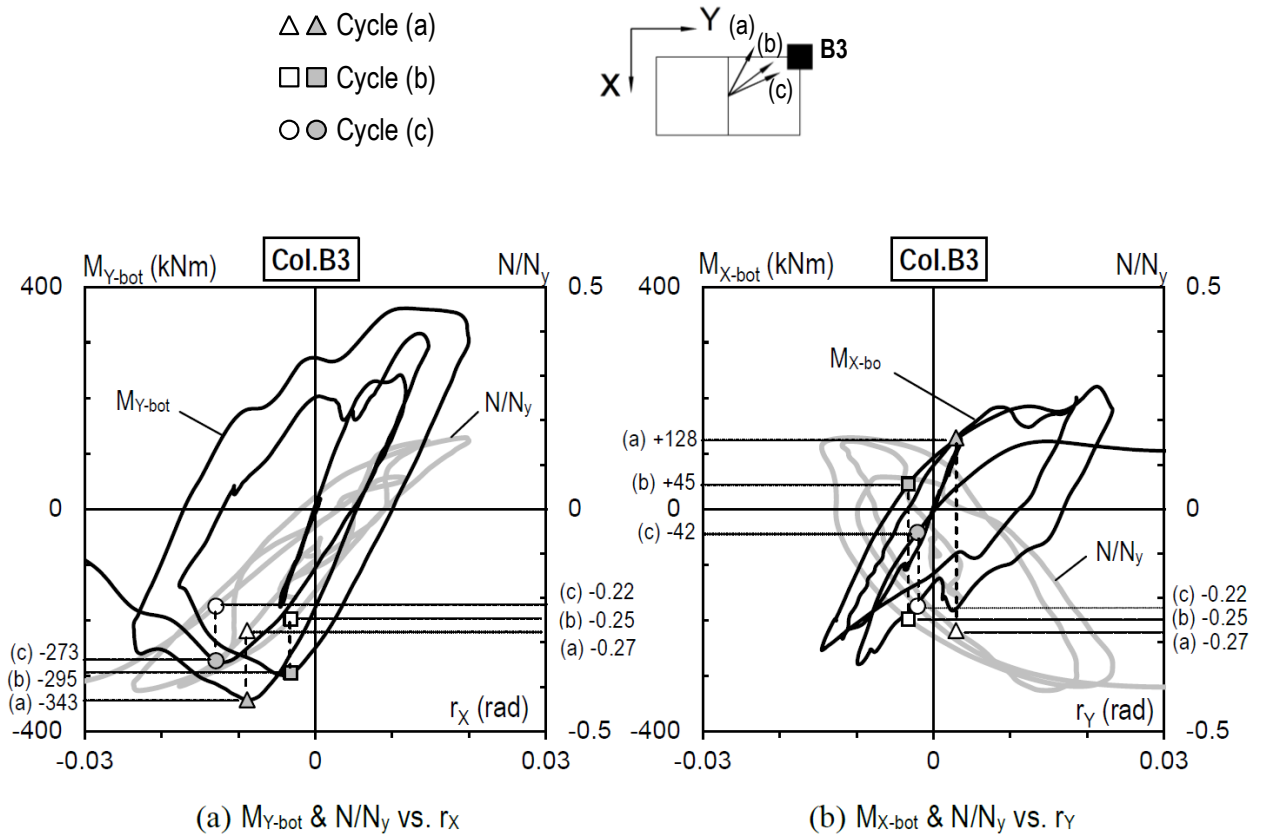
Figure 3.4 Column B3's bottom moment (*solid line*, primary axis) and low-pass filtered axial force (*dotted line*, secondary axis) vs. first-story drift ratio at 100% Takatori level, and moment and axial force magnitudes at three peaks of bottom moment ($M_{Y\text{-bot}}$) with compressive axial force condition.
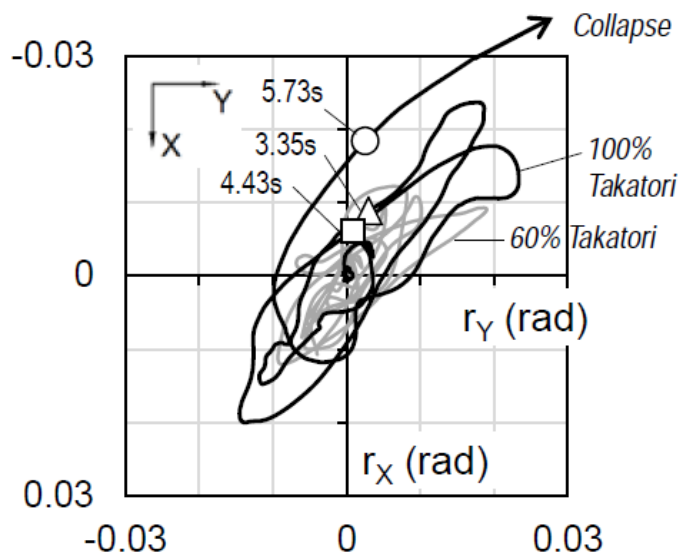
Figure 3.5 First-story drift ratio orbit at 60% (*gray*) and 100% (*black*) Takatori levels.
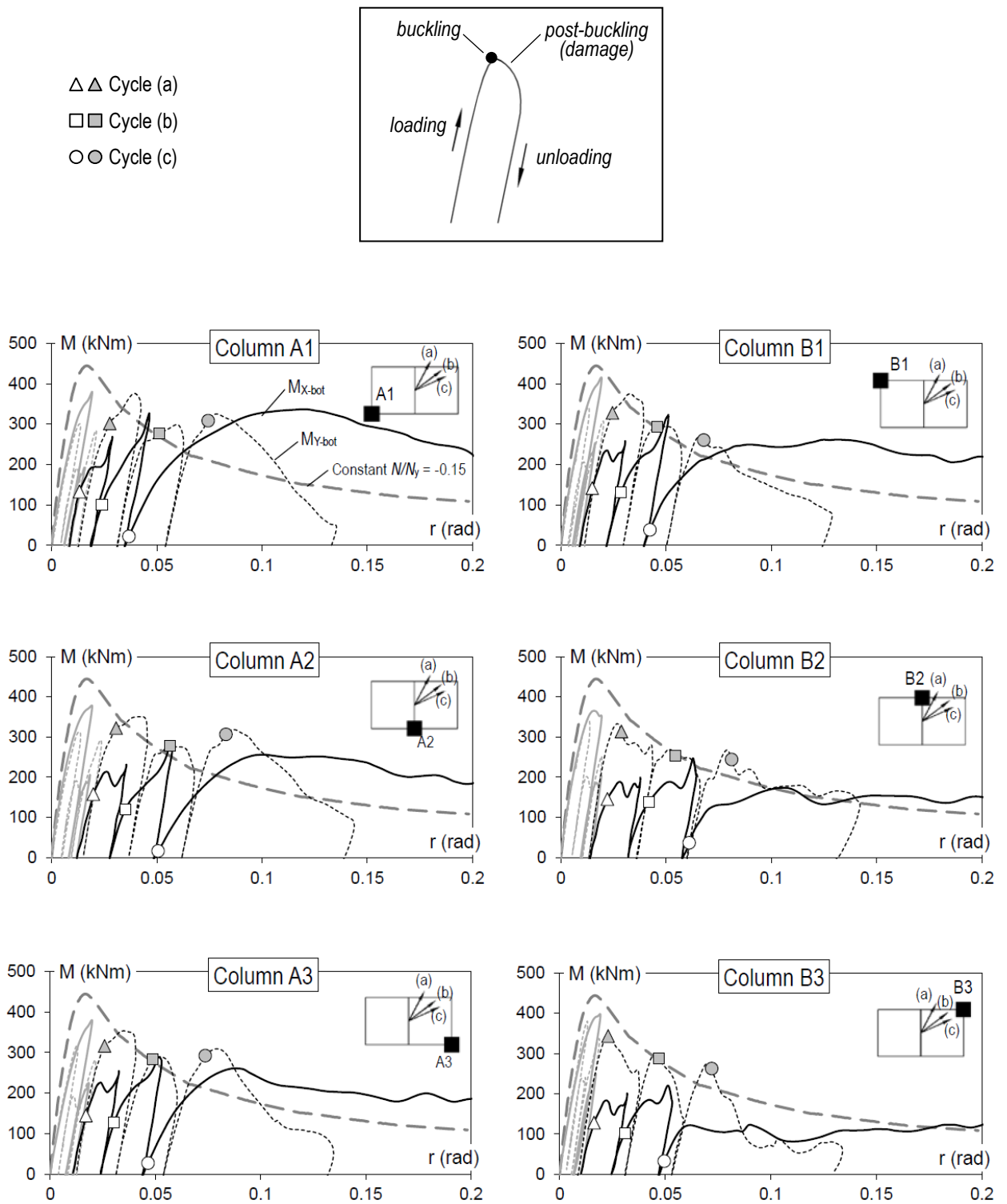
Figure 3.6 Accumulated deteriorations of first-story column bottom moments characterized by skeleton curves for the negative $M_{Y\text{-bot}}$ and positive $M_{X\text{-bot}}$, with symbols commonly showing both values at the times of 3.35s, 4.43s and 5.73s of three cycles (a), (b) and (c), respectively.

A full picture of the sequence of first-story column deterioration until the collapse time is presented in the followings. Figure 3.5 shows the first-story drift orbit with symbols marking the start of the three cycles. Figure 3.6 displays the accumulated moment deterioration of all six columns presented in shape of skeleton curves.

The load-deformation skeleton curve whose plotting method is adopted from Yamada *et al.* [30] (described in Appendix A.1) can indicate the cyclic degradation of column moment due to local buckling. The symbols showing the timing points of three cycles correlating with those in Figure 3.5 are also plotted in Figure 3.6, indicating the earlier magnitude development of $M_{\text{Y-bot}}$ than $M_{\text{X-bot}}$ within each cycle and consequent deterioration of $M_{\text{X-bot}}$ due to the preceding degraded $M_{\text{Y-bot}}$.

Especially, during the last half cycle (c) prior to collapse, $M_{\text{X-bot}}$ of all six columns increased from zero, but the tangent stiffness at the early stage was only approximately 1/3 of that in previous cycles due to the change in cross section by the preceding decrease in $M_{\text{Y-bot}}$. In addition, the skeleton curve by the cyclic bending test conducted prior to the collapse experiment (using the same column type, under constant compression load of $-0.15N_{y}$) is included in Figure 3.6. Based on that, the discrepancy of moment deteriorations amongst columns is easily recognized, which is closely related to the seismic compression force that developed in the columns, as indicated earlier in Figure 3.1(a) and Table 3.1. Larger compression forces resulted in more significant column deterioration.

In general, the column deterioration during the early cycles of the excursion at 100% Takatori motion level was caused by not only large compression forces but also local buckling effects. Column deterioration in the r_{Y} direction preceded by deterioration in the r_{X} direction progressively became more significant as the story drift increased toward collapse.

## 3.2 Influence of column deterioration on building collapse response

The previous section discussed the deterioration of the column moment capacity during the first two main cycles. This section emphasizes the subsequent half cycle up to collapse (5.6~6.5 sec) by referring to the deterioration of both the column moment and shear capacities, including the P-δ effect under exceedingly large story drifts.

During the last half cycle, column shear deterioration first occurred in the X direction. As the first-story drift ratio r_X continued to rapidly increase, the horizontal shear forces Q_X [Figure 3.7(a)] of the three columns B3, B2 and B1 stopped increasing and started decreasing at 5.68 sec, which was induced by moment deterioration at the bottom [Figure 3.1(b)] and top of those columns. The columns were subject to compression forces from –0.2 to –0.4N_y [Figure 3.7(a)]. For columns A3, A2 and A1, which are under zero or positive axial load, their shear forces Q_X later decreased at 5.79 sec, mainly because of the larger drift angle, in contrast to columns B1, B2 and B3, as discussed above. Due to considerable deterioration of the column shear capacity, ΣQ_X (story shear in the X direction) deteriorated remarkably after 5.8 sec [Figure 3.8(b)] and continued until unloading at the drift ratio r_X of –0.08 rad.

Subsequently, column shear deterioration occurred in the Y direction [Figure 3.7(c)]. Q_Y of column B3 deteriorated the earliest at 5.82 sec with a remaining strength of approximately 1/3 of the maximum capacity attained later by column A1. Q_Y of column B2 deteriorated simultaneously but then remained larger than that of column B3 because column B2 experienced a smaller compression force than did column B3 [Figure 3.7(a)], thereby experiencing a smaller P-δ effect. ΣQ_Y (story shear in the Y direction) started to exhibit deterioration at this time [Figure 3.8(c)] and progressively became more degraded when the deterioration of Q_Y of columns A3, A2 and B1 occurred at 5.91, 5.94 and 5.96 sec, respectively [Figure 3.7(c)]. Column A1 was the only column subjected to a large tension load of nearly +0.2N_y and could maintain its highest capacity until deterioration at 6.08 sec.
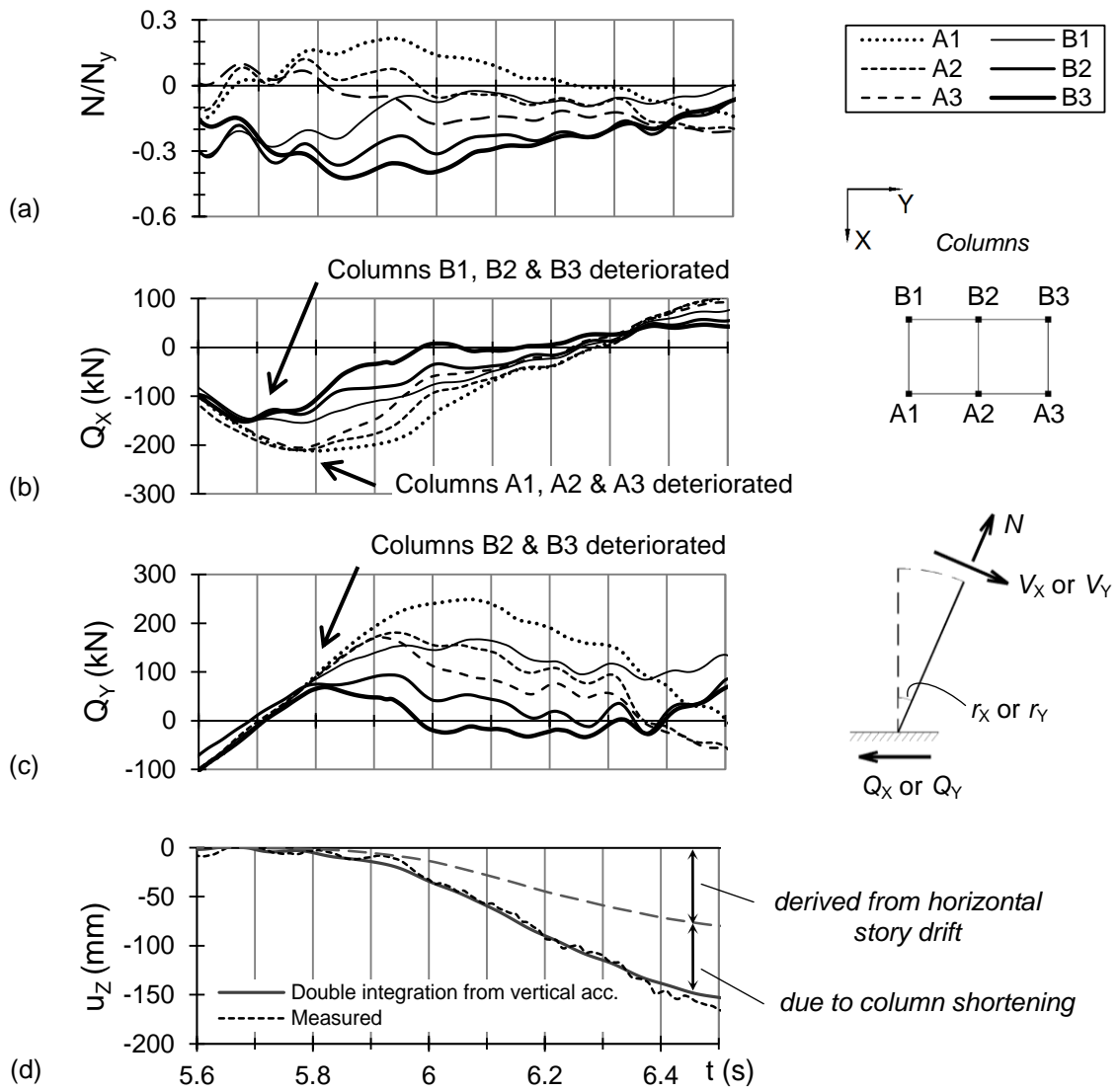
Figure 3.7 Time histories of 1st-story column (a) axial forces, (b) horizontal shear forces Q_X, (c) Q_Y, and (d) 2nd-floor downward displacement (100% Takatori level).
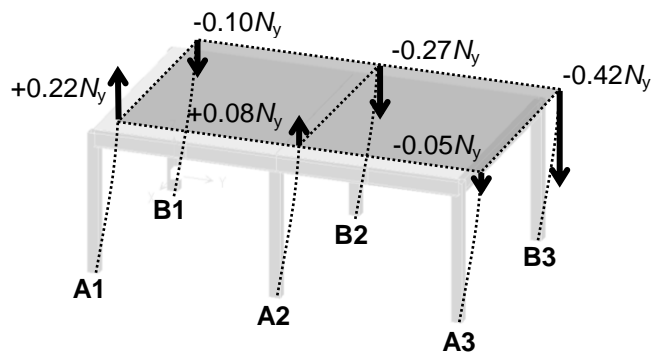
Figure 3.8 First-story column axial forces at 5.9 s, peak building overturning moment (100% Takatori level).
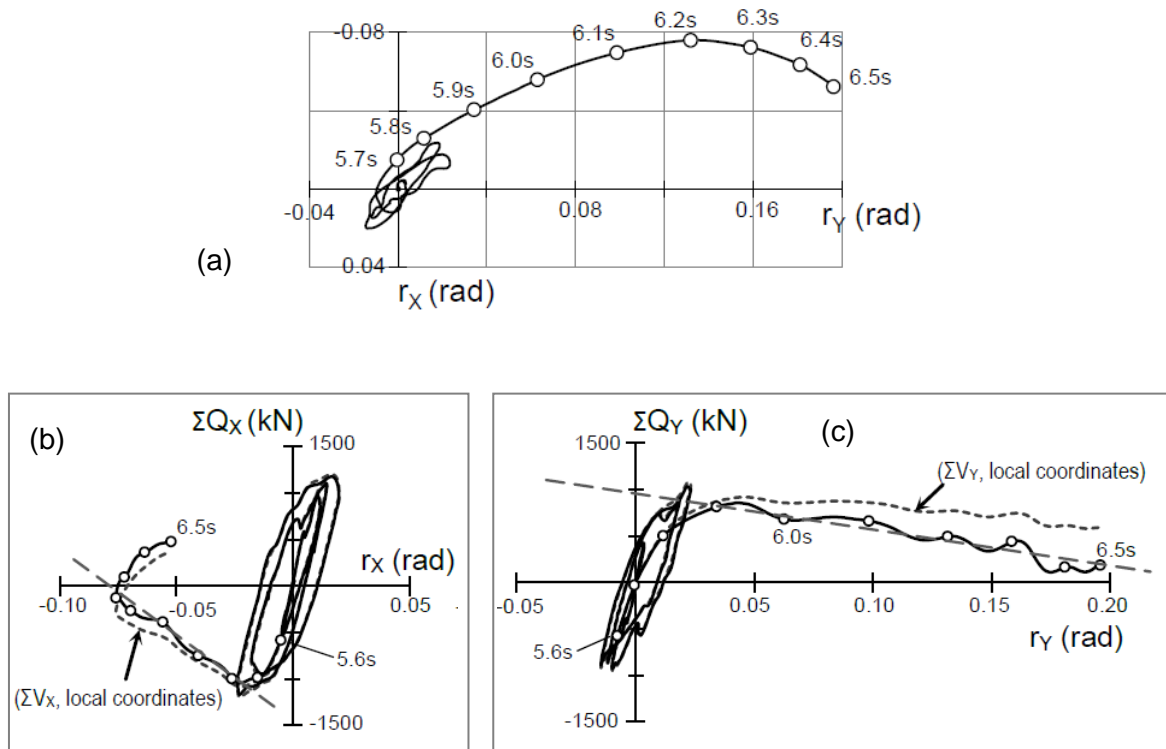
Figure 3.9 (a) 1st-story drift ratio orbit, and hysteretic curves of 1st-story shear forces (b) ΣQ_X and (c) ΣQ_Y (100% Takatori level).

As shown in Figure 3.7(d), the downward displacement of the floor center $(-u_Z)$ started increasing rapidly at 5.7 sec, which was related to the start of the above mentioned column deterioration. It was even larger than the geometric downward displacement derived from the horizontal story drift, thus confirming the phenomenon of column shortening caused by local buckling (Figure 3.2). Note that u_Z was obtained from the three-dimensional displacement measuring system and can be verified by the one obtained from double integration of the floor vertical acceleration.

The schematic description of column axial forces at 5.9 sec, the time of peak building overturning moment (Figure 3.8) illustrates the trend of different tension and compression loads developed in columns causing different states of their moment and consequent shear deteriorations as discussed above.

Deterioration and local buckling of the columns in the first story played an important role in weakening the story and determining the unbounded translational displacement [Figure 3.9(a)], lasting from 5.7 to 6.57 sec when r_Y became 0.2 rad, wherein the building collided with the surrounding fence and completely settled on the supporting table.

The P-δ effect became more significant as the story drift increased, as shown by the hysteretic relations between the story-shear force and the story-drift ratio given in Figures 3.9(b)–(c) for the X and Y directions, respectively. The broken lines in those figures represent summation of the column resisting shear forces ΣV_X (or ΣV_Y) in local coordinates regardless of the tilting effect, which were obtained directly from column strain gauges. The geometric stiffness $-W/(H-|u_Z|)$, where W is the building weight and H is the first-story height, can be clearly recognized based on the difference in slopes between the $\Sigma V_{X/Y}$ and $\Sigma Q_{X/Y}$ hysteretic branches during the large story-drift range.

To protect the shake table from damage, the experiment had to limit the collapse to a story-drift ratio r_Y of 0.2 rad. At that time, even though the P-δ effect made the base shear ΣQ_Y approach zero, the frame was still able to resist the lateral force [indicated by high ΣV_Y, Figure 3.9(c)]. If the story drift had not been limited by the safeguard system, the building might have continued translating further along the Y direction due to the P-δ effect until completely losing shear resistance. Regardless, the exceedingly large story drift r_Y and minimal base shear ΣQ_Y did indicate a collapse in the Y direction. Note that zero base shear ΣQ_X was also observed, but it occurred during unloading; therefore, it did not indicate structural collapse in the X direction.

A summary of first-story column deteriorating sequence based on column bottom moment hysteretic curves is described as follows. During the first two main cycles in 100% Takatori level, $M_{Y\text{-bot}}$ (Figure 3.10) of columns B1, B2 and B3 deteriorated whenever the building deformed toward the negative r_X-direction. In contrast, $M_{Y\text{-bot}}$ of columns A1, A2 and A3 deteriorated when the building reversed deformation toward the positive r_X-direction.
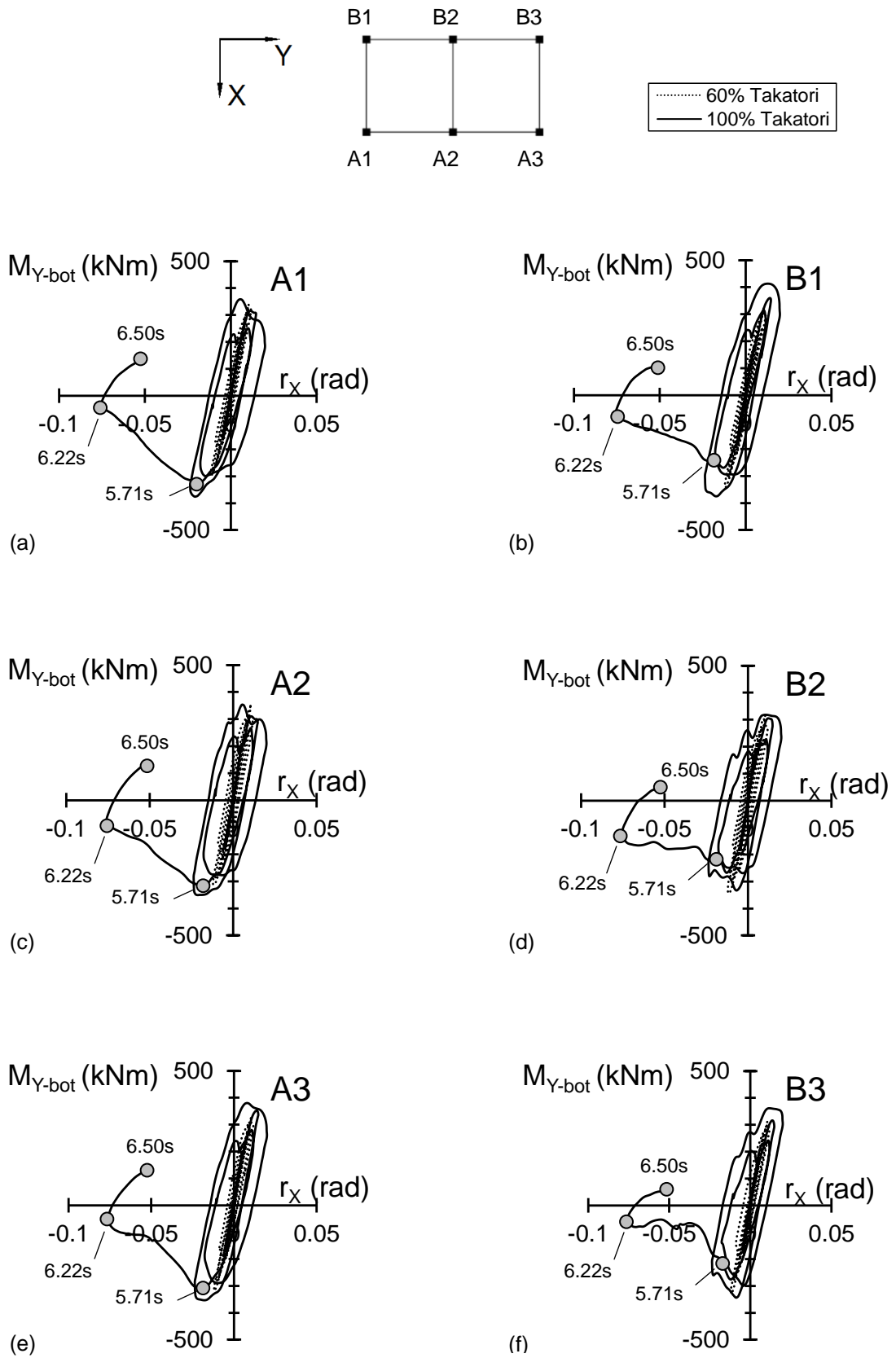
Figure 3.10 Column bottom moment vs. first-story drift ratio with respect to the X direction (dotted: 60% Takatori, solid: 100% Takatori).
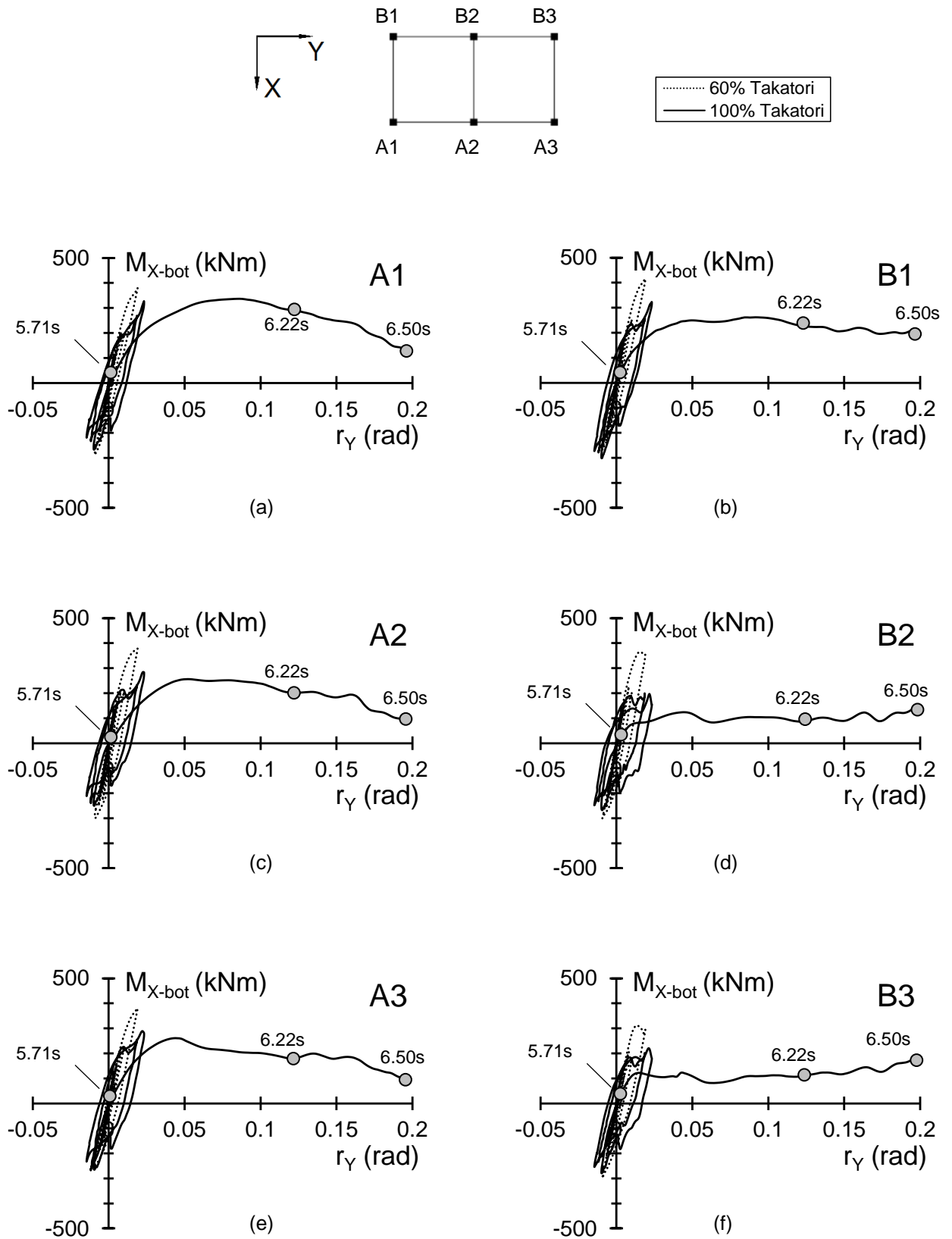
Figure 3.11 Column bottom moment vs. first-story drift ratio with respect to the Y direction (dotted: 60% Takatori, solid: 100% Takatori).

Levels of column deterioration were different from one another, closely related to the seismic compression force developed in columns, as indicated in Figure 3.1(a) and Table 3.1. The larger compression force, the more significantly those columns deteriorated. In the last half cycle prior to collapse, from 5.71 sec to 6.22 sec (r_X unloading), $M_{Y\text{-bot}}$ (Figure 3.10) deteriorated with negative slope shown clearly in the hysteretic curve, which means the columns tended to be damaged toward r_X-direction.

Levels of column deterioration depending on column compression forces are also shown apparently in $M_{X\text{-bot}}$ (Figure 3.11), especially at columns B2 and B3 where their moment capacities after deterioration were reduced to only half of those in previous cycles. From 6.22 sec, unloading occurred to r_X, but r_Y became more critical due to suddenly applied loading as well as deteriorated strength caused previously by the deformation in the X direction, resulting in the column damage and building collapse toward the Y direction.

Finally, schematic illustrations relating column axial force and moment responses with the 1st-story drift movement (Figure 3.12) are given in Figures 3.13–3.19 for columns A1, A2, A3, B1, B2, B3, and the frame, respectively, indicating values at some points of timing: 5.71s (cycle start), 5.93s (peak overturning moment), 6.22s (r_X unloading), and 6.50s (prior to collapse).
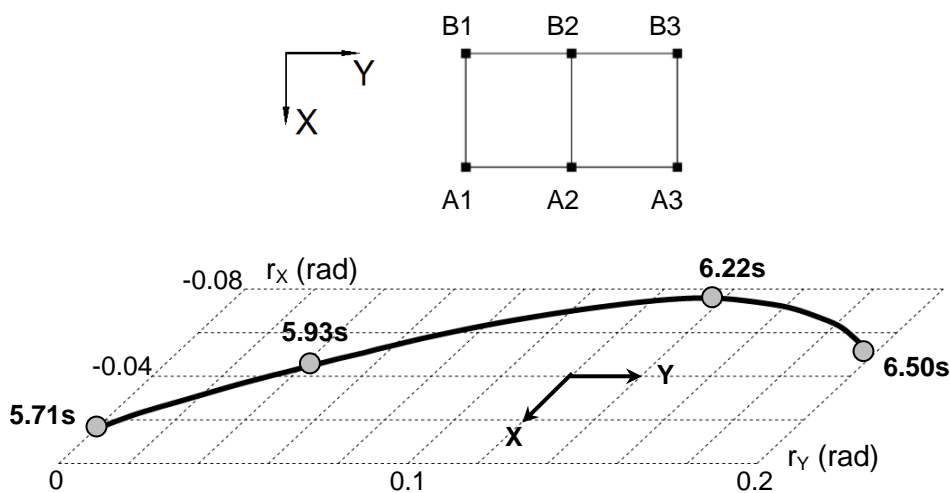
Figure 3.12 First-story drift ratio orbit (5.71-6.50s, 100% Takatori)
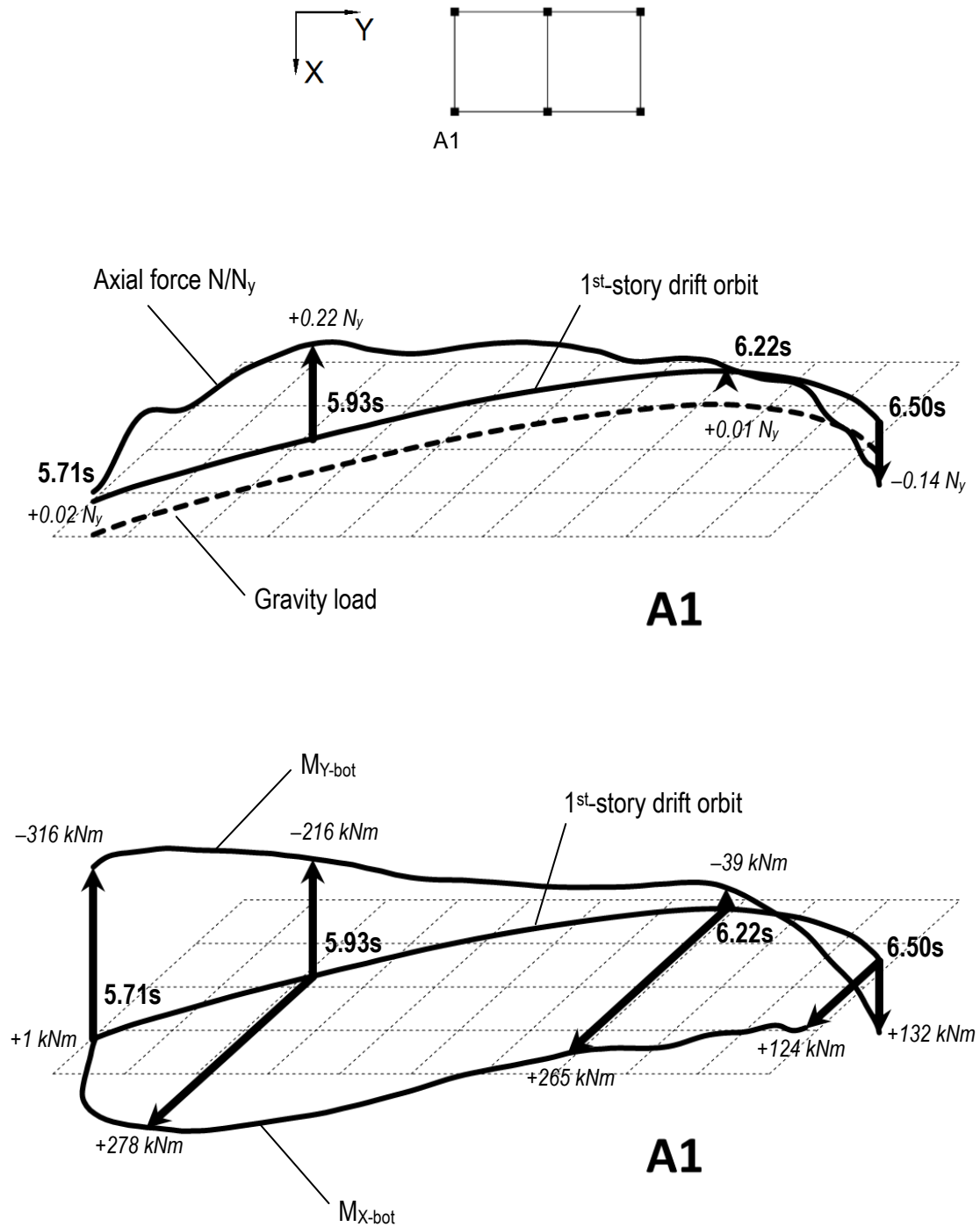
Figure 3.13 Column axial force and bottom moments tracing the 1st-story drift ratio orbit (5.71-6.50s, 100% Takatori, column A1).
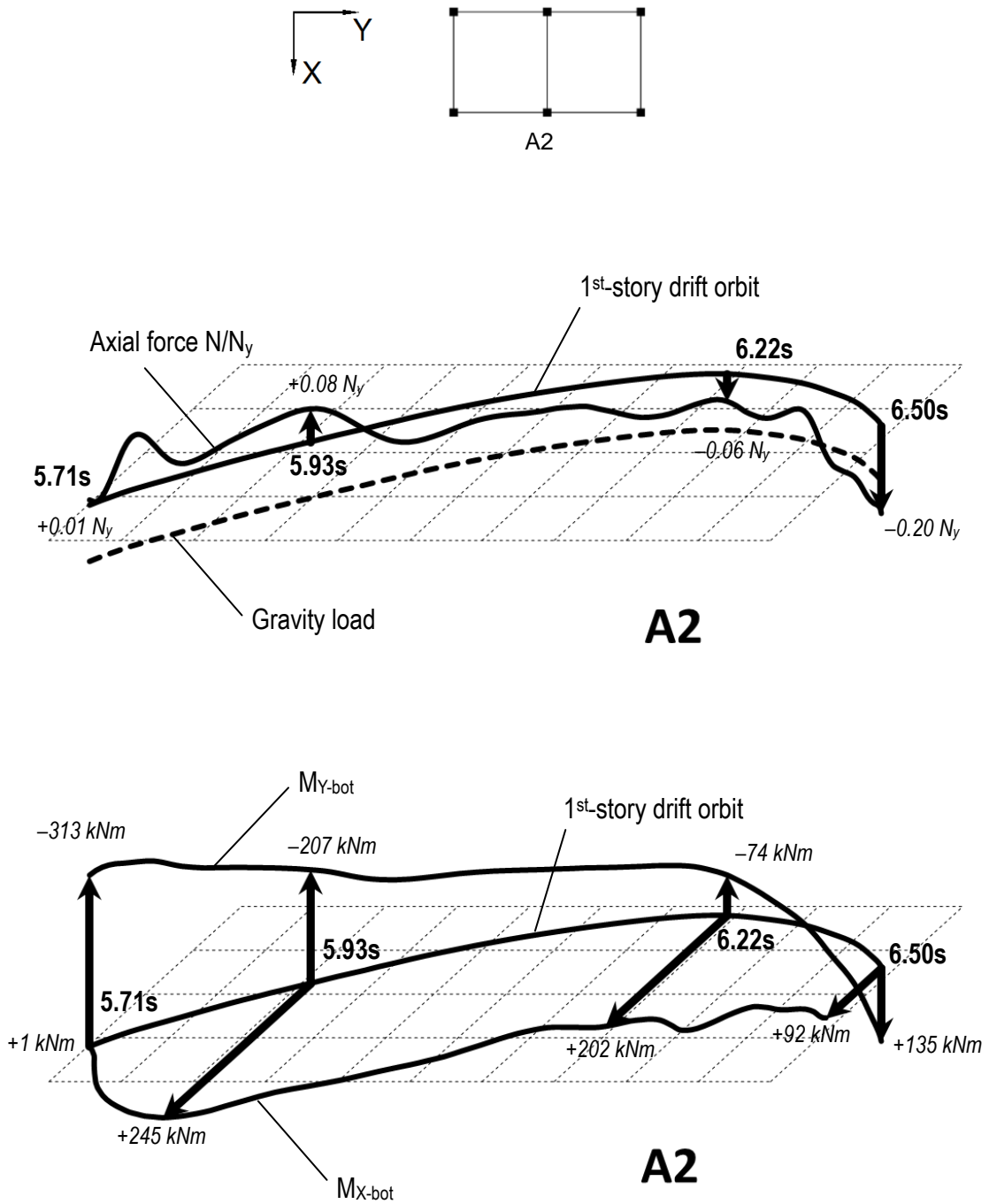
Figure 3.14 Column axial force and bottom moments tracing the 1st-story drift ratio orbit (5.71-6.50s, 100% Takatori, column A2).
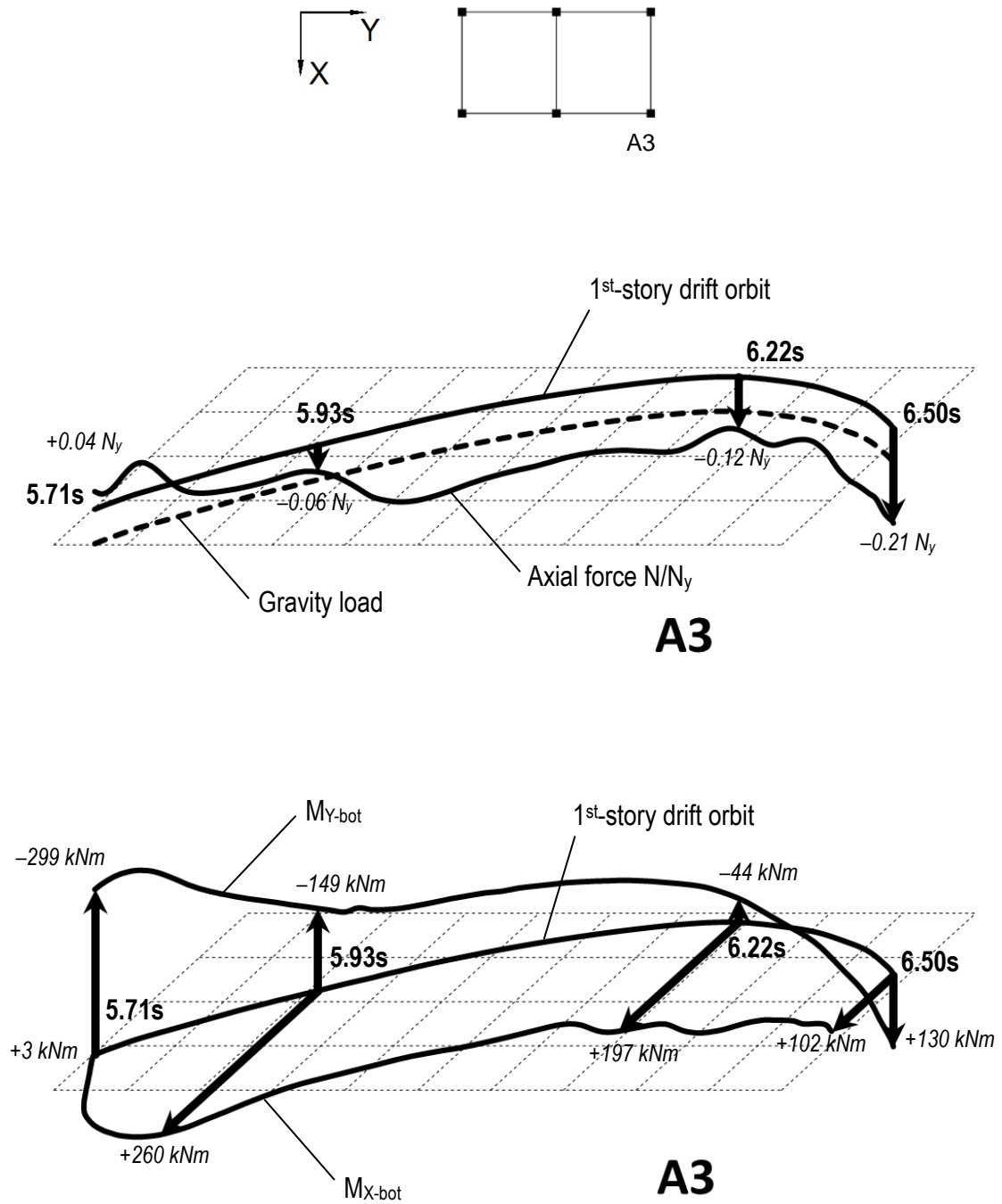
Figure 3.15 Column axial force and bottom moments tracing the 1st-story drift ratio orbit (5.71-6.50s, 100% Takatori, column A3).
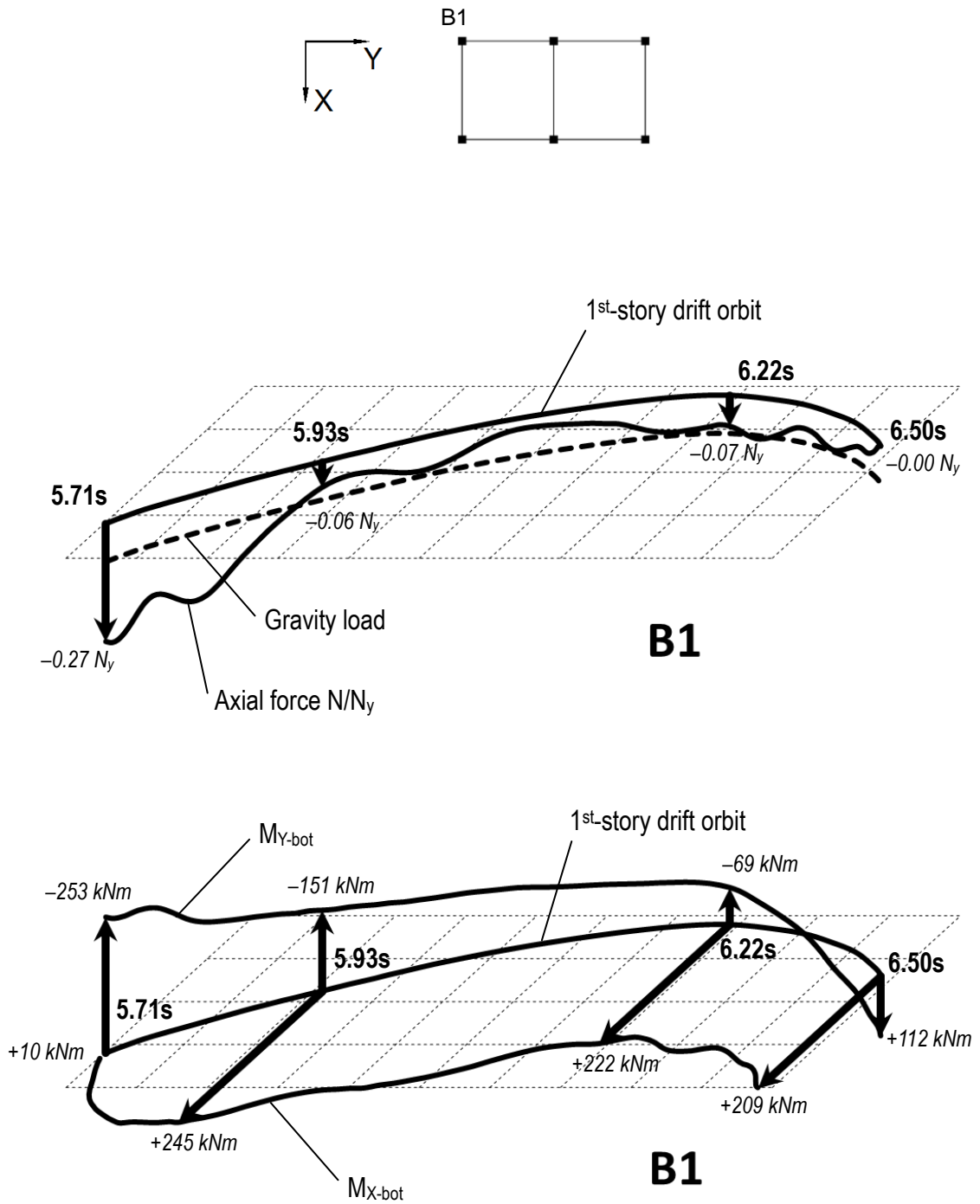
Figure 3.16 Column axial force and bottom moments tracing the 1st-story drift ratio orbit (5.71-6.50s, 100% Takatori, column B1).
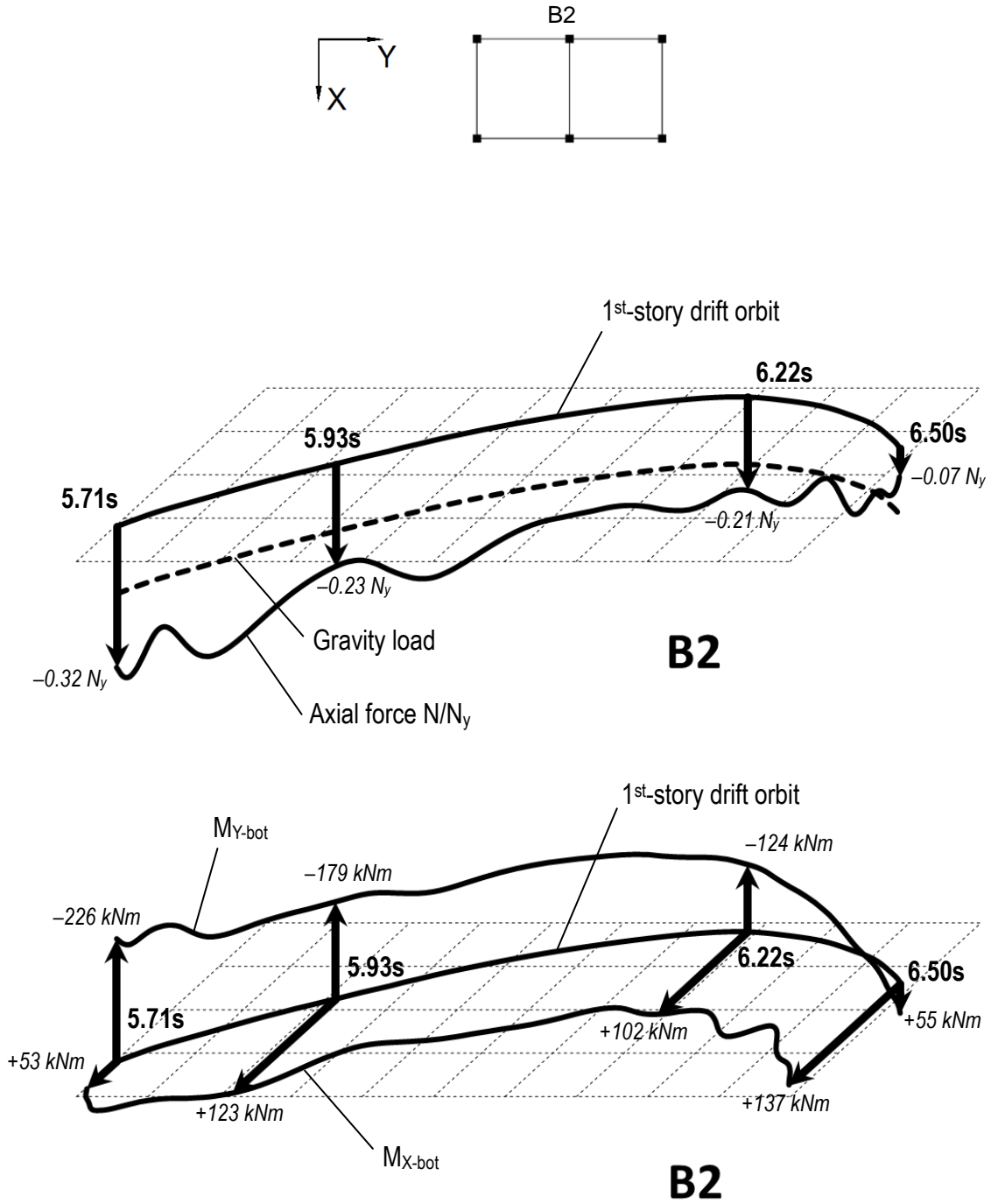
Figure 3.17 Column axial force and bottom moments tracing the 1st-story drift ratio orbit (5.71-6.50s, 100% Takatori, column B2).
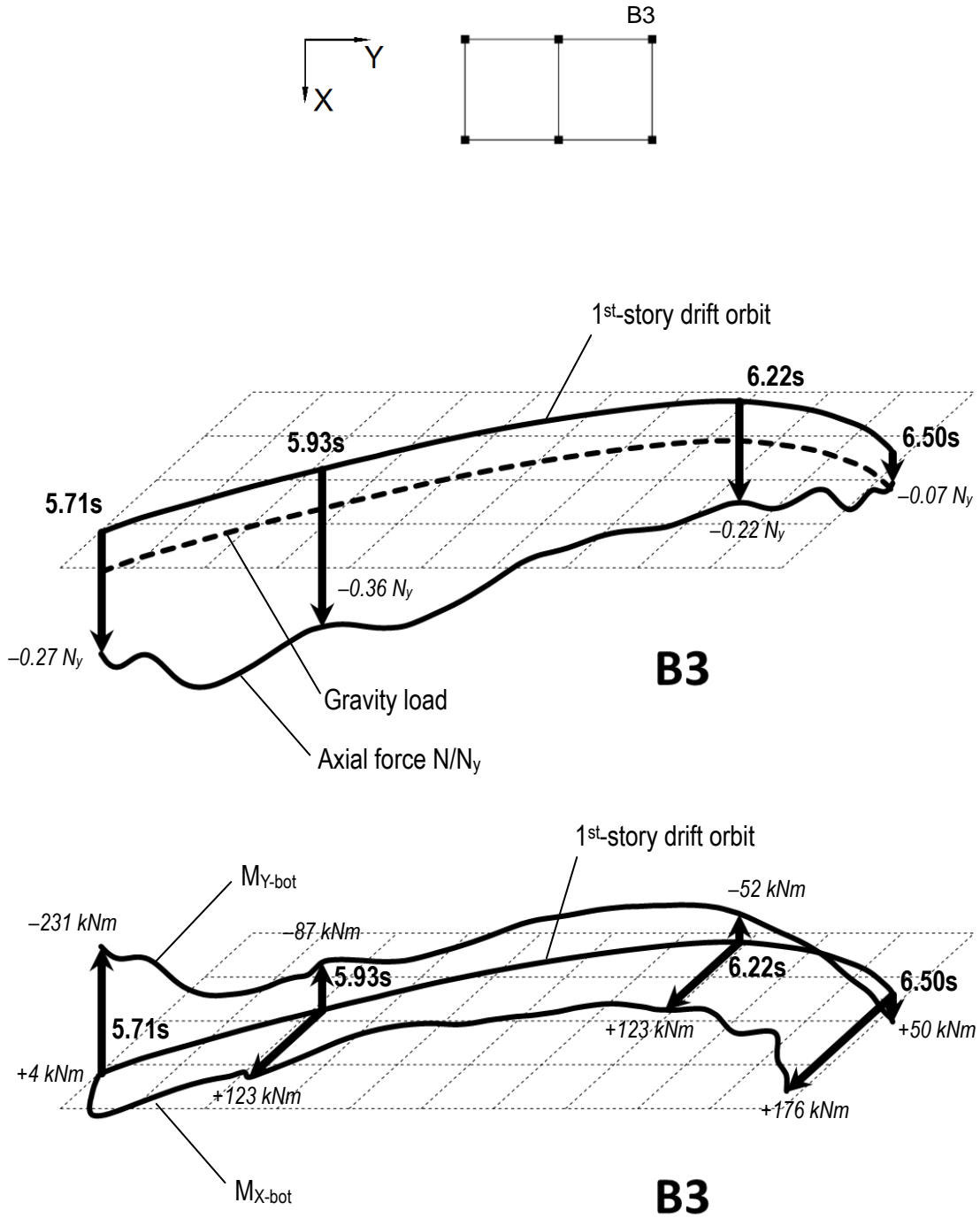
Figure 3.18 Column axial force and bottom moments tracing the 1st-story drift ratio orbit (5.71-6.50s, 100% Takatori, column B3).
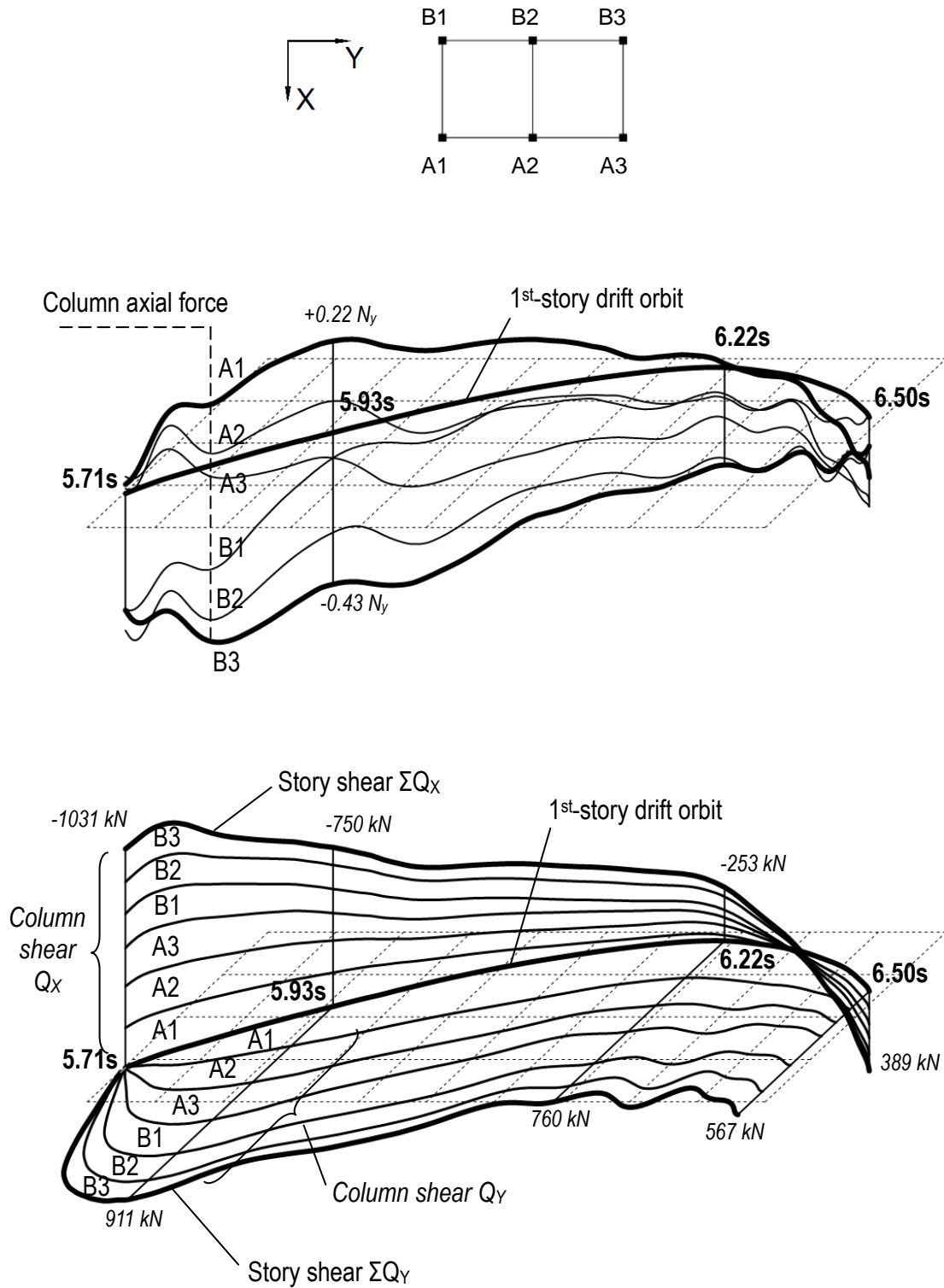
Figure 3.19 Column axial force and shear forces tracing the 1st-story drift ratio orbit (5.71-6.50s, 100% Takatori, whole frame).

3.3 Energy input and dissipation at various shaking levels

The earthquake input energy E_{in} (in either the X or Y direction) is calculated using the following equation, where m_i and $\dot{u}_i$ represent the lumped mass and the relative velocity of the ith floor with respect to the shake table, respectively; n is the number of stories; and $\ddot{u}_g$ is the shake table input acceleration:

$$E_{in} = -\int \sum_{i=1}^{n} \dot{u}_i m_i \ddot{u}_g dt \qquad (3)$$

Note that the energy in the equation is the relative energy based on the relative velocity and displacement between the structure and the ground (see Appendix A.3 for details).

Chopra [31] explained that the energy equation expressed in terms of relative motion is more meaningful than one expressed in terms of absolute velocity and displacement because the member forces and the energy dissipated by viscous damping or yielding depends only on the relative motion.

Additionally, Uang and Bertero [32] stated that the relative and absolute input energies are almost the same when the building natural period is within the range of 0.3 to 5.0 sec. Therefore, this study employs relative energy for the evaluation of building responses.

As in Section 2.4, the input and response energy quantities for 40, 60, and 100% Takatori motion levels are normalized to 20% Takatori motion for direct comparison (Figure 3.20) using the scale factor α = 1/2, 1/3, and 1/5, respectively.

As indicated by Equation (3), because there are two time-dependent quantities, i.e., the input ground acceleration $\ddot{u}_g(t)$ and the ith-floor response velocity $\dot{u}_i(t)$, the normalized earthquake input energy $\alpha^2 E_{in}$ is used in the graphical presentation in Figures 3.20(a)–(b) for the X and Y directions.
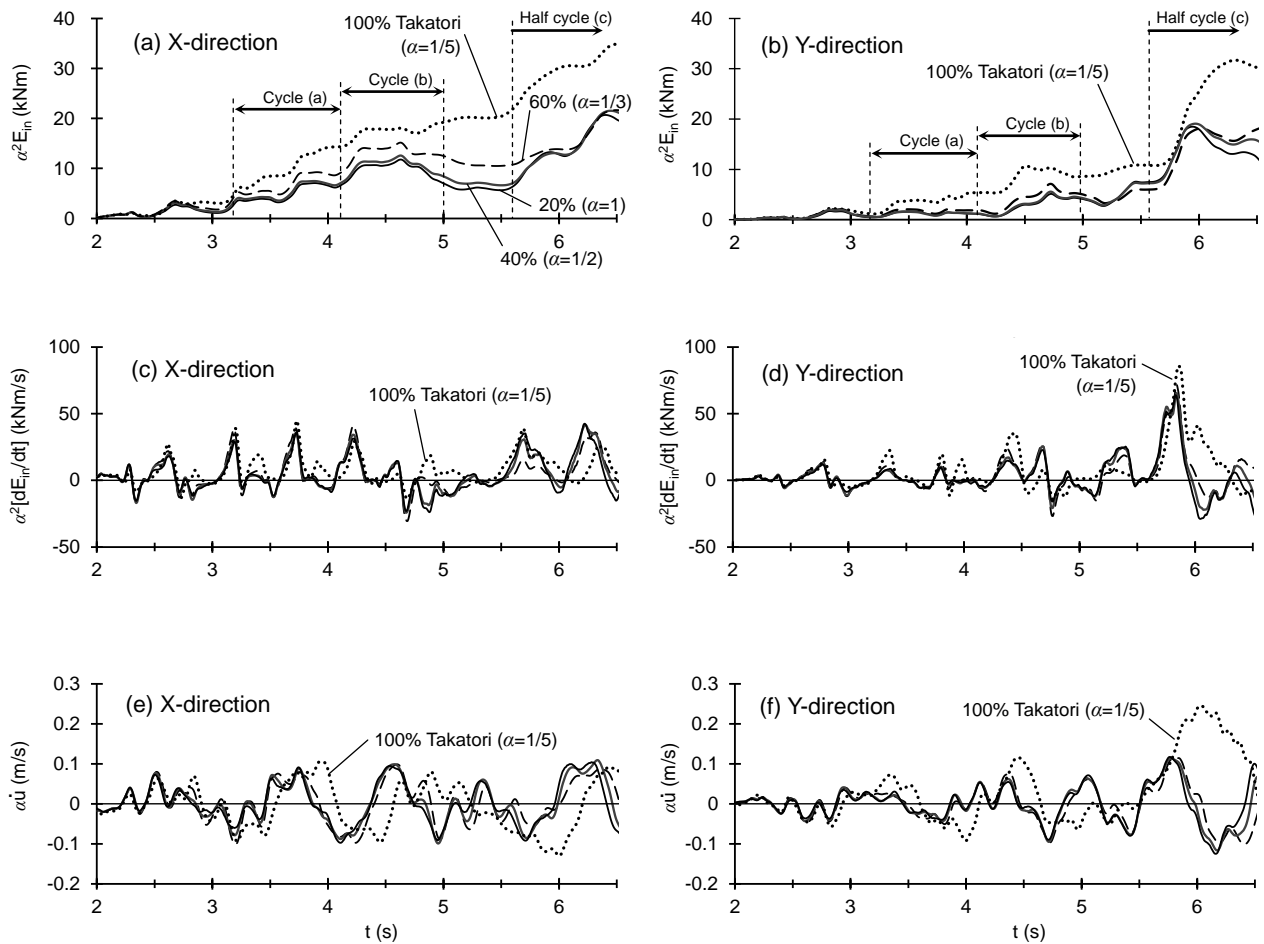
Figure 3.20 Time histories of normalized (a),(b) input energy, (c),(d) instantaneous input energy, and (e),(f) first-story relative velocity: scale factor $\alpha = 1$, 1/2, 1/3 and 1/5 for 20, 40, 60 and 100% Takatori levels, respectively.

Up to 40% Takatori level, $\alpha^2 E_{in}$ during the first two main cycles (a) and (b) was similar for all levels for both the X and Y directions. As yielding occurred, especially at the 100% Takatori level, $\alpha^2 E_{in}$ started to increase to nearly twice the values at previous levels. However, at each shaking level, the input energy in the X direction during these two cycles was approximately two to three times the input energy in the Y direction due to the stronger ground motion as well as larger response (Section 2.4).

The instantaneous input energy, defined as dE_{in}/dt, in the X direction [Figure 3.20(c)] was also very high during the first two main cycles and much larger than that in the Y direction [Figure 3.20(d)]. Moreover, from 5.7 to 6.0

sec, dE_{in}/dt in the Y direction increased to a remarkable peak [Figure 3.20(d)] and was similar for all excitation levels. As a result, $\alpha^2 E_{in}$ in the Y direction rapidly increased during this shaking period [Figure 3.20(b)], thereby causing greater dissipation demand in the frame and consequently very large displacements due to the deteriorated strength in the Y direction, as mentioned in previous sections. Figures 3.20(a)–(b) also show that $\alpha^2 E_{in}$ at collapse (and at the end, although not shown) are similar for the X and Y directions, thus suggesting that the above behavior cannot be predicted by such total input energy.

3.4 Energy dissipation at the collapse excitation level

The building response during the half cycle (c) at the 100% Takatori level can be interpreted using energy equilibrium. Because the 100% Takatori motion is 1.66 times greater than the 60% Takatori motion, its input energy should be $1.66^2 = 2.76$ times greater if the structure is elastic [refer to Equation (3)].

Figures 3.21(a)–(b) show the hysteretic relationship between the *base shear* $Q_{acc,Y}$ (based on floor inertial forces obtained from floor accelerations) and the *first-story drift ratio* r_Y within the half cycle (c) for the 60 and 100% Takatori levels, respectively. For the 100% Takatori level, because of the limited strength due to deterioration and the P-δ effect, the hysteretic branch greatly extended to dissipate the vertical striped area ΔE_{100} [Figure 3.21(b)] of 2.76 times the area ΔE_{60} [Figure 3.21(a)] enclosed by the 60% Takatori level from 5.7 to 6.0 sec. The dissipation of ΔE_{100} was finished even before 6.0 sec (i.e. 5.97 sec) because of the structural yielding.

In other words, within such a short time, the story drift r_Y had to quickly increase from zero to 0.064 rad (100% Takatori level), much greater than 0.019 rad (60% Takatori level). This explains the bifurcation of the *relative story velocity* $\dot{u}_Y$ history at 100% Takatori level [Figure 3.20(f)] at 5.7 sec, causing its response to be completely different from those for previous motion levels.
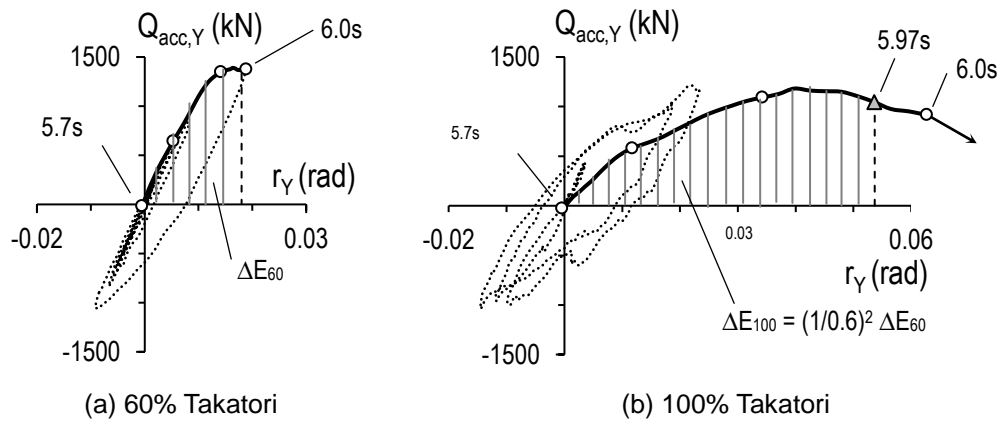
Figure 3.21 Hysteretic graphs characterizing the energy dissipation demand of the first story within the time from 5.7 to 6.0 sec in the Y direction, at (a) 60% and (b) 100% Takatori levels.
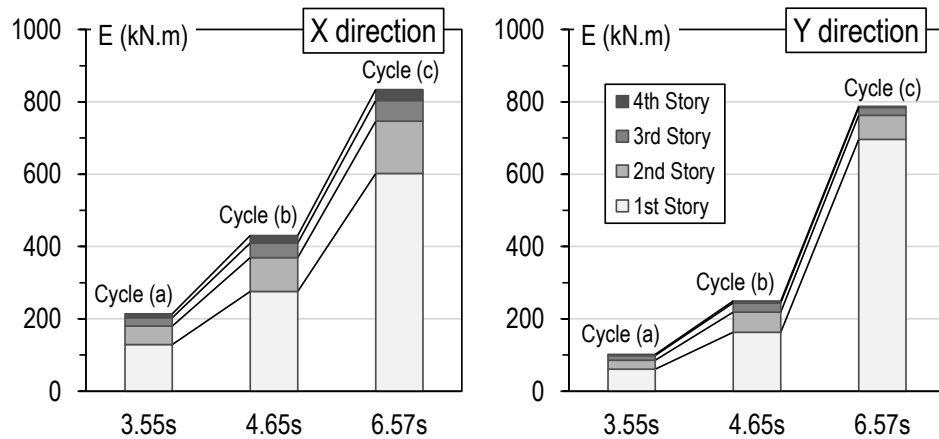
Figure 3.22 Accumulated energy dissipation per story at three points of time in three main cycles during the 100% Takatori loading.

However, because the exceedingly large amount of instantaneous input energy in the Y direction needed to dissipate within a short time, the peak $\dot{u}_Y$ at 6.0 sec [Figure 3.20(f)] was more than twice that of $\dot{u}_X$ [Figure 3.20(e)]. Consequently, the building rapidly translated and collapsed in the Y direction, although the total input energies in the X and Y directions were nearly equal [Figures 3.20(a)–(b), respectively], as mentioned in Section 3.3. Therefore, this is an important issue in evaluating and predicting the vulnerable side of the building displacement response; *maximum instantaneous input energy* is thought to play a more important role than *total input energy* in determining the main response of the structure.

Figure 3.22 plots the breakdowns of accumulated energy distribution per story in the building in the X and Y directions, at three selected times of three cycles. From bottom to top, the levels indicate the energy dissipation by the first, second, third and fourth stories. The energy dissipation was dominant in the first story, indicating the significant yielding activity in this story level. On the other hand, because the earthquake input energy was larger in the X direction than in the Y direction during the first two cycles (a) and (b), the energy dissipation was also more dominant in the X direction than in the Y direction. However, with the sudden increase of earthquake input energy in the Y direction during the last cycle (c), the rapidly dissipated energy was mostly concentrated in the first story causing the soft-story collapse mechanism in the Y direction. On the other hand, as the story drift increased remarkably, the work done by gravity due to the P-δ effect also increased. Until the collapse time, the work done by gravity was approximately 20% the energy dissipated by the first story, causing more damage to the structure.

3.5 Summary

This chapter addressed the behavior of the columns subjected to simultaneous biaxial moment - axial force, and their deterioration due to local buckling, consequently causing decrease in base shear capacity, and eventual structural collapse.

- At 100% Takatori motion level, the panel zones experienced strain hardening, and their capacity exceeded the local buckling capacity of the columns. As the story drift continued increasing, deterioration of the first-story columns occurred due to local buckling at the column ends. Panel zones were unloaded and returned to be elastic, causing substantially more drift demand to the deteriorated first-story columns. A soft-story mechanism was initiated, and the building collapsed.

- Experimental results show totally different deteriorating patterns of biaxial bending moments amongst all six columns because their axial

force magnitudes differ considerably due to the column locations. Shifting of the principal direction of the biaxial bending moments cycle by cycle also caused the initiating damage of column section in one direction and consequently reducing the resistant capacity in the other direction. The column deterioration evolution is clarified and detailed from these perspectives.

• Moreover, the building response can be interpreted in terms of energy, in which energy input and the dissipation mechanism at the collapse excitation state are evaluated. Although the total accumulated input energies were very similar in both directions, the input energy in the X direction increased gradually, whereas the input energy in the Y direction had a suddenly large instantaneous amount needed to dissipate within a short time by the frame with limited strength due to deterioration, thereby resulting in the rapid translational response and collapse of the first story mainly in the Y direction. As the P-δ effect increased, the building consequently lost stability and eventually collapsed. Therefore, the maximum instantaneous earthquake input energy should be of greater interest in predicting structural response in seismic design.

CHAPTER 4

COLUMN ANALYSES SIMULATING TWO-DIRECTIONAL
DETERIORATIONS

<div align="center">Chapter 4</div>

COLUMN ANALYSES SIMULATING TWO-DIRECTIONAL DETERIORATIONS

4.1 Concept of simulating local buckling by fiber hinge element

Fiber element method was employed in this study, where the buckling zone at the column ends is modeled as a *fiber hinge element* composed of *fibers* that can deteriorate due to buckling effect, distributed over the cross section [Figure 4.1(a)]. The hinge zone conveniently has zero length, unlike the other fiber beam element approach requiring mesh generation for expected yield zone length. Its rotation characteristic is achieved by its presumed finite length l_h of buckling zone (same approach as [33]). For the present tube column, l_h is set equal to the column depth based on the observations from experiment.

The nonlinear stress-strain properties of a fiber element [Figure 4.1(b)] stipulated by this finite length comprises two modeling rules. First, the cyclic stress-strain hysteresis rule reflects the experimental buckling behavior of steel struts by Black *et al.* [34] with the simplification of considering no strain hardening.

The first zone O-A [Figure 4.1(b)] is associated with the initial loading of the element which approaches the critical buckling stress (assumed to be equal to σ_y) at point A. Zone A-B-C is characterized by a decreasing load accompanied by element shortening and buckling. Zone C-D-E-F is the compression unloading and tensile loading of the fiber element. Subsequent hysteretic loops have the same characteristic except that the consecutive peak

compressive stresses are reduced due to deterioration caused by the previous inelastic cycling of the material. Hence, the compressive yield stress at point G, where the element begins to yield in compression, is set equal to the value of compressive stress at point C. Point C is named for the reversal location of the curve when the element shortening stops. This location changes per load cycle. Accordingly, the curve continues to approach point H and thereafter along zone H-H' on the backbone curve.
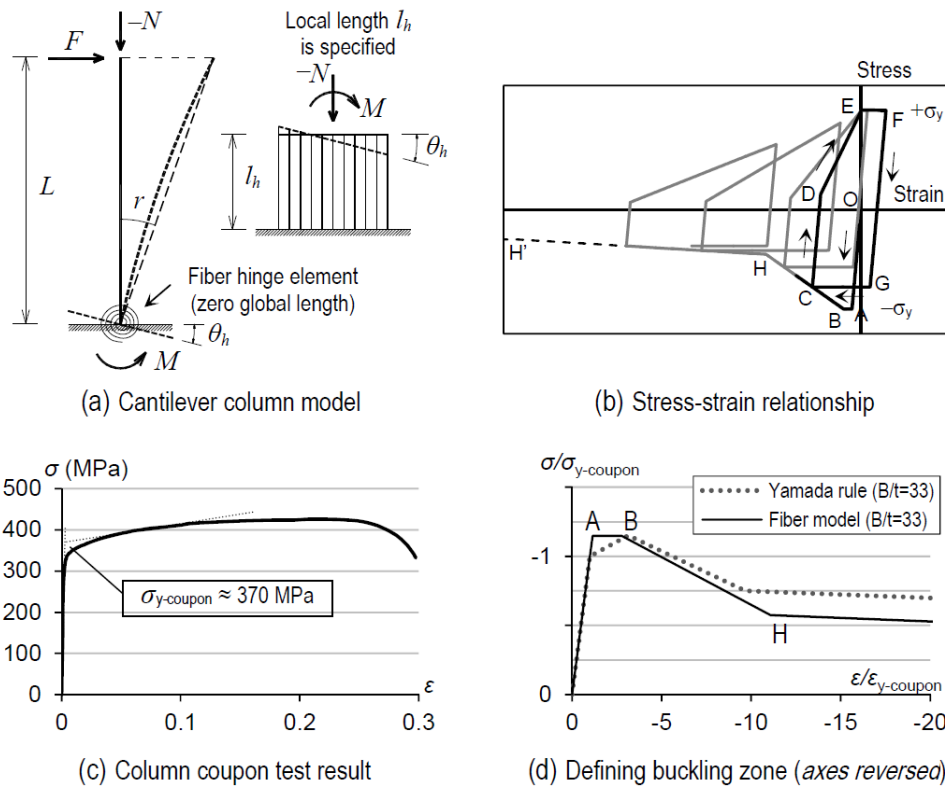
Figure 4.1 (a) Structural model, (b) material property of fiber hinge element, (c) column coupon test result, and (d) calibration for compression side based on the existing prediction rule for local buckling.

Second, the degradation rule for the compressive buckling zone is specified by considering Yamada *et al.*'s [35] axial stress-strain rule constructed from pure compression tests of stub columns with *b/t* ratios varying from 15 to 35. As shown by Figure 4.1(d), the rule was utilized for initial setting of the fiber model for the present column section (*b/t* = 33). Significant circumferential restraint at the column end causes either bi-axial

tensile or bi-axial compressive in-plane stresses and consequently increases the yield stress in the axial direction, as evidenced by FEM analysis (Section 4.2). Thus, the model considers fiber yield stress $\sigma_y = 1.15\sigma_{y\text{-coupon}}$, where $\sigma_{y\text{-coupon}} = 370$ MPa from coupon test and bi-linear approximation [Figure 4.1(c)]. Also according to [35], the experimental peak moment for $b/t = 33$ was approximately 1.15 times the plastic moment. The calibration of fiber properties for better simulation will be discussed hereafter in Section 4.2.

4.2 Simulations of columns under simple one-directional bending

The calibration of fiber properties is validated by the numerical simulation for the associated cyclic component test conducted prior to the collapse experiment. As shown in Figure 4.2, the cantilever box column RHS-300×300×9 (identical to the member in the test building) was subjected to cyclic lateral load and constant compression load of –500 kN (approximately –0.15N_y), applying two types of 0° and 45° loading directions.

For the analytical cantilever model, in order to eliminate the additional flexibility due to the finite length l_h of the fiber hinge, the column portion (length L) is stiffened by the factor of $L/(L – 3l_h)$. This factor makes horizontal stiffness equal to the case of the column without fiber hinge. It assumes the inflection point location at mid-height of the column, which was approximately the case in the building experiment.

To validate the analytical results by the model using fiber hinge element (noted as *Fiber model*), as well as utilize for some additional loading schemes as will be discussed later on, another analytical cantilever column model using finite element method (noted as *FEM model*) is constructed. Details of the *FEM model* are given in Appendix A.2. Figure 4.2 shows the agreement between the analytical results of moment-rotation relationship obtained by both *Fiber* and *FEM models* (represented by *solid line*) with the experimental records (*dashed line*).
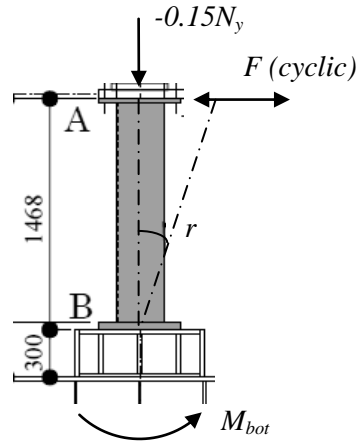
Component test setup
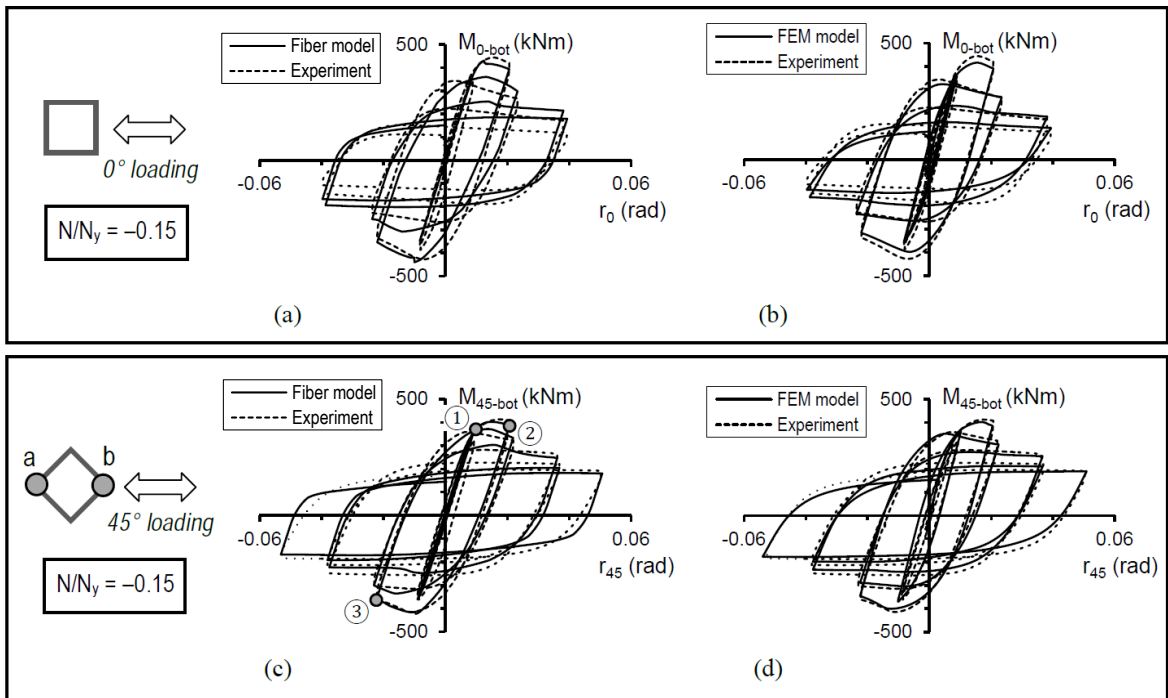
Figure 4.2 Comparison of the hysteretic load–deformation curves between records of the cyclic cantilever column test and analytical results by two types of Fiber model and FEM model.

The agreement is found on not only moment responses but also local element stress behaviors between the analytical results by *fiber model* and *FEM model* represented by solid and dashed lines, respectively (Figure 4.3). Because the building displacement observed during the excitation before collapse was oriented diagonal in plan and mainly oscillated in nearly the 45°-direction, the following discussion focuses on column bottom moment with respect to the 45°-direction, namely $M_{45\text{-bot}}$. Accordingly, the corresponding chord rotation along this 45°-direction, namely r_{45}, is also considered.

The analysis considering monotonic loading [Figure 4.3(b)] is selected to demonstrate. Figures 4.3(c)–(d) show the relations between column chord rotation r_{45} and normalized axial stresses of two corner fibers "*a*" and "*b*" [Figure 4.3(a)] subjected to the largest tensile and compressive effects, respectively. The yield stress of FEM model is also higher than the one by coupon test $\sigma_{y\text{-coupon}}$, verifying the necessity of increasing axial yield stress in the fiber model.

The analytical normalized axial stress variations in the 45°-direction of the column end's cross section at some points related to Figure 4.3(b): A (start of loading), B (rotation $r_{45} = 0.01$ rad), C (0.02 rad) and D (0.03 rad) are plotted in Figures 4.3(e)–(h), respectively.

Elasticity is shown apparently at the loading start [Figure 4.3(e)]. Nonlinearity appears to begin at the rotation of 0.01 rad [Figure 4.3(f)] where some outermost elements reached yield capacity. Especially, at the rotation of 0.02 rad [Figure 4.3(g)] most of the elements on the compression side yielded, and even some of them in the FEM model buckled. After that, the buckling became more severe at the rotation of 0.03 rad [Figure 4.3(h)], thereby reducing the resisting moment capacity at point D as shown in Figure 4.3(b). Both of the models simulated efficiently the column deterioration caused by local buckling.
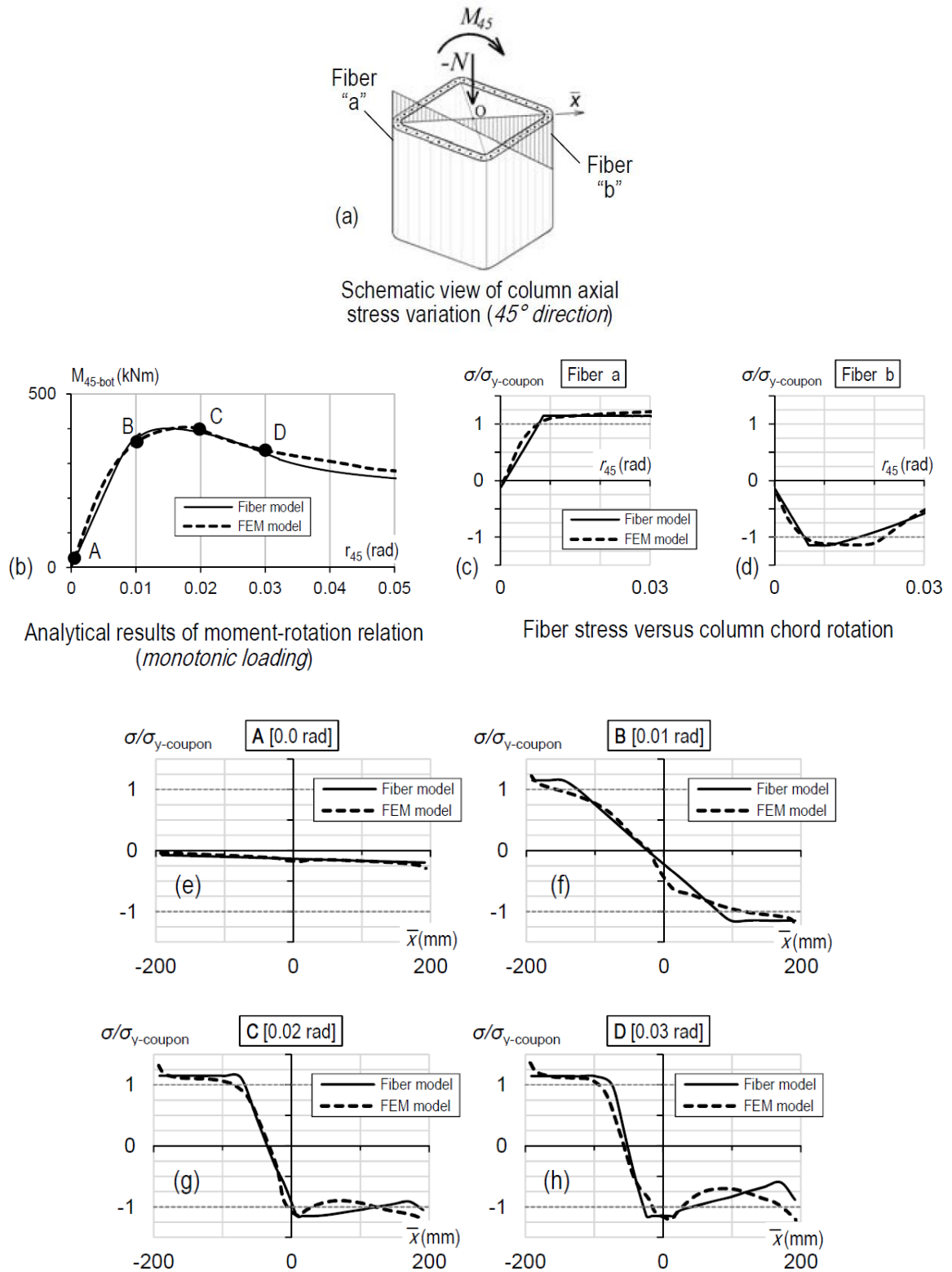
Figure 4.3 (a) Schematic view of column fibers; (b) analytical column moment-rotation relation considering monotonic loading; relations between column chord rotation and normalized axial stresses of (c) fiber "a" and (d) fiber "b"; and the analytical column normalized axial stress variations at selected instants: (e) A, (f) B, (g) C, and (h) D.

As presented earlier in Section 3.1, the fiber calibration can be explained by comparing the analytical results considering two types of *perfectly bilinear elastoplastic* and *buckling* fiber properties as shown in Figures 4.4(a)–(b), respectively.

Stress-strain relationships of two corner fibers "*a*" and "*b*" are selected to illustrate the fiber calibration. At point ①, fibers "*a*" and "*b*" start tensile and compressive yieldings, respectively. During yielding until the unloading point ② [fiber "*b*", Figure 4.4(b) right], the fiber buckling is modeled to start at compressive strain of approximately $2.5\varepsilon_y$ [point B, Figure 4.1(b)] where ε_y is the fiber yield strain, and then the fiber degradation starts.

Moment deterioration in the consecutive half cycle up to the next unloading point ③ is captured by the degradation of fiber "*a*" which is subsequently under compression. The stress of the buckled fiber beyond compressive strain of $10\varepsilon_y$ [point H, Figure 4.1(b)] is set to remain as $0.5\sigma_y$, slightly modified from the prediction rule [Figure 4.1(d)] for better simulating the experimental cyclic degradation of column moment.
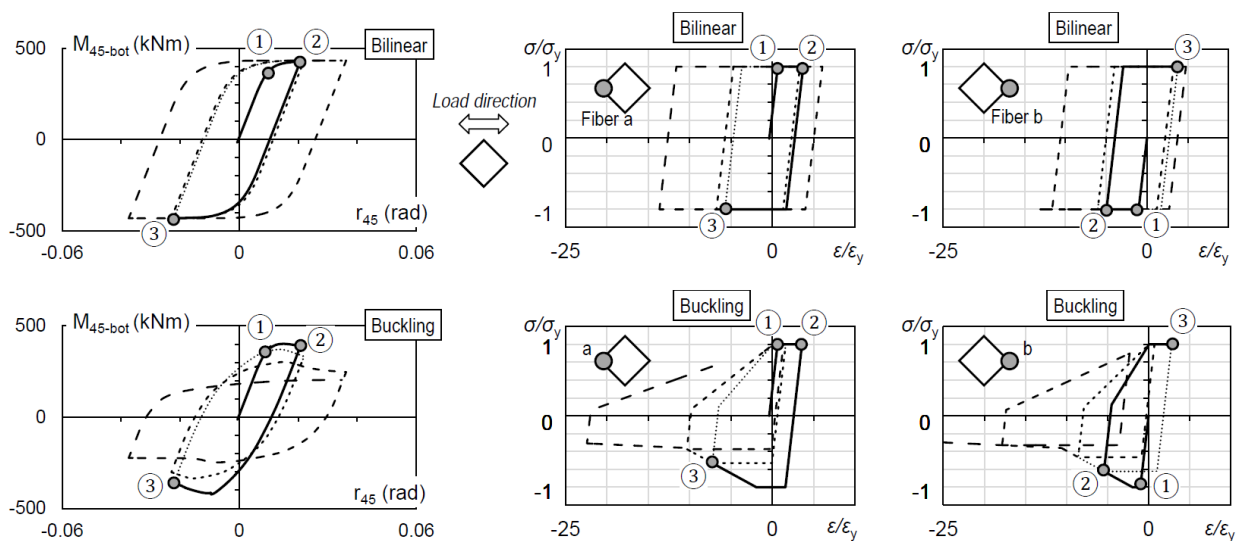
Figure 4.4 Comparison of the analytical hysteretic load–deformation and selected fiber's stress-strain relationship by two types of fiber properties under $N/N_y = -0.15$: bilinear type (upper row) and buckling type (lower row).

In order to demonstrate the effect of axial load on the deteriorating column moment behavior, two further hypothetical cyclic cantilever column analyses were conducted, using the similar lateral displacement loading history but varying the constant axial loads into two cases: *large tension* ($+0.2N_y$) and *critical compression* ($-0.4N_y$).

A series of load–deformation hysteretic and skeleton curves for different levels of constant axial loads $N/N_y = +0.2$; -0.15; and -0.4 are shown in Figures 4.5(a)–(c), respectively. Note that there are two types of skeleton curves displayed in those figures: the thick line is the envelop skeleton obtained from cyclic loading, and the dotted line is obtained by monotonic loading.
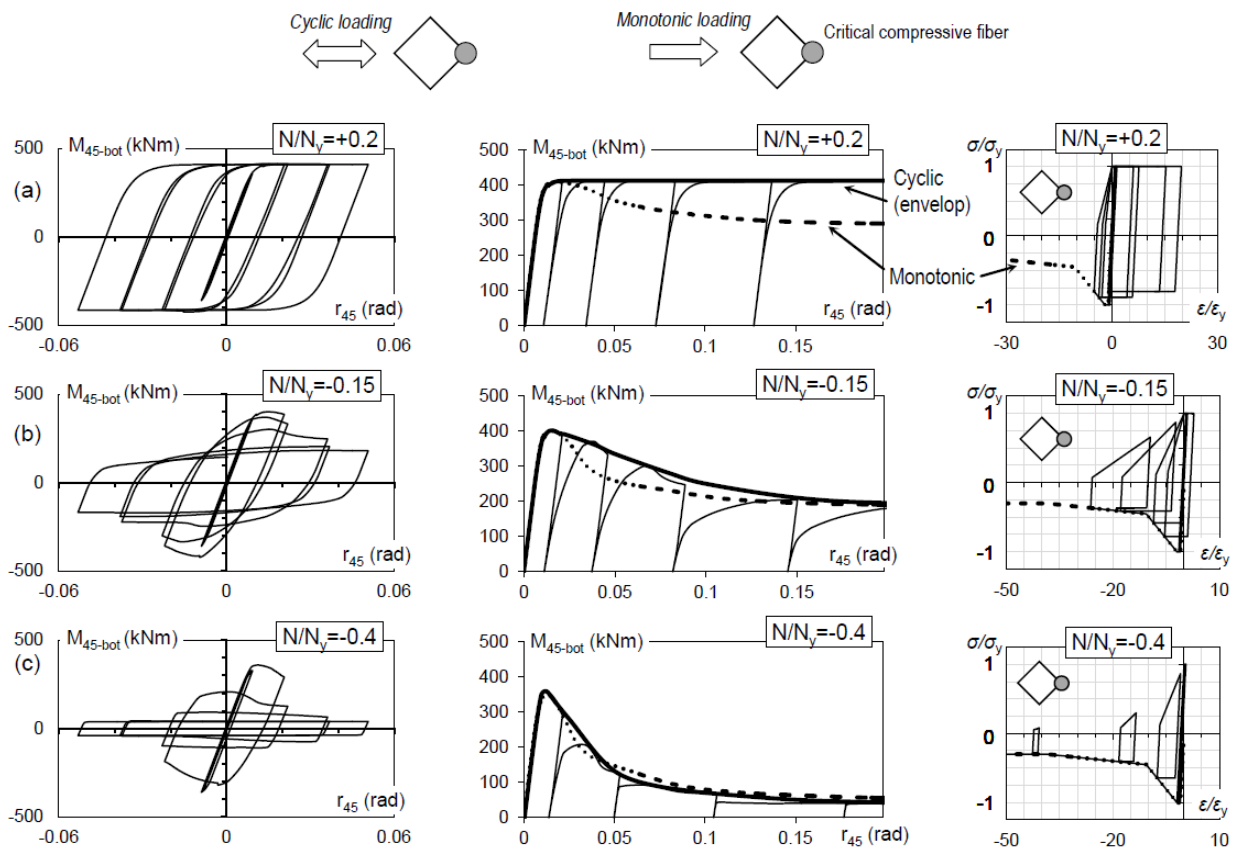
Figure 4.5 Cantilever column's analytical results using fiber hinge element with two types of cyclic (solid line) and monotonic (dotted line) loadings, expressed by hysteretic load–deformation curves (left), skeleton curves (middle) and the selected critical compressive fiber's stress-strain relationship (right) for different levels of constant axial loads: (a) $N/N_y = +0.2$; (b) $N/N_y = -0.15$; and (c) $N/N_y = -0.4$.

Cyclic behavior of the analytical column model under tension $N/N_y = +0.2$ [Figure 4.5(a)] appears to remain strong and stable even during the large loading excursion. However, when subjected to monotonic loading, it starts to show a slight degradation at the rotation angle of approximately 0.02 rad and reduces to 0.75 times its original strength at deformation of 0.2 rad.

This can be explained by the stress-strain relationship of the selected fiber element located at the column corner and it consequently suffers the most critical compression effect due to the bending moment in 45°-direction loading [Figure 4.5(a) right]. The dotted line representing the fiber response by monotonic loading degrades rapidly when the applied stress is large enough to cause buckling strain. Thus, the column becomes weakened even under small deformation.

In contrast, that fiber experiences the sequence of compression–unloading–tension–yielding–unloading in case of cyclic loading, thereby not only its tensile and but also its compressive strength remains almost stable, keeping the global hysteretic column moment behavior nearly without deterioration, as shown by its flat skeleton curve [Figure 4.5(a) middle].

The effects of compressive axial force are shown in Figures 4.5(b)–(c) for two levels of $N/N_y = -0.15$ and -0.4, respectively, where the moment skeleton responses due to both monotonic and cyclic loadings are relatively similar. The difference of fiber stress-strain hysteretic relationships among three levels of constant axial loads as shown in Figure 4.5 (right) can visualize the different weakening behavior at the vicinity of the column bottom end due to local buckling in those cases.

Under the large compression load, the fiber hysteretic curve has more likelihood to enter the buckling zone and reduce strength in the subsequent load cycles. Therefore, the moment capacity consequently becomes smaller than its peak strength in the previous cycles. The fiber hinge element can account for the axial force effect on moment.

4.3 Simulations of columns under complex two-directional bending

To demonstrate the influence of axial force on the deteriorating behavior of column moment as well as the two-directional moment deterioration, a series of hypothetical cyclic bending of cantilever column analyses are conducted for both *Fiber model* and *FEM modes*, applying the constant axial loads into three different levels: *large tension* ($+0.2N_y$), *moderate compression* ($-0.15N_y$) and *large compression* ($-0.4N_y$). The technique of two-directional displacement control (Figure 4.6) is applied to the cantilever column model, wherein the tip end is subjected to two types of elliptical cyclic loading as follows.
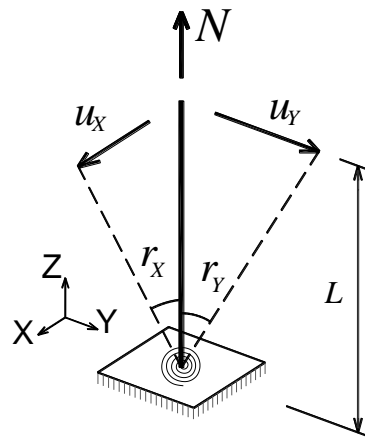
Figure 4.6 Axial force and two-directional lateral displacement loading applied to the analytical cantilever column model.

4.3.1 Load type 1

The first type of elliptical displacement loading is shown in Figure 4.7, where r_X and r_Y represent the chord rotation angles along the X and Y axes, respectively. Their loading histories are displayed in Figure 4.7(a). The width-to-length ratio of the elliptical loop is 0.2. The column model firstly experiences loading in the r_X direction from point O to point A [Figure 4.7(b)]. Note that the horizontal axis is used to represent r_Y, and the vertical axis representing r_X is reversed to make the coordinates appear consistent with

those of the full-scale building presented earlier in Figure 2.1(c) (Section 2.1). The column then starts the elliptical loop A–B–A [Figure 4.7(c)] and repeats the loop until changing to the r_Y direction loading at point C [Figure 4.7(d)], finally finishes two elliptical loops C–D–E along the r_Y direction [Figure 4.7(e)].
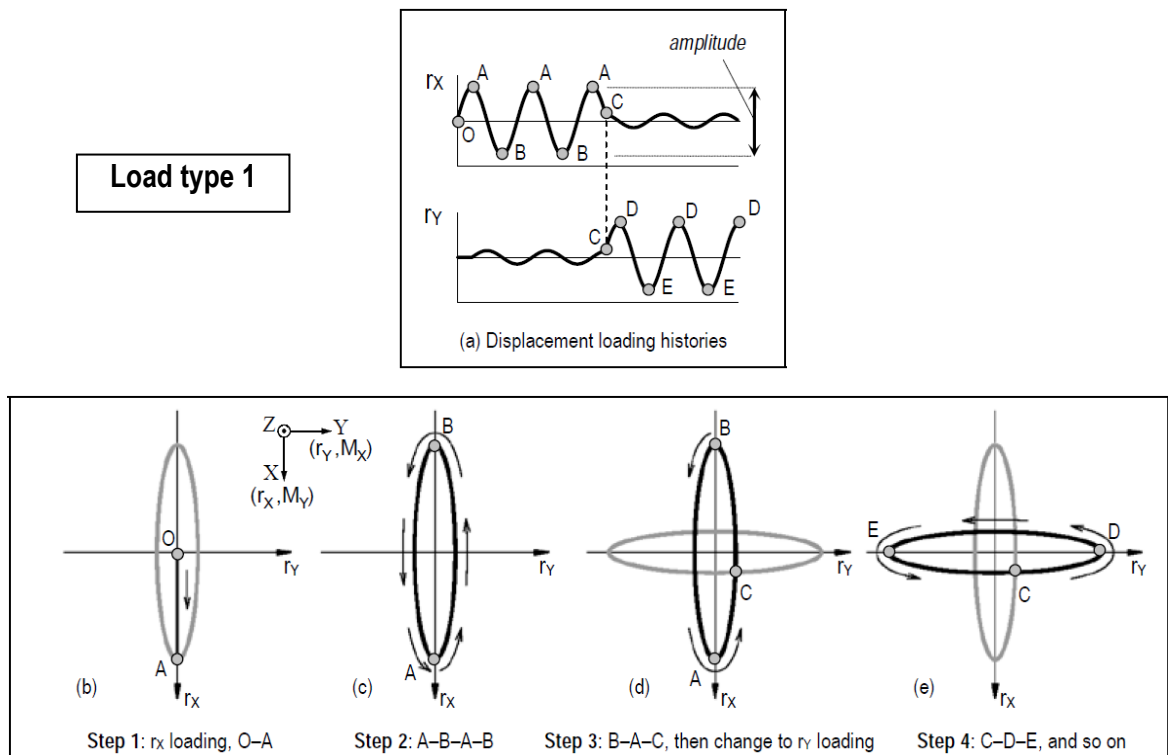
Figure 4.7 Elliptical loading scheme of two-directional lateral displacement applied to the cantilever column analyses (*Type 1*).

Initially, the loading type with small amplitude ±0.015 rad (noted as *type 1-a*) is applied to both r_X and r_Y, expecting the inelastic and yielding response of the column model. Figure 4.8 displays the analytical results of the *Fiber model* and *FEM model* represented by *black* and *gray* solid lines, respectively. Three groups of graphs related to three constant axial force levels N/N_y = +0.2, −0.15 and −0.4 are shown in Figure 4.8. Within each group, the upper graph plots the interacting relation between $M_{X\text{-bot}}$ (horizontal axis, related to r_Y) and $M_{Y\text{-bot}}$ (vertical axis, related to r_X) as well as the yield surface represented by dotted line. Note that the vertical axis is also reversed to define the moment coordinates consistent with the displacement coordinates

presented earlier in Figure 4.8. The two lower graphs in each group show the hysteretic relationships "$M_{Y\text{-bot}}$ vs. r_X" and "$M_{X\text{-bot}}$ vs. r_Y" from left to right, respectively. Some major points corresponding to the peak displacement of the first loop in each loading direction (referred to Figure 4.7), such as A and B (for r_X loading); C (for the direction changing point); D and E (for r_Y loading), are selected to show on those graphs in Figure 4.8.

In overall, the analytical results by *Fiber model* almost agree with those by *FEM model*. The different moment response depending on the axial force magnitude can be well simulated by both models. Under tension [Figure 4.8(a)] for the small loading amplitude of ±0.015 rad deformation, the moment yield surface does not change significantly when the loading direction is shifted from the X axis to the Y axis. However, the yield surface tends to shrink if the column is subjected to moderate compression [Figure 4.8(b)] and large compression [Figure 4.8(c)].

In other words, the column under tension does not show any much difference between responses of $M_{Y\text{-bot}}$ [Figure 4.8(d)] and $M_{X\text{-bot}}$ [Figure 4.8(e)]. The deteriorating effect of $M_{X\text{-bot}}$ caused by the preceding yielding/degrading of $M_{Y\text{-bot}}$ is shown when the column is subjected to compression force [Figures 4.8(f)–(i)]. With the similar r_Y and r_X deformation amplitudes in this loading *type 1-a*, the analytical results by *Fiber model* predicted the peak $M_{X\text{-bot}}$/peak $M_{Y\text{-bot}}$ ratios to be 0.88 and 0.32, whereas the results by *FEM model* estimated those ratios to be 0.76 and 0.31, for two axial force levels of $-0.15N_y$ and $-0.4N_y$, respectively.

Additionally, the loading type 1 is repeated with the larger amplitude of ±0.03 rad deformation (noted as *type 1-b*) applied to both r_X and r_Y, expecting the inelastic and local buckling response of the column model. Figure 4.9 displays the analytical results of the *Fiber model* and *FEM model* represented by *black* and *gray* solid lines, respectively, with the same arrangement of graphs as those presented in Figure 4.8.

Load type 1-a
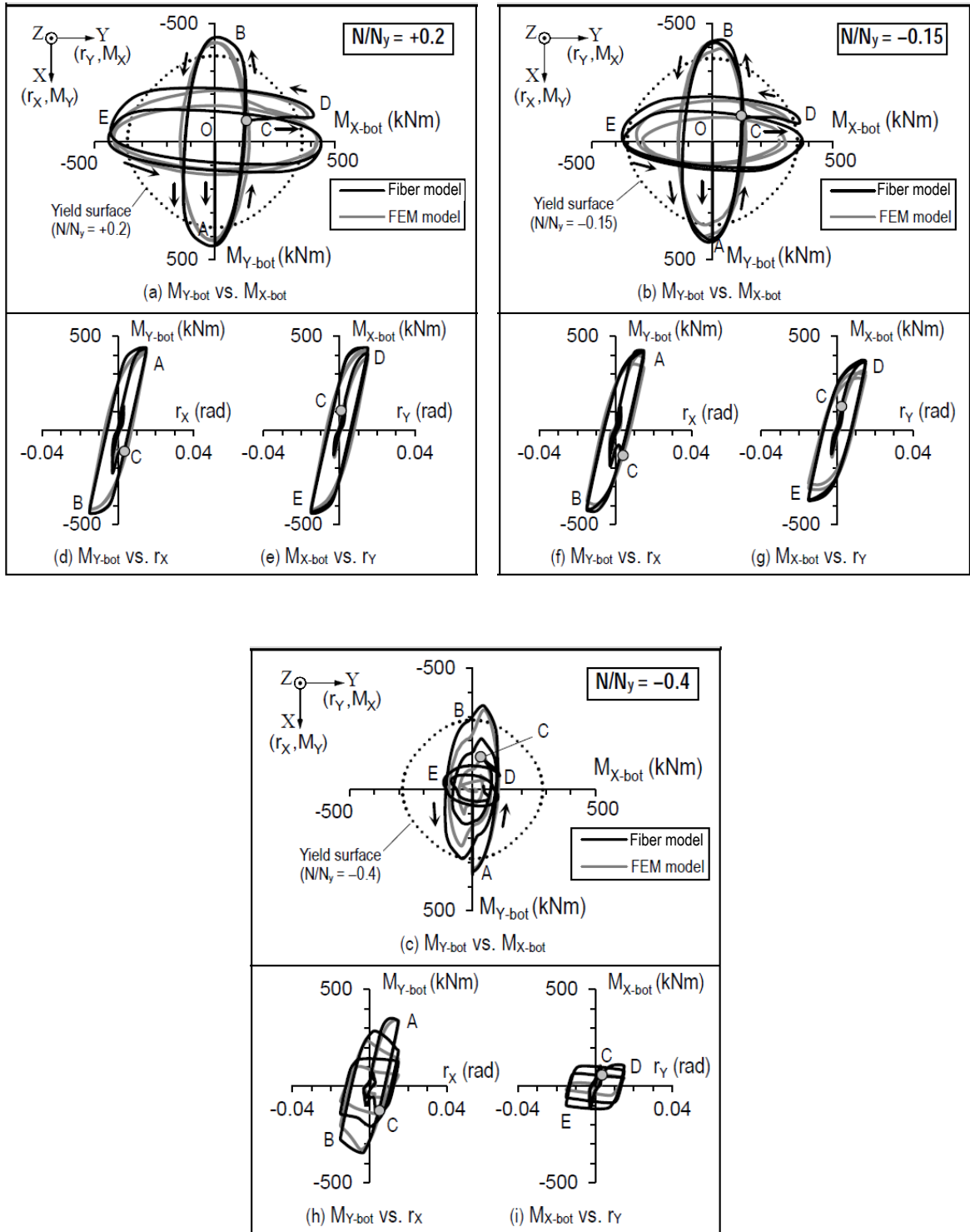
Figure 4.8 Analysis results of column bottom moments for loading type 1-a (small deformation amplitude ±0.015 rad).
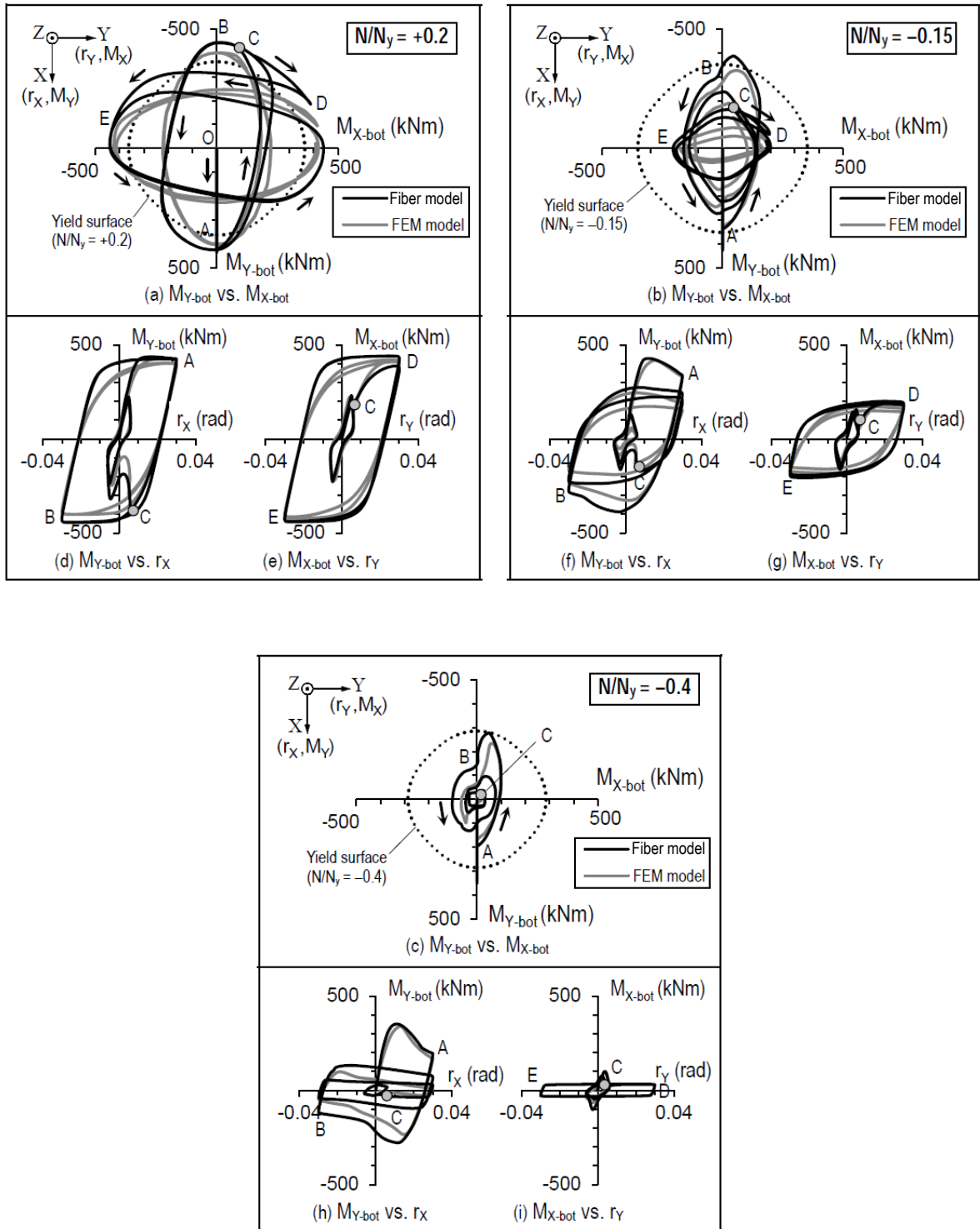
Figure 4.9 Analysis results of column bottom moments for loading type 1-b (large deformation amplitude ±0.030 rad).

The column under tension appears to remain stable responses characterized by its stable yield surface [Figure 4.9(a)], whereas the columns under moderate compression [Figure 4.9(b)] and large compression [Figure 4.9(c)] experience significant shrinkage of their yield surface. Deterioration of moment starts to display when the deformation angle exceeds 0.015 rad [*e.g.* Figure 4.9(f)]. In the loading *type 1-b*, the peak $M_{X\text{-bot}}$/peak $M_{Y\text{-bot}}$ ratios were estimated to be 0.47 and 0.28 (by *Fiber model*), whereas they are 0.44 and 0.29 (by *FEM model*) for two levels of $-0.15N_y$ and $-0.4N_y$, respectively.

4.3.2 Load type 2

Differently from the abovementioned loading scheme considering the loops in the pure r_X direction followed by other loops in the pure r_Y direction, the new scheme (noted as *type 2*) counts for the random loading direction changing cycle-by-cycle. The elliptical displacement loading histories are displayed in Figure 4.10(a). The width-to-length ratio of the elliptical loop is 0.2, similar to the previous *type 1*.

The column model firstly experiences loading from point O to point A [Figure 4.10(b)], then starts the two elliptical loops A–B–A [Figure 4.10(c)] with the direction of 66° with respect to the $+r_Y$ axis, until changing loop at point C [Figure 4.10(d)], and finally finishes the third elliptical loop C–D–E [Figure 4.10(e)] with the direction of 29° with respect to the $+r_Y$ axis. Deformation amplitude is set approximately ±0.02 rad for r_X and -0.015 to $+0.03$ rad for r_Y directions.

Those loop directions and amplitudes were idealized from three main cycles of the 1st story drift ratio orbit recorded in the collapse experiment, as presented earlier in Figure 3.5 (Section 3.1). This type of loading is utilized as a preliminary analysis estimating column moment behavior in the collapse test considering constant axial force condition. Further complicated analyses counting for the alternating tension/ compression forces will be discussed later in Section 4.4.
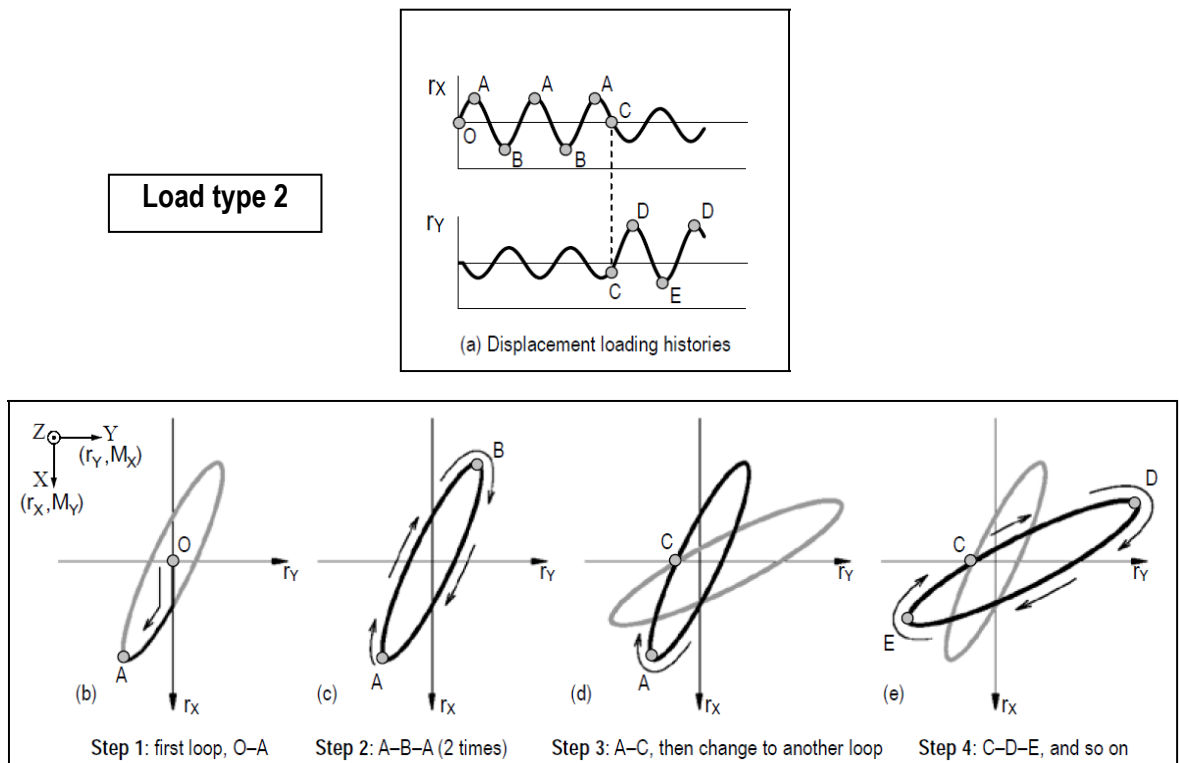
Figure 4.10 Elliptical loading scheme of two-directional lateral displacement applied to the cantilever column analyses (Type 2).

Figure 4.11 displays the analytical results of the *Fiber model* and *FEM model* represented by *black* and *gray* solid lines, respectively, with the similar arrangement of graphs as those presented in Figure 4.8. During the first two cycles, the displacement loops are close to the r_X direction. Therefore, $M_{Y\text{-bot}}$ develops more rapidly than $M_{X\text{-bot}}$. If the column is under tension, $M_{Y\text{-bot}}$ experiences just a slight degradation [points A and B, Figure 4.11(d)], which does not reduce the capacity of $M_{X\text{-bot}}$ so considerably in the third cycle [point D, Figure 4.11(e)]. During the loading time from points C to D (increasing both r_Y and r_X deformations), since the column moment follows the margin of yield surface, only $M_{X\text{-bot}}$ can develop [Figure 4.11(e)] but $M_{Y\text{-bot}}$ has to decrease Figure 4.11(d)]. However, it does not indicate column deterioration because the column can still remain its capacity in the subsequent cycles, characterized by the almost stable yield surface [Figure 4.11(a)] until the end.
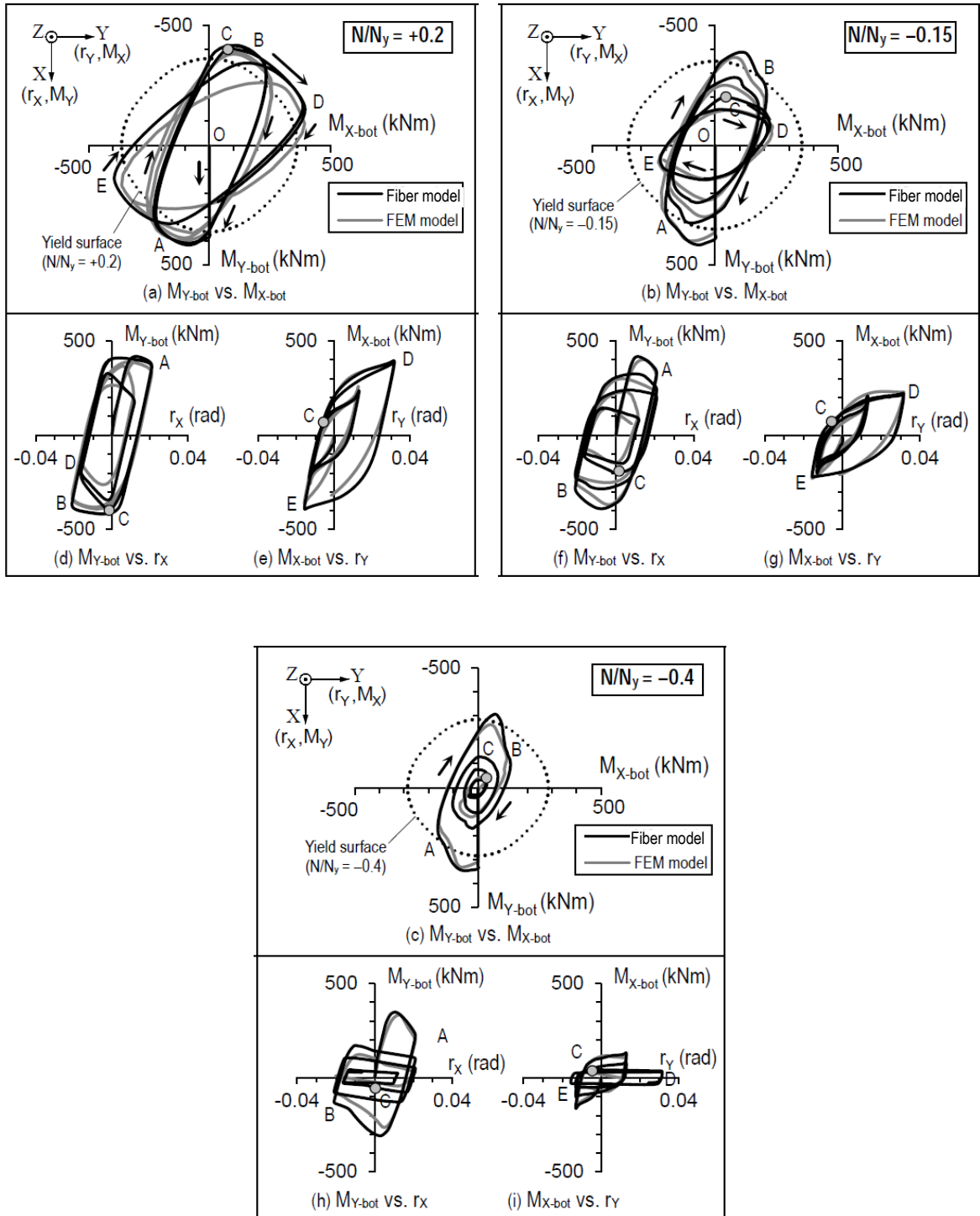
Figure 4.11 Analysis results of column bottom moments for loading type 2 (amplitude ±0.02 rad for r_X and –0.015 to +0.03 rad for r_Y directions).

The situation completely changes when the column is subjected to compression force. Under moderate compression level ($-0.15N_y$), $M_{\text{Y-bot}}$ easily deteriorates due to local buckling at the r_X deformation amplitude of ±0.02 rad [points A and B, Figure 4.11(f)], and the remaining capacity of $M_{\text{Y-bot}}$ at point C before changing to the other cycle is only 0.49 times its peak value achieved in previous cycles.

Although the peak r_Y amplitude (point D) is +0.03 rad, 1.5 times the peak r_X amplitude, the peak $M_{\text{X-bot}}$ at point D [Figure 4.11(g)] is only 0.50 times the peak $M_{\text{Y-bot}}$, almost equal to the remaining $M_{\text{Y-bot}}$ capacity at point C as mentioned above. The yield surface significantly shrinks down as shown in Figure 4.11(b). Similar situation with more severe shrinkage of yield surface occurs to the column model having large compression ($-0.4N_y$) [Figure 4.11(c)], where the peak $M_{\text{X-bot}}$ at point D [Figure 4.11(i)] as well as the remaining $M_{\text{Y-bot}}$ capacity at point C [Figure 4.11(h)] are only 0.12 times the peak $M_{\text{Y-bot}}$.

Generally, such complex biaxial moment interaction and deterioration under constant axial load were well simulated by the *Fiber model*. Moreover, the agreement with the results by *FEM models* can enhance the validation of fiber hinge element method. This loading *type 2* aims to predict the potential decreased capacity of $M_{\text{X-bot}}$ due to the preceding degraded $M_{\text{Y-bot}}$ after two cycles of r_X loading in large amplitude, thereby reducing the column resistance when the loading suddenly causes the shaking action in the r_Y direction, resulting in the column damage and structural collapse toward this direction.

4.3.3 Shrinkage of yield surface due to local buckling of column

The analytical results from the above loading schemes suggest the decreased capacity of $M_{\text{X-bot}}$ due to the preceding degraded $M_{\text{Y-bot}}$. To extend the study, this section briefly presents the proposed explanation for that finding, using the analytical results by *Fiber model*. The column model subjected to constant moderate compression force ($-0.15N_y$) and the loading *type 1-b* is selected to demonstrate.
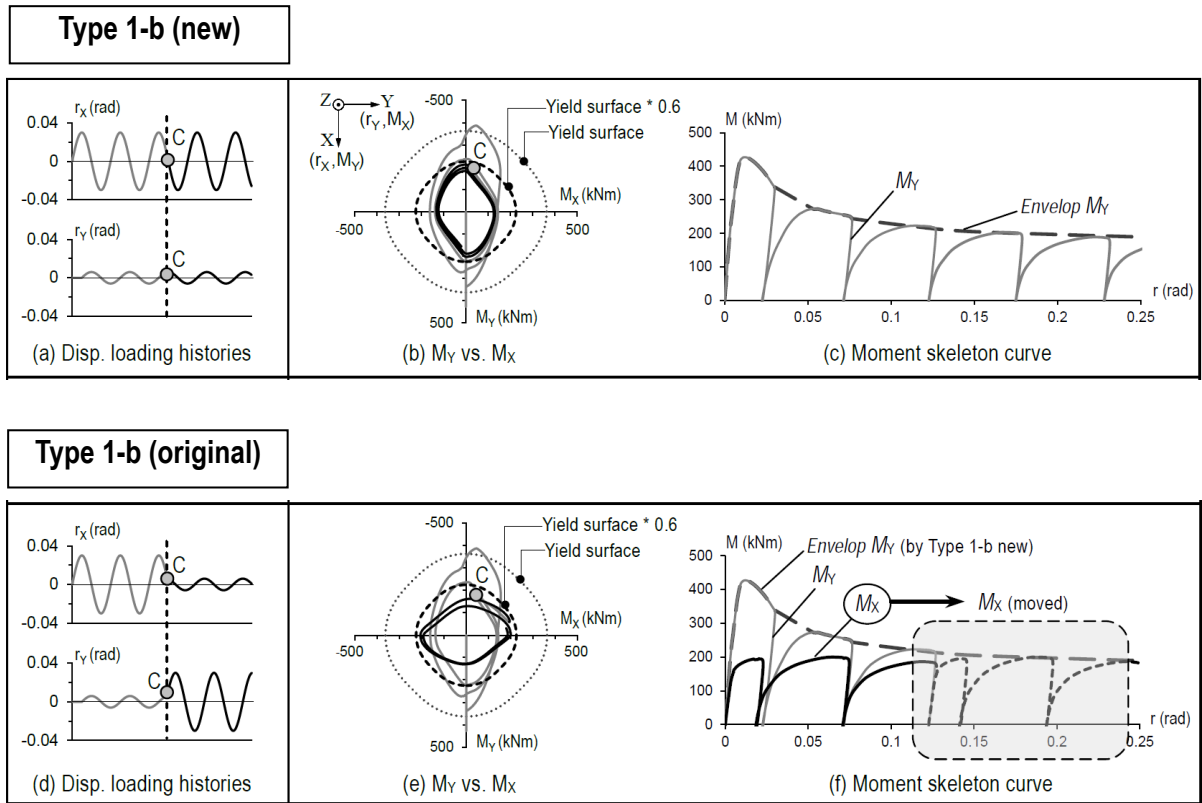
Figure 4.12 Shrinkage of yield surface caused by deterioration due to local buckling, examined by two loading schemes applied to Fiber model.

Firstly, by assuming the elliptical loops remain stable in the pure r_X direction throughout the loading without changing to the other direction at point C, the loading *type 1-b (new)* is proposed as shown in Figure 4.12(a). As a result, the column model experiences the continuous cyclic development of $M_{Y\text{-bot}}$ (hereafter abbreviated as M_Y) until the end of loading. The consequent moment interaction surface is shown in Figure 4.12(b), where the gray and black solid lines indicate the loading time before and after point C, respectively. The analytical yield surface shrinks down significantly to the almost stable one as large as 0.6 times the original one. The skeleton curve of M_Y is plotted in Figure 4.12(c) with the envelop curve shown by broken line.

By comparing with the original loading *type 1-b* as shown in Figure 4.12(d), the difference of moment interaction surface is displayed only after point C [*i.e.* the black line, Figure 4.12(e)]. However, the analytical results indicate quite similar shrinking levels of yield surface between two cases, even

though the displacement loadings are currently applied in two different directions. On the other hand, the skeleton curves of M_Y and M_X for the original loading *type 1-b* are plotted by *gray* and *black* solid lines, respectively in Figure 4.12(f). If the M_X skeleton (*black solid*) is moved adjacent to the end point of the M_Y skeleton, as represented by the *black dashed line* in the box shown in Figure 4.12(f), it locates within the margin limited by the envelop M_Y skeleton obtained by the loading *type 1-b (new)*. This finding suggests the nearly synchronized deterioration of moment capacity of the steel box column section in any principal direction. In other words, whenever the column moment deterioration occurs in one direction, the yield surface may shrink down, thereby limiting the moment capacity in the other directions.

4.4 Simulations of isolated columns in the collapse test

The previous section presented the bending analyses of the cantilever column under constant axial load. In fact, the structure during the seismic excitation experiences a more sophisticated axial load condition than the constant load assumption. Thus, the component test using constant axial load can hardly predict the actual deteriorating moment response as observed in the collapse test. This section presents a series of hypothetical time-history bending analyses conducted for all six columns (A1, A2, A3, B1, B2 and B3) in the first story level of the building. Assuming the inflection point remains stable at the middle height of the column, the analytical column models are constructed as cantilever columns with the height of $H/2 = 1750$ mm, where H is the actual first-story column height in the test frame. Displacement control is applied to the cantilever column model [Figure 4.13(a)], wherein the tip end is subjected to the bi-directional lateral displacement history so as to reproduce the identical chord rotation as the first-story drift ratio recorded in the collapse test at 100% Takatori motion level [Figure 4.13(b)]. In addition, the experimental varying axial force histories (including gravity load) of each particular column recorded in the collapse test [Figures 4.13(c)–(e)] are also applied to the column model.
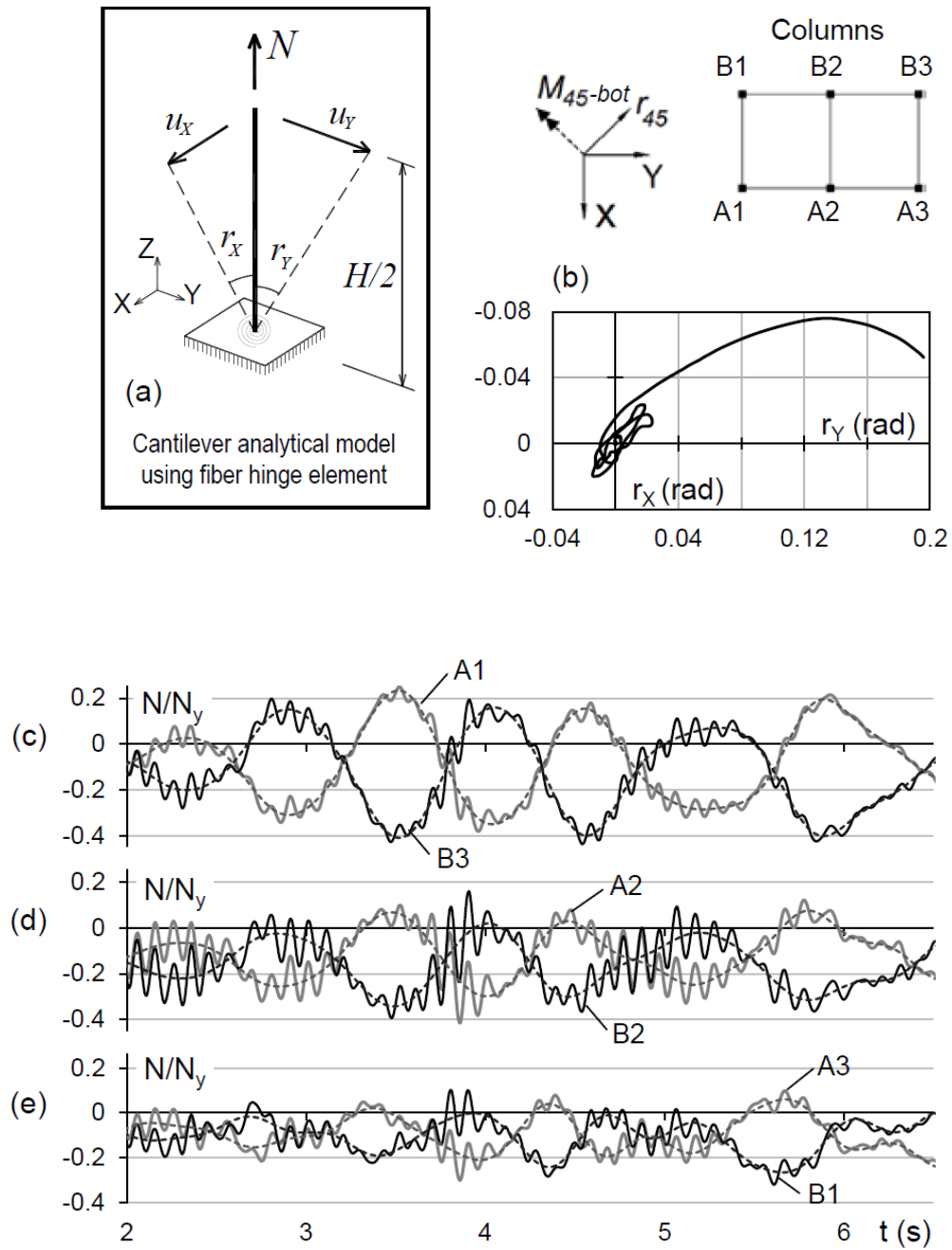
Figure 4.13 Cantilever column analyses using fiber hinge element with varying axial loads: (a) model and loading description; (b) deformation condition resembling first-story drift ratio recorded in the collapse experiment at 100% Takatori motion level; and different axial load conditions of six columns (c) A1 & B3, (d) A2 & B3, and (e) A3 & B1, shown in original time-histories *(solid line)* and low-pass filtered versions *(dashed line)*.

Variation of the axial forces was caused by the building overturning moment during the excitation. Therefore, each column shows different axial force histories. On the other hand, due to the major direction of story drift oriented diagonally [Figure 4.13(a)], the similar variation of seismic axial forces excluding the gravity load can be recognized in couples of columns located oppositely on that major diagonal direction: A1 and B3 [Figure 8(c)], A2 and B2 [Figure 4.13(d)], A3 and B1 [Figure 4.13(e)].

Note that the column axial force fluctuated as a result of not only the overturning moment but also the vertical response acceleration with a period of about 0.01 sec, which is equal to the building's natural period in the Z direction. In order to show the major variation of column axial forces excluding such high frequency fluctuation, low-pass filtered versions of the axial force histories (dashed lines) are also included in those figures.

In the sequence of Figures 4.13(c)–(e), the alternating fluctuations of low-pass filtered column axial forces were observed for each half cycle during the building vibration history, with peak values varying enormously from $-0.40N_y$ to $+0.22N_y$ for columns A1 and B3 [Figure 4.13(c)], moderately from $-0.34N_y$ to $+0.07N_y$ for columns A2 and B2 [Figure 4.13(d)], and slightly from $-0.27N_y$ to $+0.05N_y$ for columns A3 and B1 [Figure 4.13(e)].

In order to investigate the potential effect of the high frequency fluctuation of axial load on the column moment response, a preliminary analysis is conducted for one selected column A2 located in the middle and therefore develops the largest axial load fluctuation of nearly $\pm 0.15N_y$ due to the vertical response acceleration. Original and low-pass filtered experimental axial loading histories are analyzed.

Figure 4.14(a) shows the similarity of moment–rotation hysteretic relationship between two versions of axial loads. Only some slight local discrepancies showing the high-frequency fluctuation are reflected at the peak range of moment histories as shown in Figure 4.14(b).
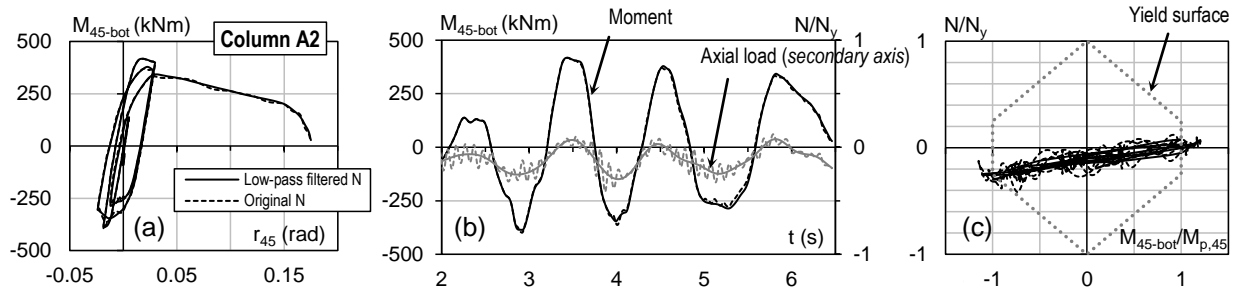
Figure 4.14 Comparison of fiber-based cantilever column's analytical results between two types of low-pass filtered (solid line) and original (dashed line) axial load conditions for the selected column A2 at 100% Takatori motion level: (a) bottom moment–deformation hysteretic curves, (b) bottom moment and axial load time-histories, (c) bottom moment–axial load interaction curves.

It is because the fluctuation of $\pm0.15N_y$ is not large enough to cause significant change of moment capacity for column A2 carrying gravity load of about $-0.15N_y$, as displayed by the moment–axial force relation in Figure 4.14(c). Therefore, the fluctuated column axial loads recorded in the collapse experiment due to the vertical acceleration might not have caused any significant influence to the column strength.

On the other hand, before the building collapsed under 100% Takatori motion level, it experienced significant yielding at 60% Takatori level test. In order to examine the effect of the preceding 60% Takatori motion to the final collapse test on the steel columns in the building, two types of single 100% Takatori loading history (noted as "*single loading*") and consecutive 60–100% Takatori loading history (noted as "*consecutive loading*") are applied to the analytical cantilever column models. Note that ten seconds of white noise delay are inserted between the 60% and 100% input motion histories.

Analytical results of three columns B3, A1 and A2 which develop the largest compression, largest tension and moderate axial load during collapse are selected to show in Figures 4.15(a)–(c), respectively. The results by single loading are represented by the gray thick lines, whereas the ones by consecutive loading are shown by the black thin lines (dotted and solid for the 60% and 100% Takatori parts, respectively).
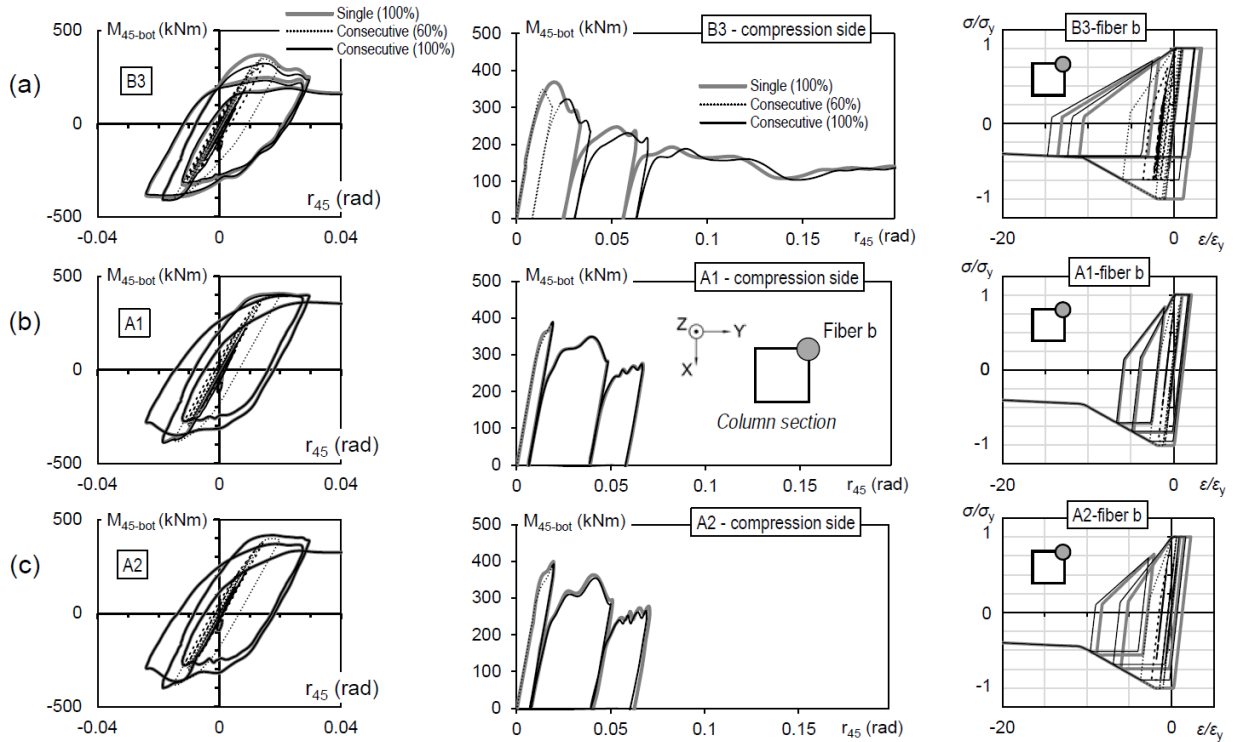
Figure 4.15 Comparison of cantilever column analytical results between two types of consecutive 60-100% Takatori loading (thin line: 60% Takatori part – dotted, 100% Takatori part – solid) and single 100% Takatori loading (thick line), for three columns B3, A1 and A2: moment-rotation hysteresis (left), skeleton curves for the compression side of columns showing moment deterioration (middle) and stress-strain of the selected critical compressive fiber (right).

In overall, the results of both loading types do not differ significantly except for column B3 on the positive side of deformation when it was subjected to compression load [Figure 4.15(a)]. It is because the analytical column B3 in case of consecutive loading had experienced the initial deterioration in the largest cycle of 60% Takatori motion level, its strength was reduced when the 100% Takatori motion consecutively excited the column model. This can be explained by the stress-strain relation of the fiber "b" located at the corner and subjected to the largest tensile effect by coupled biaxial bending and compression load [Figure 4.15(a) right]. However, the difference is shown mostly in the first cycle of 100% Takatori level. The moment histories and magnitudes of column B3 in the subsequent cycles until collapse appear to be quite similar in both cases, as can be recognized by the skeleton curves [Figure

4.15(a) middle]. Column A1 almost shows identical column moment and fiber strain results between the two cases [Figure 4.15(b)]. Column A2 displays a slight difference of fiber strain response and the skeleton curves on the compression side [Figure 4.15(c)]. In summary, the major inelasticity by 60% Takatori motion level was not large enough to cause considerable damage to every column in the structure. Both single and consecutive loading protocols can provide reliable results for these cantilever column analyses.

The above analyses suggest the effect of axial load history on the seismic response of column moment. The situation can be verified by the full set of time-history analyses for the entire six columns using fiber hinge element as shown in Figure 4.16 (right), where the experimental records and analytical results are represented by gray thick and black thin lines, respectively. The single 100% Takatori loading protocol is adopted. $M_{45\text{-bot}}$ of the cantilever column models agree with those recorded in the test, verifying the column strength deterioration due to the moment-axial force interaction and local buckling after several cyclic plastic deformations in large amplitude.

In addition, the contrast situations of moment deterioration are easily recognized in couples of columns: A1 and B3 (N/N_y varied from –0.4 to +0.2), A2 and B3 (N/N_y = –0.3 to +0.1), A3 and B1 (N/N_y = –0.2 to +0.0) as plotted in Figures 4.16(a)–(c), respectively. For instance, moment of column A1 mostly deteriorated on the negative side of deformation, whereas moment of column B3 primarily degraded on the positive side. The moment deterioration varied between columns, which is closely related to the seismic compression force that developed in the columns, as indicated earlier in Figure 4.13. Column A1 deteriorated when it was subjected to compression (peak N/N_y = –0.38), whereas column B3 still remained strength because it was under tension, and vice versa [Figure 4.16(a)]. On the other hand, it is noteworthy that after several load cycles, column moment magnitude on each side could not exceed the previously deteriorated magnitude on that side in preceding cycles anymore. This confirms the occurrence of column damage by local buckling before the collapse time, as will be detailed in the next chapter.
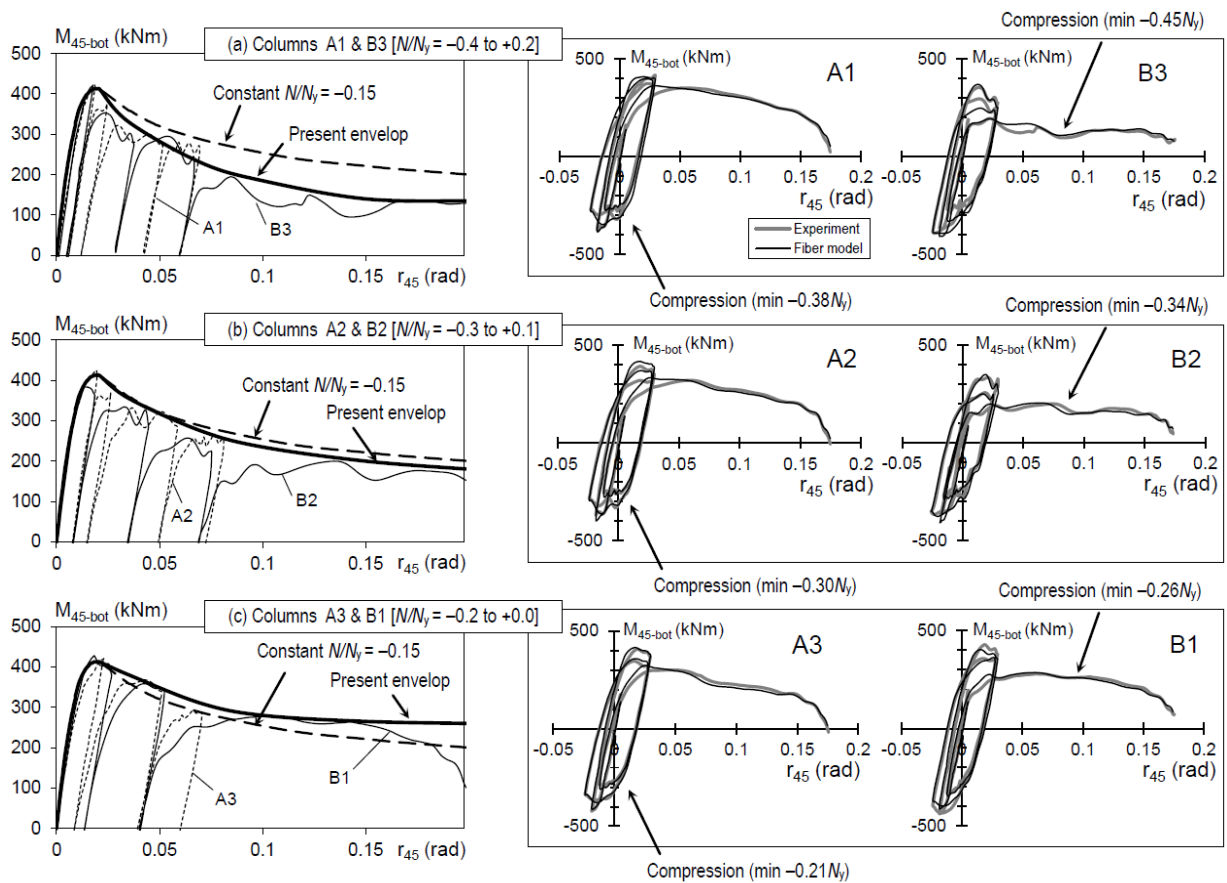
Figure 4.16 Experimental skeleton load–deformation curves showing effect of compression load on column moment deterioration (left), and comparison of hysteretic bottom moment–deformation curves (right) between collapse experimental records and fiber-based cantilever column's analytical results with different varying axial load conditions at 100% Takatori motion level, categorized into three groups of columns: (a) A1 & B3 [N/N$_y$ = –0.4 to +0.2], (b) A2 & B3 [N/N$_y$ = –0.3 to +0.1], and (c) A3 & B1 [N/N$_y$ = –0.2 to +0.0].

Each couple of columns shows different degrading shape of the moment hysteretic curves. The different varying axial load conditions developed in columns are the reason for the difference of moment degradation level, which can be interpreted by the moment skeleton curves recorded in the collapse experiment, combining the subsequent hysteretic segments on the compression sides of each column (Figure 4.16 left). The skeleton curve by component test with constant compression load N/N_y = –0.15 is also included and utilized as a basis for comparison.
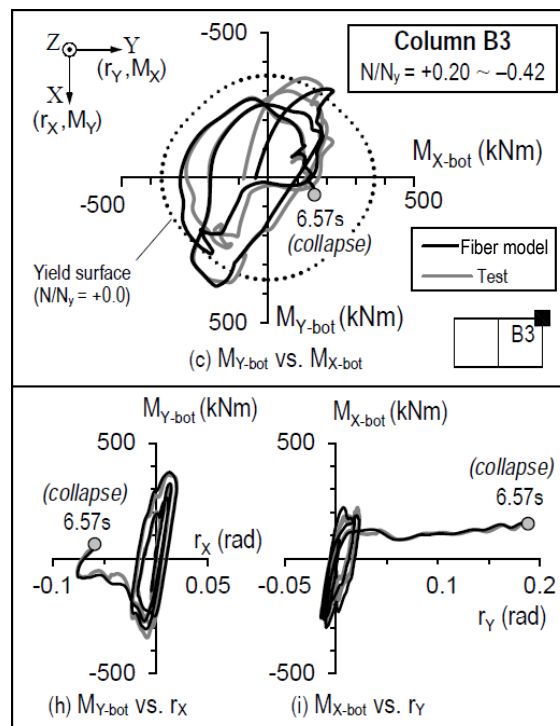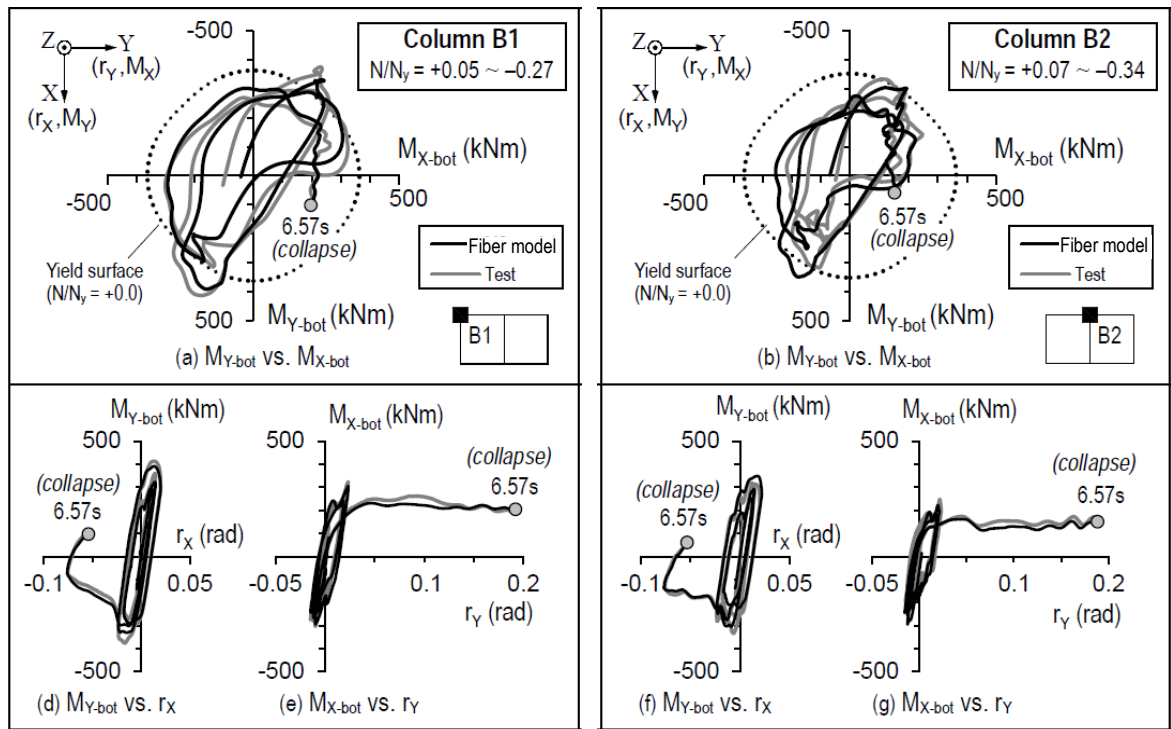
Figure 4.17 Analysis results of column bottom moments, applying varying axial force and lateral displacement histories by 100% Takatori level.

Moment responses of columns A2 and B2 appear to closely follow the basis skeleton because of the moderate variation of axial load. The envelop skeleton of columns A1 and B3 is more degraded, whereas the one of columns A3 and B1 is stronger than the basis skeleton. Larger compression forces resulted in more significant column deterioration.

Regarding moment response in each direction, three groups of graphs related to three selected columns with different levels of axial force varying: B1 (N/N_y varied from +0.05 to –0.27, *small compression*), B2 ($N/N_y \approx$ +0.07 to –0.34, *moderate compression*) and B3 ($N/N_y \approx$ +0.20 to –0.42, *large compression*) are shown respectively from left to right in Figure 4.17. Within each group, the graph arrangements are similar to those presented in Figure 4.8 (Section 4.3.1). Furthermore, to clarify the moment interaction surface, the curves relating to the elastic loading time before 3.2 sec (*i.e.* the start of the first cycle (a), referred to Section 2.4) are omitted in Figures 4.17(a)–(c). The stop point marked by circle symbol is related to 6.57 sec, the time when the building completely collapsed and settled on the supporting safeguard system.

As predicted by the loading *type 2* (Section 3.3.2), during the first two cycles of loading close to the r_X direction, $M_{Y\text{-bot}}$ developed earlier than $M_{X\text{-bot}}$ and rapidly reached to yield surface. However, the difference of axial force variation caused different responses of $M_{Y\text{-bot}}$ among the three columns during this time. $M_{Y\text{-bot}}$ of column B1 which had the smallest compression force hence was quite stable on both $-r_X$ and $+r_X$ loading directions [Figure 4.17(d)]. In contrast, the $M_{Y\text{-bot}}$ capacity of columns B2 [Figure 4.17(f)] and B3 [Figure 4.17(h)] was reduced significantly, especially on the $-r_X$ side, where they were carrying quite large compression forces. Local buckling must have occurred considerably to those columns during this time, thereby limiting their moment capacity. Consequently, the development of $M_{X\text{-bot}}$ was limited, particularly in the last half cycle until collapse at nearly 0.2 rad of r_Y deformation. Three increasingly significant levels of $M_{X\text{-bot}}$ deterioration during that time (characterized by the decreasing ratio of the average remaining capacity to the nominal plastic moment M_p) are easily recognizable from columns B1 [Figure

4.17(e), ratio 0.67] to B2 [Figure 4.17(g), ratio 0.48] and B3 [Figure 4.17(i), ratio 0.31]. The moment interaction surface of column B1 [Figure 4.17(a)] appeared to be strongest among the three columns, whereas the ones of columns B2 [Figure 4.17(b)] and B3 [Figure 4.17(c)] were much more shrinking, especially near the collapse time.

4.5 Summary

This chapter explained the methodology of simulating two-directional column deteriorations by using fiber hinge element.

- Compared to the continuum finite element models, the fiber hinge models required an empirical calibration considering the cantilever column test results, the existing prediction rule for local buckling, and FEM verifications. However, they certainly are more convenient, since they are able to clarify the physics of accumulated column damage by characterizing the complex three-dimensional deformation of the local buckling behavior, based on the approximate uniaxial stress-strain hysteretic relation of each fiber. This was demonstrated by the analyses of cyclic bending cantilever column models considering different cyclic loading types under different constant axial loads, as well as nonlinear analyses of isolated particular cantilever columns applying displacement histories and varying axial forces which were derived from the frame shake table tests.

- The study clarified that any deterioration of column moment due to local buckling in the X direction, for instance, may limit the capacity of moment in the Y direction, and vice versa, which can be explained based on the shrinkage of moment yield surface.

- The complex interaction between varying axial force and two-directional moment deteriorations was closely simulated by the model using fiber hinge element, promising its applicability to dynamic structural collapse analysis, as will be presented in the following chapter.

CHAPTER 5

BUILDING ANALYSES INVOLVING TWO-DIRECTIONAL
COLUMN DETERIORATIONS

Chapter 5

BUILDING ANALYSES INVOLVING TWO-DIRECTIONAL COLUMN DETERIORATIONS

5.1 Modeling features

The building specimen is three-dimensionally modeled by the PC-ANSR analysis program [36]. Columns and beams of the building are modeled by the line elements. Fiber hinge elements are adopted to simulate the buckling zone at the column ends. Composite action of the steel beam and concrete slab is taken into account by employing stiffness factors varied from 2.11 to 2.76 depending on the beam section type, specified by the Architectural Institute of Japan [37]. The beam-to-column panel zones and the bolted column base connection are modeled as the bilinear rotational spring elements whose elastic rotational stiffnesses are specified based on their responses measured in the test.

Non-structural components added on three exterior frames of the building are simulated as partially-restrained truss elements. Their elastic stiffness at each story level is determined by subtracting the steel frame stiffness (calculated from the story shear as summation of column restoring forces measured by strain gauges) from the building stiffness (calculated from the inertial force-based story shear). These components contribute about 10 to 15% the lateral stiffness at each story. Based on the observed behavior of non-structural components in the collapse test [9], their hysteretic behaviors are proposed so as to start degrading at the story drift ratio of 0.015 rad and gradually reduce strength to zero at the story drift ratio of 0.10 rad.

Rayleigh damping is adopted for the analytical model, with 2% damping assigned to cover the first two fundamental modes in both translational directions, based on the results identified from the free vibration test before main excitation (*i.e.* first mode damping ratios of 2.1% and 2.3% for the X and Y directions, respectively [6]). The analytical fundamental periods are 0.795 sec and 0.765 sec, consistent with those identified from the free vibration test, which are 0.8 sec and 0.76 sec in the X and Y directions, respectively [6].

5.2 Model validation using pre-collapse excitations

Accuracy of the analytical building model is demonstrated via nonlinear dynamic analyses considering small to large excitations. Subjected to the motion of 20% Takatori record which is equivalent to the Japanese Level-1 design earthquake (i.e. peak ground velocity at 0.25 m/s), the building responded elastically. The analytical results show good agreement with those recorded in the experiment, as displayed in Figure 5.1. Story drift ratios of the first story level in the X and Y directions (namely r_X and r_Y) are plotted in Figures 5.1(a)–(b), respectively. The plan view motion of the first story expressed in terms of story drift ratios is also given in Figures 5.1(g). Total accelerations of the second floor in the X and Y directions (namely $\ddot{u}_{tot,X}$ and $\ddot{u}_{tot,Y}$) are shown in Figures 5.1(c)–(d), respectively. Figures 5.1(e)–(f) show the base shear calculated as the summation of first-story column restoring forces measured by strain gauges in the X and Y directions (namely ΣQ_X and ΣQ_Y), respectively. The hysteretic relations between base shear and the first-story drift ratio in the X and Y directions are also presented in Figures 5.1(h)–(i), respectively. In those plots, black thin and gray thick lines represent the analytical results and experimental records, respectively. Under the 60% Takatori motion level which is 1.5 times greater than the Japanese Level-2 design earthquake (i.e. peak ground velocity at 0.75 m/s), the building had inelastic behavior. Figure 5.2 shows the analytical results for this excitation level in the same arrangement as those of 20% Takatori presented above. In overall, the model can simulate closely both the elastic and inelastic responses.
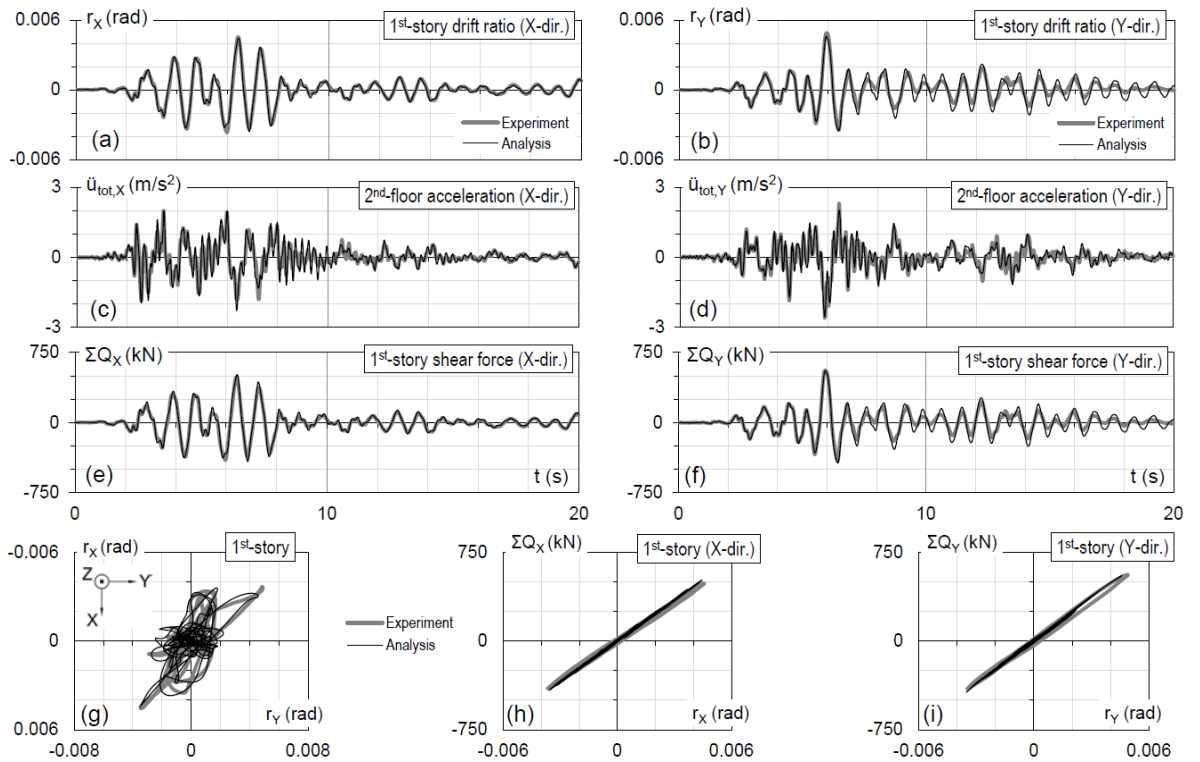
Figure 5.1 Comparison of the elastic global responses between analytical results (thin line) and experimental records (thick line) at 20% Takatori level: 1st-story drift ratios, 2nd-floor absolute accelerations, and 1st-story shear forces, in the X and Y directions.
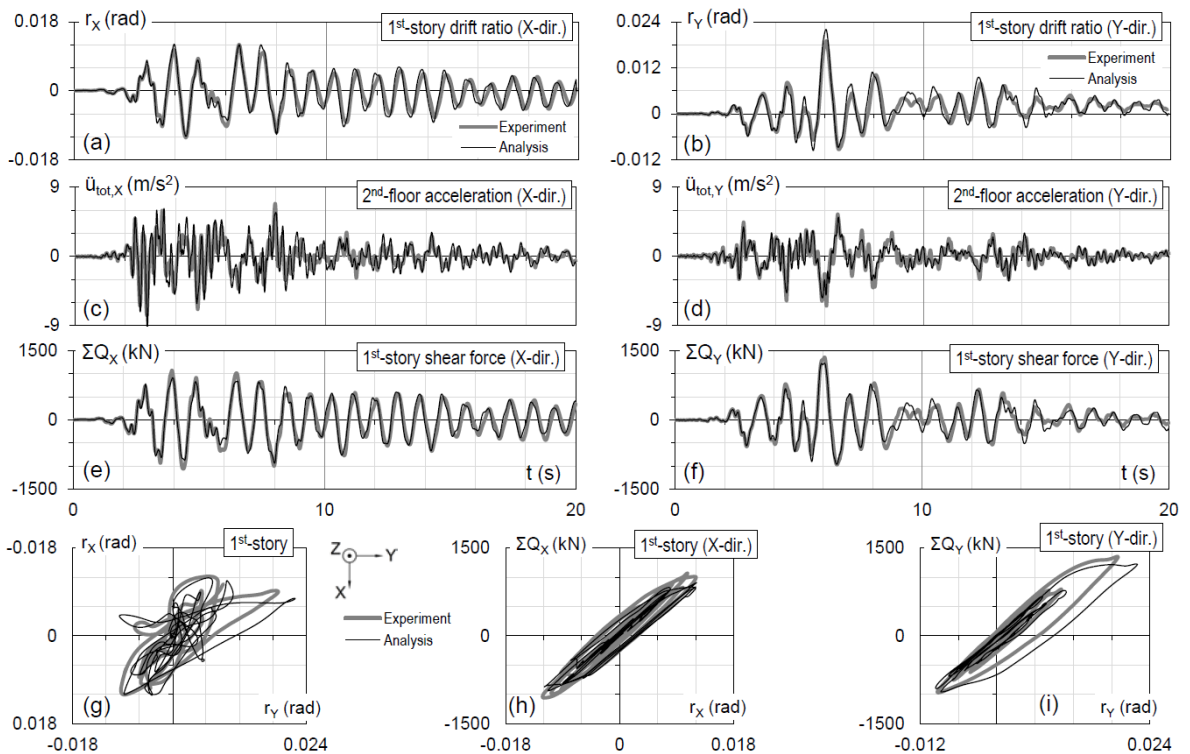
Figure 5.2 Comparison of the elastic global responses between analytical results (thin line) and experimental records (thick line) at 60% Takatori level: 1st-story drift ratios, 2nd-floor absolute accelerations, and 1st-story shear forces, in the X and Y directions.

(a) 1st-story drift ratio orbit
(100% Takatori level)

(b) Column axial loads at 5.9s
(peak building overturning moment)

(c) Selected fibers show different conditions under
biaxial bending and tension/compression load

(d) Enlarged orbit from (a)

(e) Timing definition of three main cycles based on 1st-story drift ratio time-histories

Figure 5.3 Analytical results (thin line) of the first-story drift ratios in comparison with the experimental records (thick line) at 100% Takatori level.

5.3 Simulations of column deteriorations

The collapse occurred when the building was subjected to the 100% Takatori motion level which is 2.5 times greater than Level-2 design earthquake (*i.e.* peak ground velocity at 1.28 m/s). Figure 5.3 displays the analytical results of displacement for the collapse excitation level, showing good agreement with those recorded in the test. Note that the model was subjected to the 60–100% Takatori consecutive input motions. The varying column axial force histories due to the building overturning moment as well as the high frequency fluctuation due to vertical acceleration were well simulated

by the analytical model. The schematic description of column axial forces at 5.9 sec (the time of peak building overturning moment) [Figure 5.3(b)] illustrates the trend of different tension and compression loads developed in columns whose relative magnitudes differ considerably by the column locations, causing different states of their moment deteriorations.

Two examples of oppositely varying axial force histories are shown in Figures 5.4(a)–(b) for columns A1 and B3 having the largest tension/ compression loads, respectively. Consequently, moment histories of those two columns deteriorated differently during the excitation loading until collapse, which can be explained based on the strain history of the selected fibers "*a*" and "*b*" [Figure 5.5(c)] located at corners showing completely different conditions under biaxial bending and tension/ compression load.
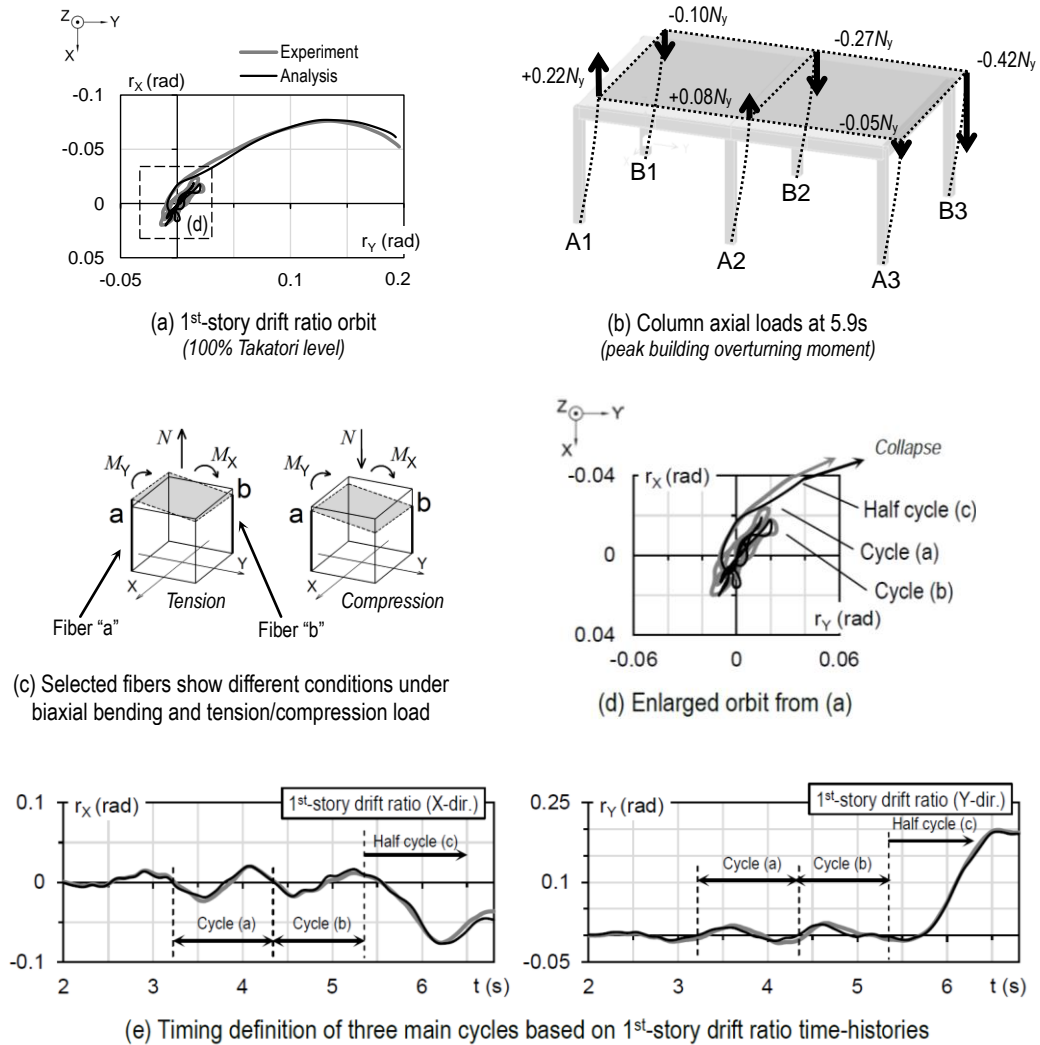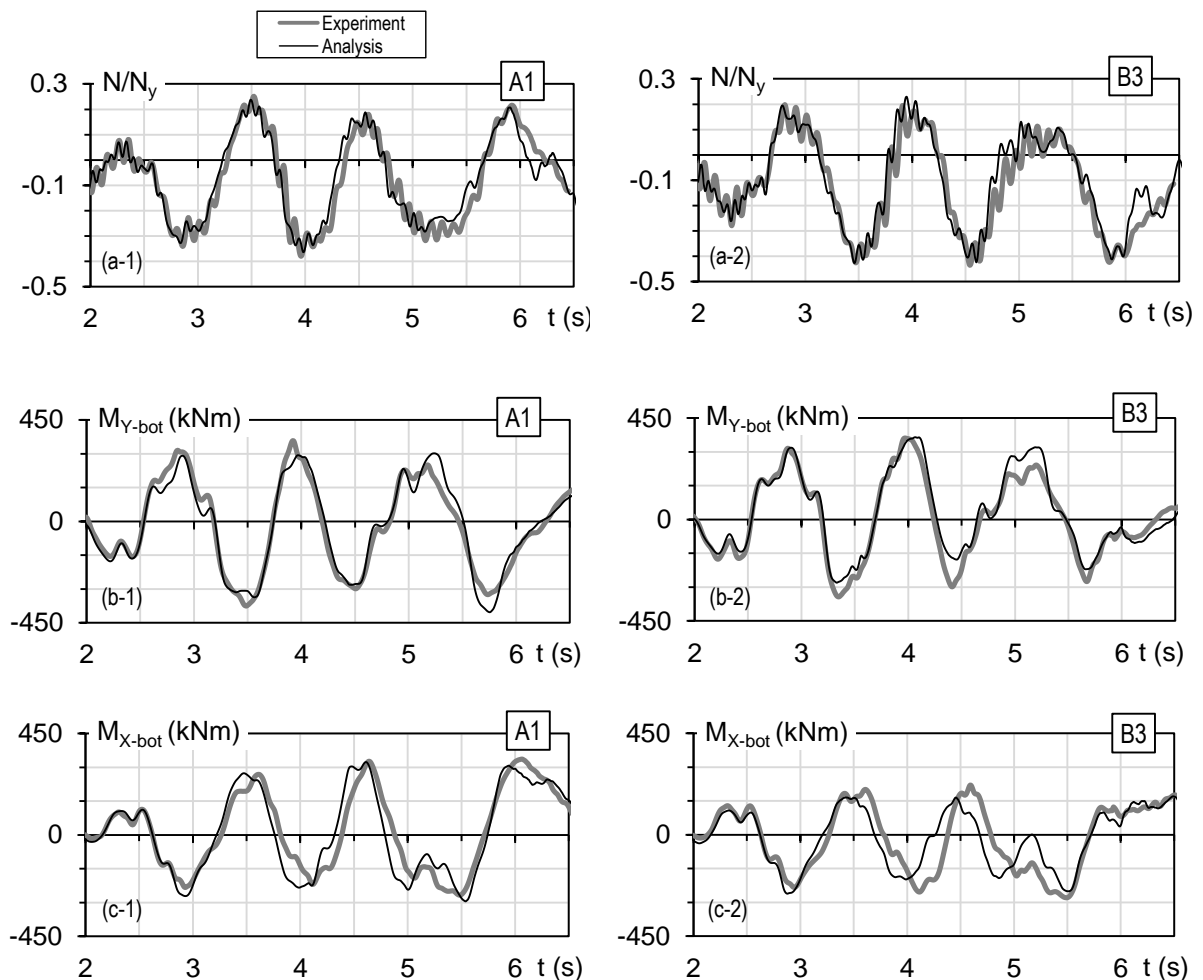

Figure 5.4 Comparison of the nonlinear local responses between analytical results (thin line) and experimental records (thick line) at 100% Takatori level: (a) axial load, (b) $M_{Y\text{-bot}}$ and (c) $M_{X\text{-bot}}$ of the first-story columns A1 and B3.
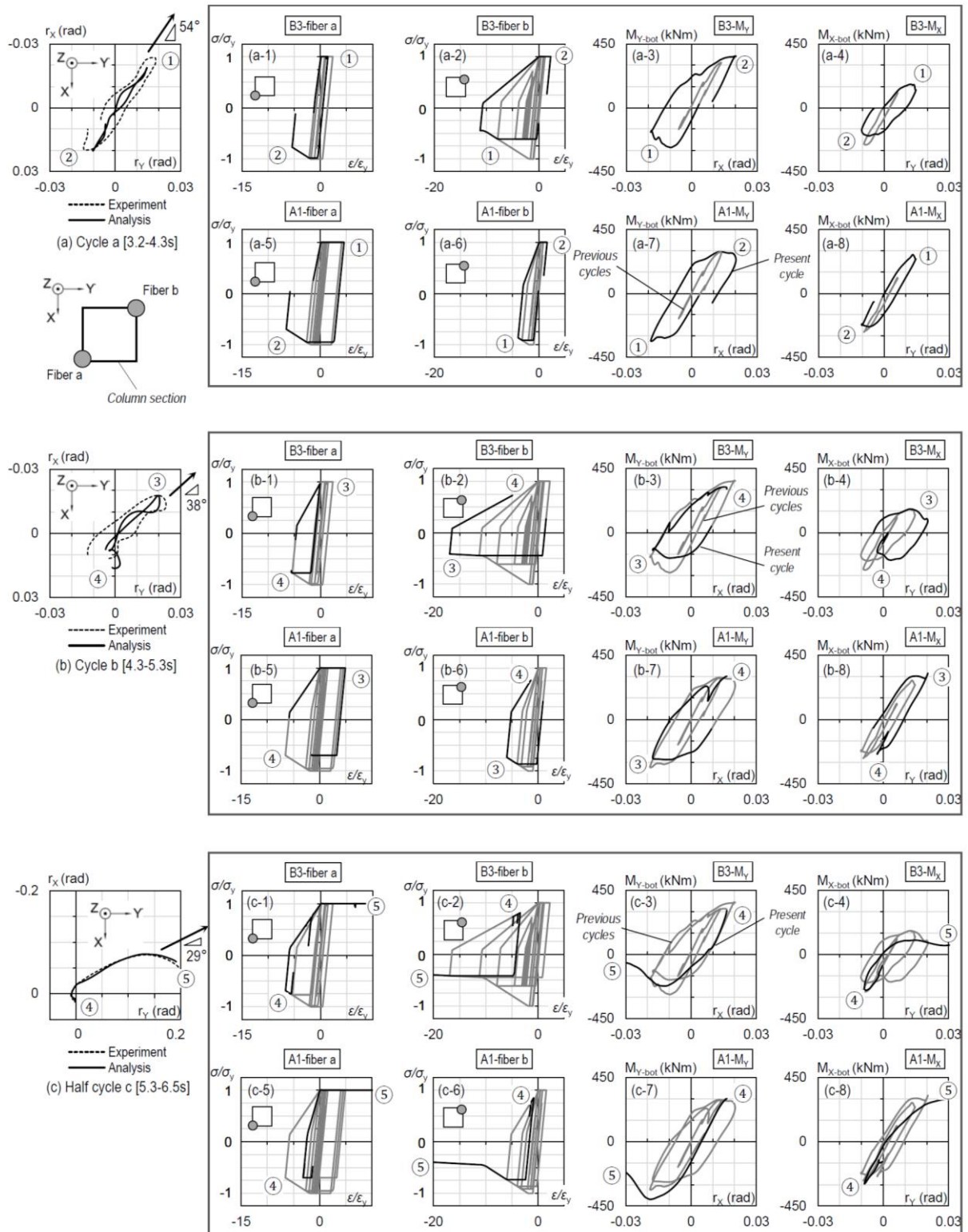
Figure 5.5 Analytical stress-strain responses of the selected fibers and consequent analytical bottom moments of two first-story columns B3 and A1 at 100% Takatori motion level, displayed in three main cycles: (a) 3.2 – 4.3s, (b) 4.3 – 5.3s, and (c) 5.3 – 6.5s, showing the different cumulative deteriorating progresses.

The physics of accumulated column damage characterized by fiber strain history can be clarified in each particular loading cycle. Based on Figure 5.3(e), three main cycles are specified with durations of (a) 3.2~4.3 sec, (b) 4.3~5.3 sec, and (c) 5.3~6.5 sec, respectively. Each cycle is defined as the period whereby the story drift orbit makes a full loop in plan. Figure 5.5 (left) shows the breakdown segments of the first-story drift orbit as three main cycles (a), (b), and (c), respectively. The arrow in the figure indicates the main orientation of each cycle defined here as the coordinate consisting of the maximum drift angle values of both r_X and r_Y.

In sequence of those cycles, the orientation angles shifted from approximately 54° [Figure 5.5(a)] to 38° [Figure 5.5(b)] and finally to 29° [Figure 5.5(c)] with respect to the +Y axis, respectively. The principal directions of the bending moments consequently were shifted cycle by cycle mostly from the X to the Y directions.

Accordingly, the column moment deterioration was initiated at the first peak displacement (noted as point ①) along the X direction in cycle (a) [Figure 5.5(a)]. Fiber "b" of column B3 experienced quite significant buckling [Figure 5.5(a-2)] whereas the one of column A1 was still strong [Figure 5.5 (a-6)]. Therefore, $M_{Y\text{-bot}}$ of column B3 degraded [Figure 5.5(a-3)] whereas $M_{Y\text{-bot}}$ of column A1 have not shown deterioration yet [Figure 5.5(a-7)]. In contrast, the weakening of column A1 only occurred at the subsequent peak displacement (noted as point ②) where fiber "a" of column A1 started to show buckling response [Figure 5.5(a-5)]. The influence of deteriorated strength in one side on the other side due to biaxial bending effect was reflected in $M_{X\text{-bot}}$ of both columns B3 and A1 [Figures 5.5(a-4) and (a-8)].

Similarly, such situation of column moment deterioration characterized by fiber strain history repeated in cycle (b) at two successive peak displacements [noted as ③ and ④ in Figure 5.5(b)]. Note that because of the reduced strength due to buckling from the previous cycle, the fiber's strain response under compressive stress became more critical. Fiber "b" of column

B3 at point ③ remained only half of its original strength [Figure 5.5(b-2)]. Consequently, $M_{Y\text{-bot}}$ of column B3 at point ③ degraded more significantly than the one at point ① of the preceding cycle [Figure 5.5(b-3)]. The accumulated strength deterioration was well simulated by the model.

Finally in the last half cycle (c) until collapse [Figure 5.5(c)], the building tended to yield toward the $+r_Y$ axis. The principal directions of the bending moments consequently were shifted mainly to the Y direction which also became the eventual collapse direction. The progress of story displacement from point ④ to point ⑤ caused the significant weakening of $M_{Y\text{-bot}}$ with a negative slope clearly shown in the hysteretic curve, meaning that the columns tended to be damaged in the r_X direction. In contrast, $M_{X\text{-bot}}$ continued increasing, but the tangent stiffness at the early stage was only approximately 1/3 of that in previous cycles, likely due to the change in cross section by the preceding decrease in $M_{Y\text{-bot}}$. From 5.9 sec until collapse, the deteriorations of $M_{Y\text{-bot}}$ and $M_{X\text{-bot}}$ were shown for column B3 where its capacities after deterioration [Figures 5.6(c-3) and (c-4)] were reduced to only half of those attained by column A1 [Figures 5.6(c-7) and (c-8)]. Effect of critical compression load of column B3 during this half cycle [Figure 5.5(a-2)] causing the earlier damage in comparison with column A1 which was still under tension [Figure 5.5(a-1)] was reflected by the analysis.

In addition, the analytical model also closely simulated the damages of other columns not shown and discussed in these figures occurring subsequently in between the times of damage of column B3 and A1, depending on the tension/compression load conditions developed in those columns.

5.4 Simulations of soft-story mechanism and energy dissipation

Figure 5.7 presents the motion trajectories of the entire system including shake table and all stories during the time from 5.5 to 6.5 sec in the last half cycle (c). The broken line stands for the shake table motion. From inside to outside, the solid lines indicate absolute displacements of the first-, second-,

third-story and roof levels. The story-drift velocity can be estimated based on the 0.1-sec increments marked by circles on the displacement orbit. The sudden increase in deformation at the first story during this time was well simulated by the analytical model (represented by the *black thin lines* with floor symbols) in comparison with experimental records (*gray thick line without floor symbols*).
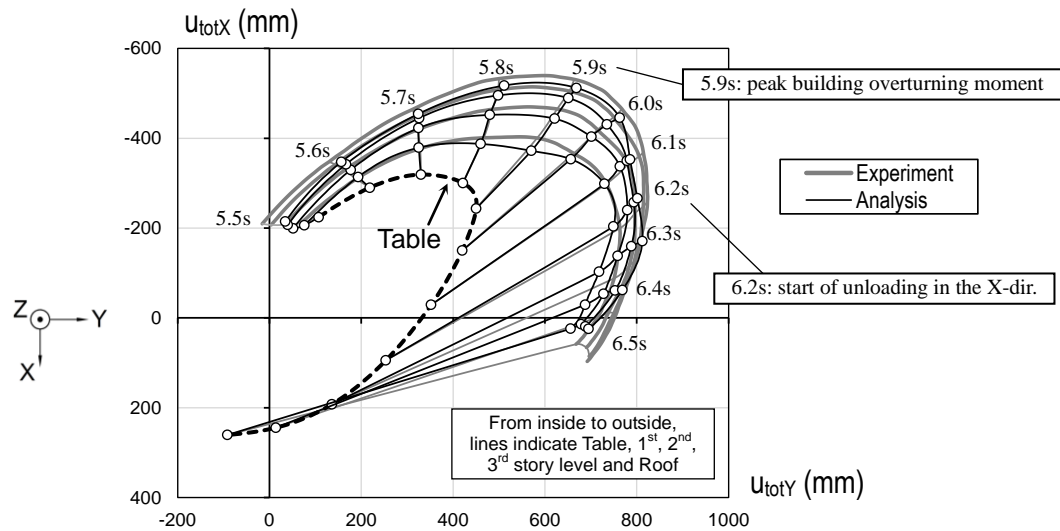
Figure 5.7 Plan view of absolute displacement of the building and shake-table at 100% Takatori level: analytical results (thin line), experimental records (thick line).

(a) X direction   (b) Y direction
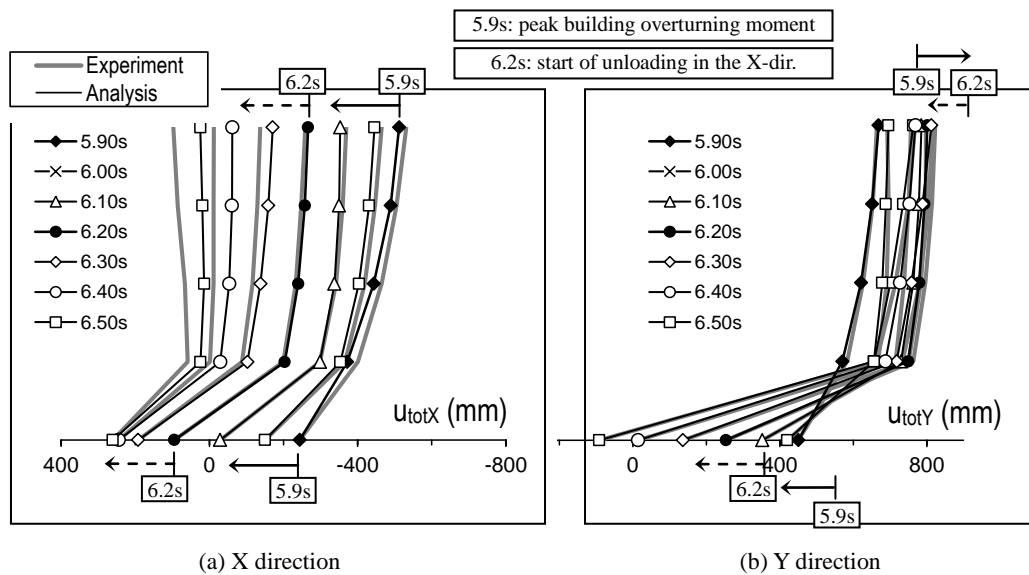
Figure 5.8 "Snapshots" at 0.1 sec increment of absolute displacement of the building and shake-table at 100% Takatori motion level in the (a) X and (b) Y directions: analytical results (thin line), experimental records (thick line).
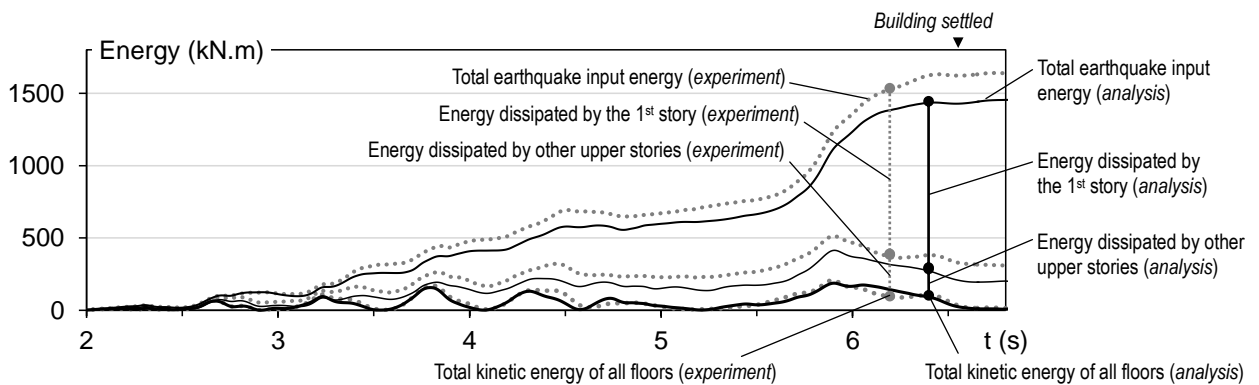
Figure 5.9 Comparison of the input and dissipated energies between analytical results (solid line) and experimental records (dotted line) at 100% Takatori motion level, of both X and Y directions.

Along the X direction [Figure 5.8(a)], the deformation magnitude appeared to increase nonlinearly at the first story from 5.9 sec. The response velocity of the first story was smaller than the input ground velocity, and the structure was shaken suddenly. Moreover, shaking action is more apparent in the Y direction [Figure 5.8(b)] from 5.9 to 6.2 sec, where the shake table already had reversed motion but the first story still kept moving forward, as indicated by the opposite arrows in the figure. The soft-story collapse mechanism induced by column deterioration was formally initiated at approximately 5.9 sec in the Y direction. Deformations then progressively concentrated in the first story because it experienced softening. Story-drift deformation increased unbounded in the first story but decreased in the other upper stories until the entire structure settled on the supporting table and collided with the safeguard system at 6.57 sec.

Soft-story collapse mechanism is also recognized via the energy dissipation. Figure 5.9 compares the experimental and analytical histories of the total input and distributed energies in the building at the collapse excitation level, with both the X and Y directions being summed. The uppermost line represents the *total earthquake input energy* which is the relative energy based on the relative velocity and displacement between the structure and the ground (or shake table). From top to bottom, the lines

indicate the *energy dissipated by the hysteretic and viscous forces* at the first stories and the other upper stories, and *total kinetic energy* of all floors. Note that the total input earthquake energy shown here is the relative energy based on the relative velocity and displacement between the structure and the ground (or shake table). The input energy simulated by the analytical model during the pre-collapse time appears to underestimate the experimental result, since the model simulated less dissipation of energy by the upper stories. However, the analytical model simulated quite well the dominant energy dissipation in the first story because of yielding activity in this story level. Especially, the rapidly increased input energy which was dissipated only by the first story from 5.7 sec until collapse was reproduced efficiently by the analysis.

5.5 Extension of hypothetical simulations

In order to examine the effect of the vertical input accelerations on the building dynamic responses, a hypothetical simulation was conducted on the analytical model by applying the 100% Takatori motion records excluding the vertical component. As shown in Figures 5.10 and 5.11, the simulation responses with and without vertical input accelerations are represented by solid and dashed lines, respectively, indicating only a minor difference between two cases. Except the high frequency fluctuation caused by the vertical input motion during the unbounded displacement zone near collapse time easily recognized in the base shear versus first-story drift ratio hysteretic relationship (Figure 5.10), the absence/presence of vertical input acceleration is predicted not to cause any major changes to the building's global horizontal responses. In local perspective, the responses of column B3 are selected to demonstrate the comparison (Figure 5.11). Due to the lack of vertical accelerations, the fluctuation of column axial force [Figure 5.11(a)] was filtered out. Only the effect of overturning moment was reflected on the column axial force response; however, the consequent uni-axial stress-strain relation and strength deterioration of column fiber [Figure 5.11(b)] did not change

significantly under the absence of high frequency fluctuation of axial force. As a result, the column bending moment responses and degradations due to local buckling [Figures 5.11(c)–(d)] did not differ considerably from the ones with vertical input motion.
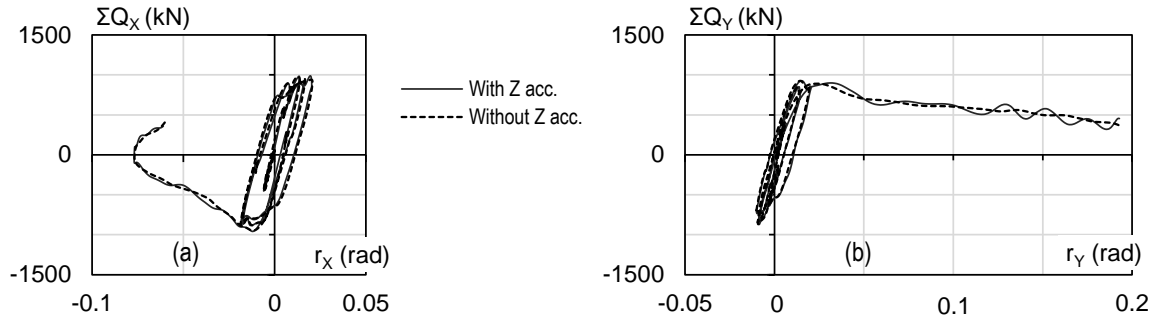
Figure 5.10 Comparison of the global analytical responses at 100% Takatori motion level between the loading with (solid line) and without (dashed line) vertical input accelerations: 1st-story shear forces versus story drift ratios in the (a) X, and (b) Y directions.
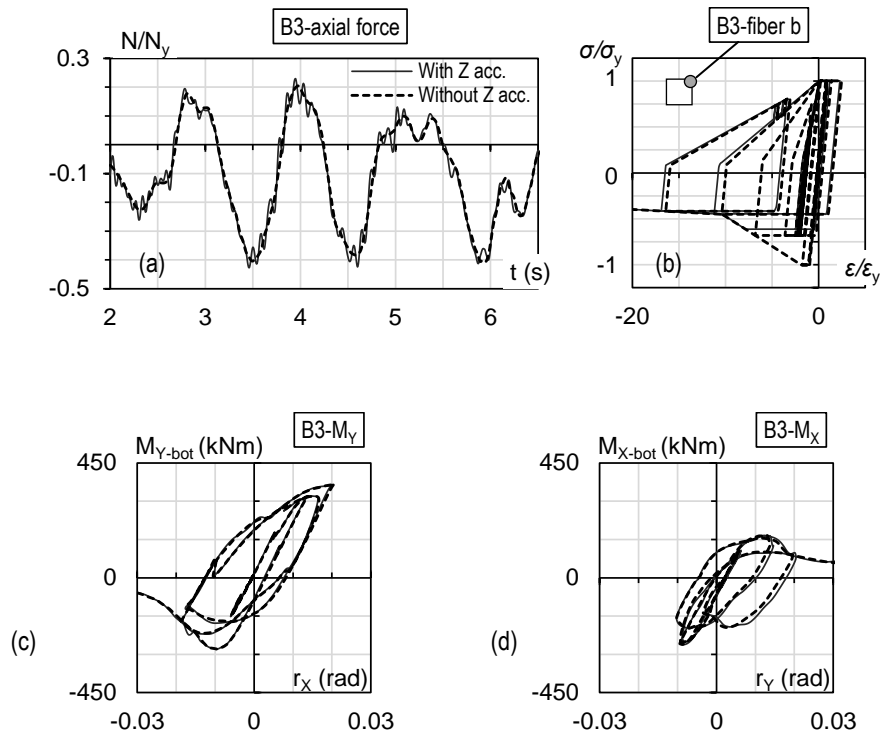
Figure 5.11 Comparison of the local analytical responses at 100% Takatori motion level between the loading with (solid line) and without (dashed line) vertical input accelerations: (a) axial force history, (b) typical fiber stress-strain relation, (c) bottom moment $M_{Y\text{-bot}}$ and (d) $M_{X\text{-bot}}$ of column B3.

(a) 1st-story drift ratio history [Y-dir.]   (b) 1st-story shear vs. drift ratio [Y-dir.]
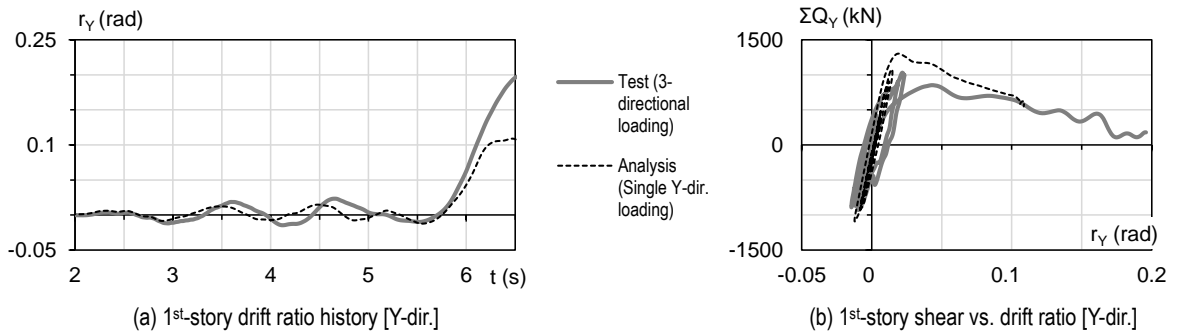
Figure 5.12 Comparison of the planar analytical responses applying the single Y direction input accelerations (dashed line) and test results involving three-dimensional input motions (gray solid line) at 100% Takatori level: 1st-story drift ratio (a) time-history and (b) hysteretic relation with story shear force in the Y direction.

On the other hand, the planar anlytical study was also conducted using the single input ground motion in the Y direction which developed the largest deformation and eventual collapse orientation. Under the lacking of the simultaneous ground shaking activity in the X direction, the experimental correlative two-directional column deteriorations were not reflected by the analytical responses represented by the gray solid and dashed lines, respectively (Figure 5.12). The first-story drift ratio r_Y simulated by the planar analysis was out-of-phase and the one at 6.5s reached to 0.11 rad, just nearly a half of the experimental record [Figure 5.12(a)]. Furthermore, the highly overestimated analytical base shear strength in the Y direction [Figure 5.12(b)] obviously shows the potential error of planar simulation approaches which are not able to involve the interaction of two-directional input ground motions as well as structural responses and deteriorations. Hence, a full constitutive 3D analytical model would be more appropriate for the nonlinear dynamic collapse simulation.

5.6 Summary

This chapter described the simulation of building responses throughout small to large and collapse excitation levels.

- Due to the effects of complex loading such as alternately applied compressive and tensile axial load induced by overturning moment, and shifting of the principal directions of the bending moment cycle-by-cycle, a 3D model proves its appropriateness and advantages rather than 2D approaches in simulating the building response in this collapse test.

- The nonlinear dynamic analyses using the fiber hinge models efficiently simulated the building responses throughout small to large excitations. The agreement with experimental records was achieved on variety of quantities such as story drift ratios, accelerations, base shear, and energy dissipation.

- The model was able to simulate the deteriorating behavior due to the coupled axial load and two-directional bending moment of particular columns whose relative magnitudes differ significantly by their locations. On the other hand, the accumulated deteriorations in accordance with the cycle-by-cycle shifting of the principal direction of the two-directional bending moments causing the earlier damage of column section in the X direction and subsequently reducing the resistant capacity in the Y direction were successfully reflected by the analytical model. The progress of column deteriorations was visualized and detailed via the stress-strain hysteretic relations of column-end fibers. The eventual soft-story collapse mechanism induced by the weakening of the first-story column ends was also closely simulated.

- The analytical model can predict the hypothetical responses of the building which were not tested or measured in the experiment, such as the presence/absence of vertical input accelerations is predicted not to cause any significant effect on the building collapse response, or the

correlative activity of two-directional input motions causes more damages to the structure than the single one.

- Moreover, the approach as adopted in this study combining simple beam, truss, spring and fiber hinge elements rather than finite elements indicated the extent to which the simplified analysis can simulate the structural instability.

CHAPTER 6

CHARACTERIZATIONS FOR CYCLIC DETERIORATIONS OF
COLUMNS AND SOFT STORY

Chapter 6

CHARACTERIZATIONS FOR CYCLIC DETERIORATIONS
OF COLUMNS AND SOFT STORY

This chapter characterizes the analytical column model using fiber hinge element in comparison with other analytical methods using the skeleton and Bauschinger approach (Yamada *et al.* [40], Ishida *et al.* [41–42]) for cyclic deteriorations and soft story. The characterization is on some aspects such as: (1) cyclic moment-deformation hysteresis shape, (2) two-directional correlative deteriorations caused by local buckling, (3) effect of varying axial load condition, and (4) soft story behavior governed by six columns.

6.1 Column moment-rotation hysteresis shape

On the basis of skeleton and Bauschinger curves, Yamada *et al.* [40] established a hysteresis model of tube columns under uniaxial bending, involving deterioration caused by local buckling. The database of cyclic test results on tube columns with varying *b/t* ratios and lengths was utilized for the establishment of skeleton curves. Due to the characteristic of skeleton approach, the study needed to assume the unloading part of the hysteresis curve. Therefore, the analytical moment-rotation hysteresis curves [Figure 6.1(a)] appeared to overestimate column strength during the loading reverse ranges, and the hysteresis shapes related with the large deformation ranges were relatively more expansive than the experimental ones.

(a) Yamada *et al.*'s skeleton and Bauschinger method [40]: *left*- hysteresis, *right*- skeleton

(b) Fiber hinge method: *left*- hysteresis, *right*- skeleton
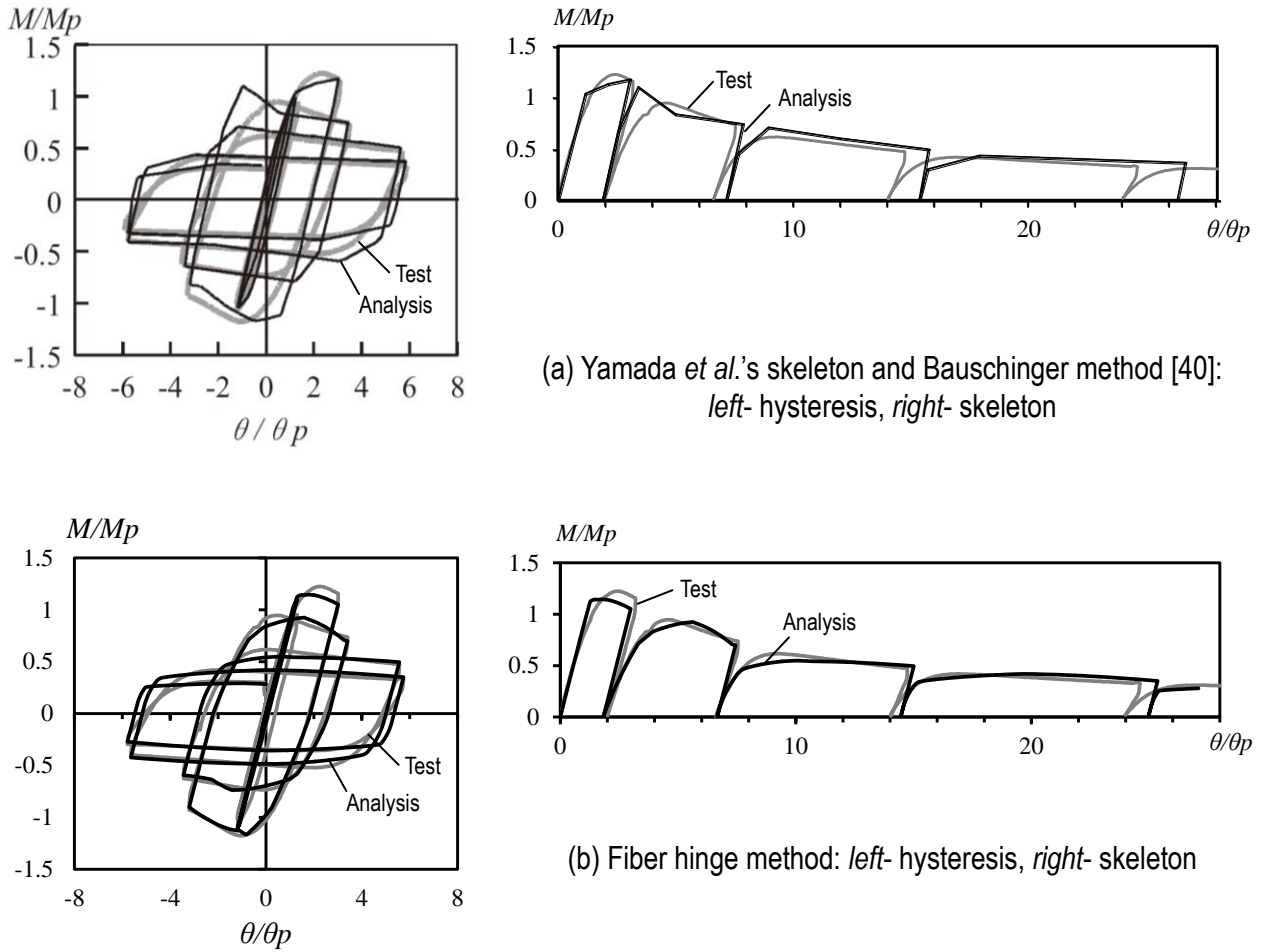
Figure 6.1 Analytical column moment-rotation hysteresis and skeleton curves for 0-degree loading case ($b/t = 33$, $N/N_y = -0.15$).
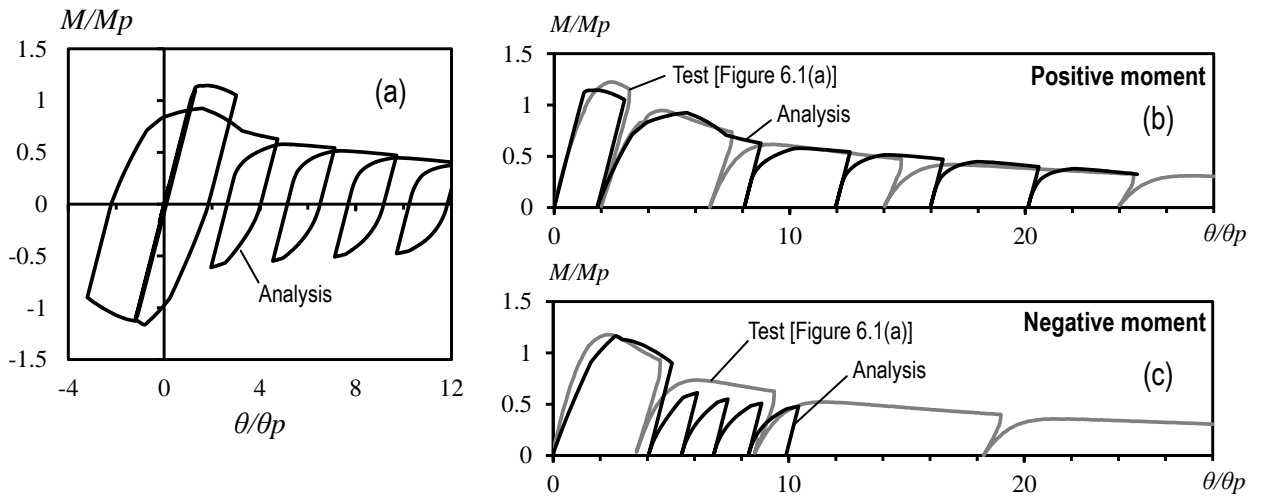
Figure 6.2 Analytical column moment-rotation results by fiber hinge method: *left*-hysteresis, *right*- skeleton curves ($b/t = 33$, $N/N_y = -0.15$).
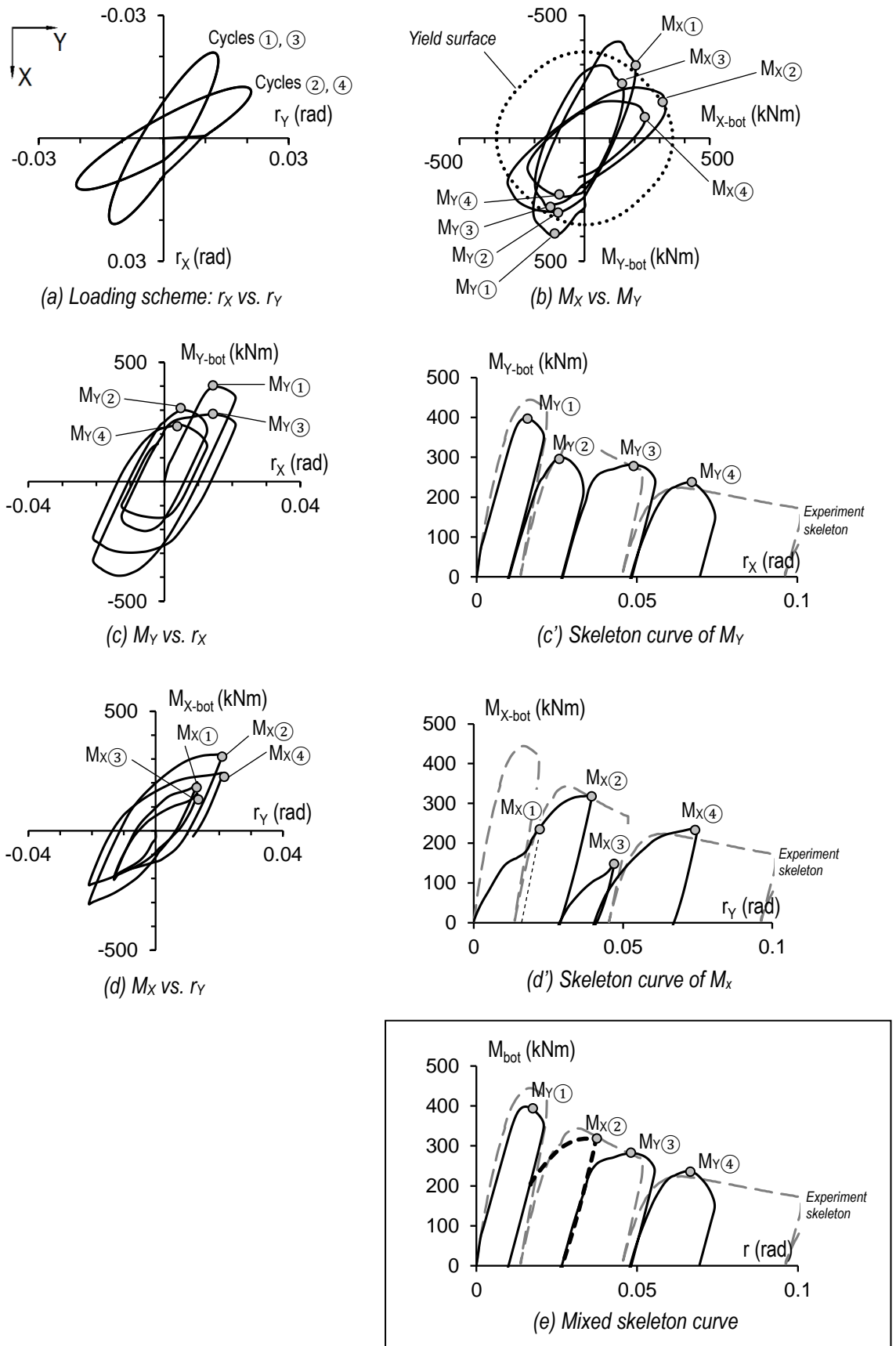
Although Yamada's skeleton curve [Figure 6.1(a)-right] closely matched the experimental one, some local overestimations of moment can be found, *e.g.* in the second cycle. It consequently caused the hysteresis shape slightly coarse. Figure 6.1(b) shows the analytical results by fiber hinge method for the same column type and loading condition with those by Yamada's method [Figure 6.1(a)]. Due to the fiber discretization of column section, the hysteresis curve by fiber hinge method fairly agrees with the experimental response, and the hysteresis shape appears smoother than Yamada's one.

A hypothetical loading scheme considering the asymmetric cyclic bending [Figure 6.2(a)] was additionally applied to the fiber hinge model. The skeleton curves by this new loading scheme are shown in Figures 6.2(b)–(c) for the positive and negative moments, respectively. The experimental skeleton curve previously plotted in Figure 6.1 is used for the comparison, showing good agreement of the fiber hinge model, except a slight difference on the negative moment skeleton [Figure 6.2(c)].

In summary, the fiber hinge element method as presented in this study specifies local properties of fibers but is able to control the global column moment-rotation hysteresis shape in good agreement with the experimental response. Although the method has different approach, it shows certain compatibility with the skeleton approach like Yamada *et al.* [40].

6.2 Two-directional correlative deteriorations

As discussed in previous chapters, the fiber hinge element method is capable of controlling two-directional correlative moment deteriorations. The weakening of fibers during the two-directional cyclic loading automatically reflects the shrinkage of column moment yield surface, thereby reducing the capacity whenever the deterioration of moment occurs in any direction. An analytical example of random two-directional cyclic loading is selected to show in Figure 6.3(a). The simulated moment interaction surface and hysteresis curves in the X and Y directions are shown in Figures 6.3(b)–(d), respectively.

(a) Loading scheme: r_X vs. r_Y

(b) M_X vs. M_Y

(c) M_Y vs. r_X

(c') Skeleton curve of M_Y

(d) M_X vs. r_Y

(d') Skeleton curve of M_x

(e) Mixed skeleton curve

Figure 6.3 Analytical results by fiber hinge method applying the random two-directional loading scheme ($b/t = 33$, $N/N_y = -0.15$)

The two individual skeleton curves of $M_{Y\text{-bot}}$ and $M_{X\text{-bot}}$ are plotted in Figures 6.3(c')–(d'), respectively. Those curves indicate four loading cycles ①, ②, ③, ④, and peak responses during each cycle, *e.g.* $M_{X②}$ means the peak M_X at cycle ②. Those graphs clearly show the peak points in each segment (*i.e.* half cycle) of the individual skeleton curves outrace the experimental envelop skeleton curve, thereby suggesting incompatibility of the uniaxial-bending skeleton approach for explaining the biaxial moment response. Therefore, a mixed skeleton curve including both M_Y and M_X should be considered to understand the two-directional correlative deteriorating sequence.

The general rule for creating a mixed two-directional moment skeleton curve is proposed as follows:

- From the two individual skeleton curves of M_X and M_Y given, select the one giving the largest moment and use it as the initial segment of the mixed skeleton curve.

- For the subsequent cycle after that segment, compare the peaks of M_X and M_Y, then select the skeleton segment (either M_X or M_Y) giving the larger moment and put it consecutively at the end point of the previous segment.

- Repeat the similar action for other subsequent cycles. Combine the selected segments to get the mixed two-directional skeleton curve.

Figure 6.3(e) shows the mixed two-directional moment skeleton curve by applying the above-mentioned rule. Initially, it includes the segment of $M_{X①}$ (solid line) because of the larger response in cycle ①. However, in cycle ②, the segment of $M_{Y②}$ (dashed line) is selected instead of $M_{X②}$. Then, in cycle ③, the segment of $M_{X③}$ (solid line) is selected because its magnitude was larger than $M_{Y③}$. Similar procedure is conducted until the end of loading. Finally, the mixed skeleton curve [Figure 6.3(e)] appears to closely follow the experimental envelop skeleton curve, in contrast with the two individual skeleton curves of $M_{Y\text{-bot}}$ and $M_{X\text{-bot}}$ [Figures 6.3(c')–(d')].

To analyze biaxial bending behavior of tube columns, Ishida *et al.* [41–42] used the multi-spring (MS) approach for modeling the column hinge. In that approach, a stress-strain hysteresis rule for the axial spring was developed. However, the study did not clearly present its own feature of controlling two-directional correlative deteriorations.

6.3 Effect of varying axial load condition

In order to involve the varying axial load condition in the MS model, Ishida *et al.* [42] specified the rule for controlling the spring's stress-strain response (based on Yamada *et al.* [43]) by switching between the skeleton curves at different axial force levels (Figure 6.4). However, as a matter of fact, the spring's axial stress-strain response which should implicitly reflect the effect of column axial force variation was not considered in that approach, in contrast with the feature of fiber hinge element method as presented in this study (Chapter 4).
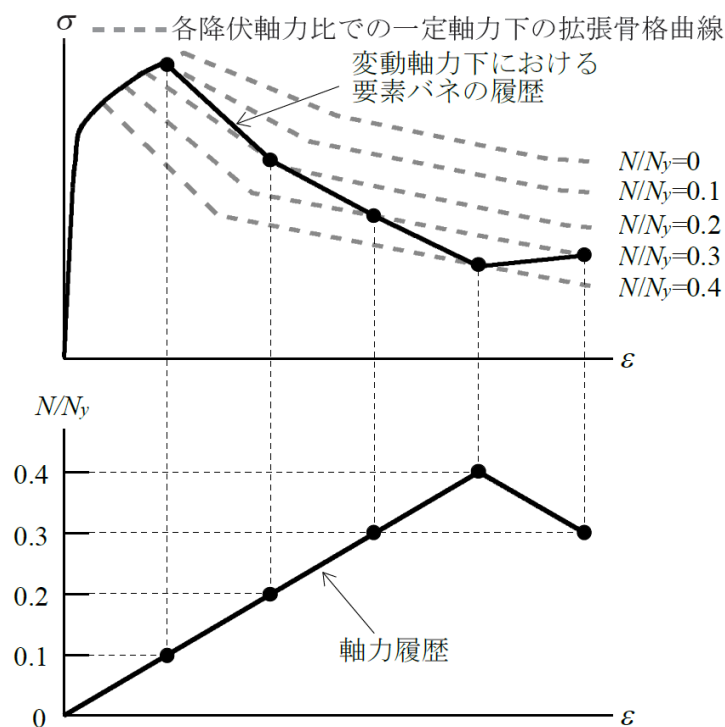
Figure 6.4 Analytical rule (based on Yamada *et al.* [43]) of controlling the spring's stress-strain response under varying axial force condition by switching between the skeleton curves at different axial force levels.
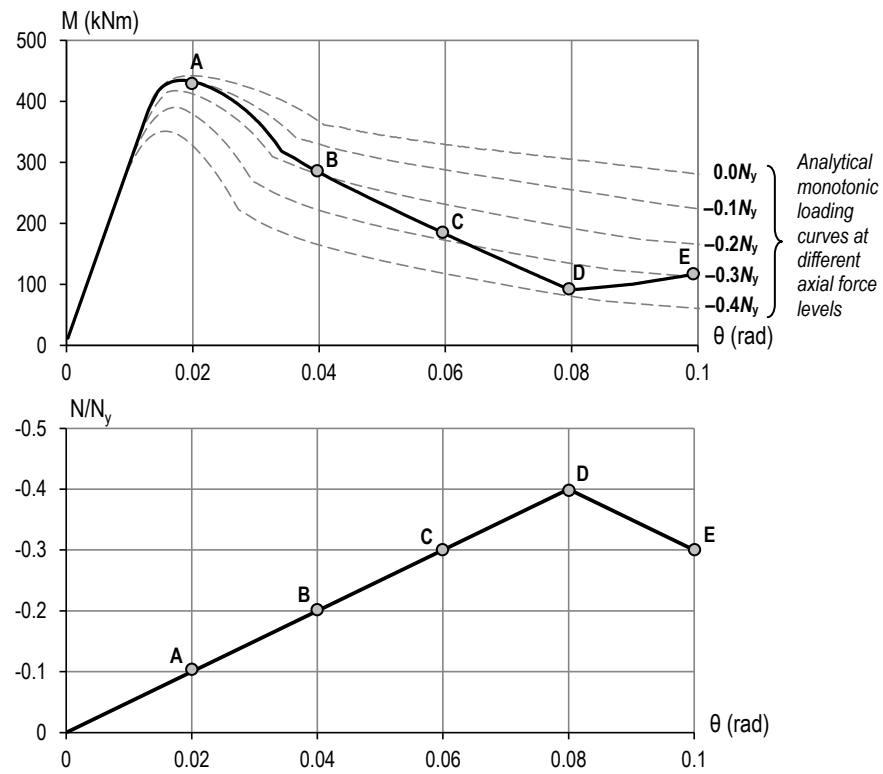
**Figure 6.5** Analytical monotonic bending moment response *(upper)* under varying axial force condition *(lower)* simulated by fiber hinge method.

A similar analytical monotonic loading scheme (as shown in Figure 6.4) simulated by fiber hinge model considering the changing of axial force in accordance with the displacement history is shown in Figure 6.5. A series of analytical monotonic moment-deformation curves at different levels of axial forces are included in the figure, showing the simulated moment responses associated with each point (A, B, C, D, E) quite agree with each corresponding individual axial force level. The simulation result indicates that the fiber stress-strain responses under the variation of axial force condition can automatically generate the column moment response in compatibility with the skeleton approach. More examples can confirm this feature, such as the simulation results for isolated columns considering the displacement and axial force histories derived from the collapse test (as presented earlier in Section 4.4). Three columns B1, B2 and B3 with different axial force conditions are selected to show the simulated moment skeleton curves in Figure 6.6.
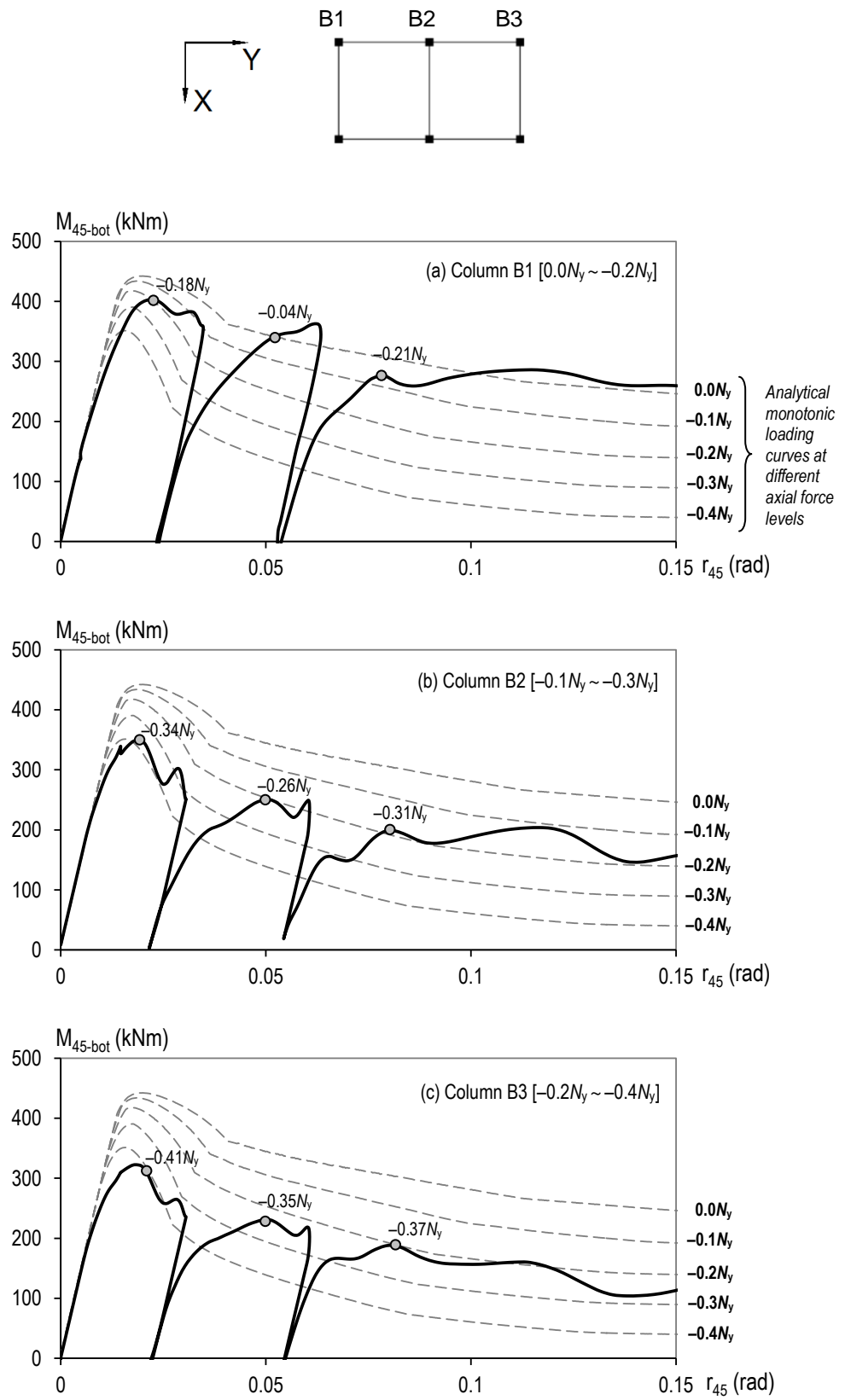
Figure 6.6 Analytical moment-rotation skeleton curves simulated by fiber hinge method, applying lateral displacement and varying axial force histories derived from the frame shaking test (columns B1, B2, B3).

6.4 Soft-story behavior governed by six columns

During the seismic loading, axial forces developed in columns may differ depending on the column location (Figure 6.7). However, the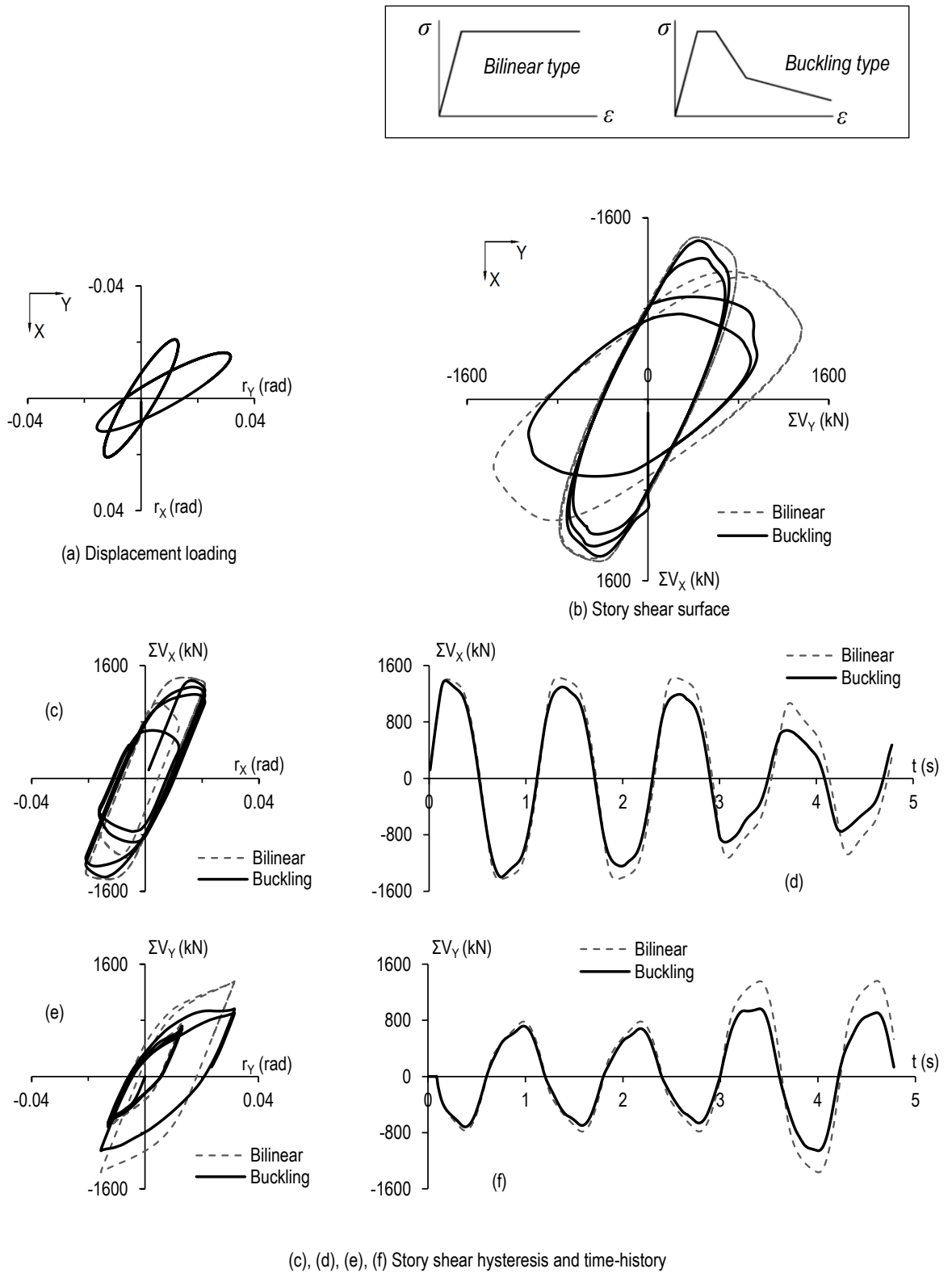 summation of column axial forces should remain constant as the building weight. On the average sense, the base shear response thus can be approximated from the analytical shear force of a single cantilever column model considering constant axial load as the building weight W divided by number of columns (*e.g.* $W/6$ for this building).
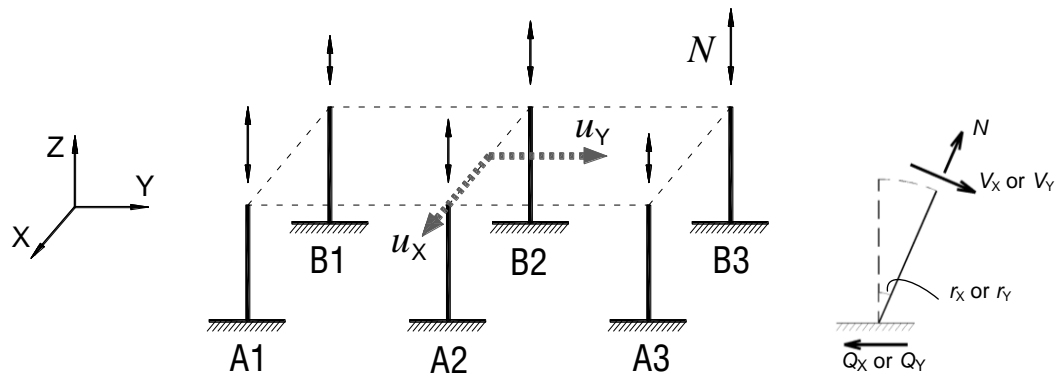
Figure 6.7 Story shear obtained by summation of particular column shear forces

Two types of perfectly bilinear elastoplastic and buckling fiber properties (noted as *"bilinear"* and *"buckling"* model, respectively) are selected for the comparison of analytical base shear response. Displacement control is applied in the analyses with the concept of examining the resisting capacity of different structural strengths under the similar deforming condition. Analytical results of story shear by two models applying the elliptical idealized load scheme (with story drift exceeding 0.02 rad) are shown in Figure 6.8. The story shear interaction surface [Figure 6.8(b)] shows the stable behavior of the bilinear model (represented by dashed line) after several cycles despite the yielding. In contrast, story shear capacity of the buckling model (represented by solid line) is reduced significantly cycle-by-cycle [Figures 6.8(c)–(e)] due to the deterioration caused by local buckling. The reduction of story shear capacity reflects the shrinkage of column yield surface.

(a) Displacement loading

(b) Story shear surface

(c)

(d)

(e)

(f)

(c), (d), (e), (f) Story shear hysteresis and time-history

Figure 6.8 Analytical results of story shear by two types of bilinear and buckling fiber hinge model applying the elliptical idealized load scheme.

(a) Displacement loading

(b) Story shear surface

(c), (d), (e), (f) Story shear hysteresis and time-history
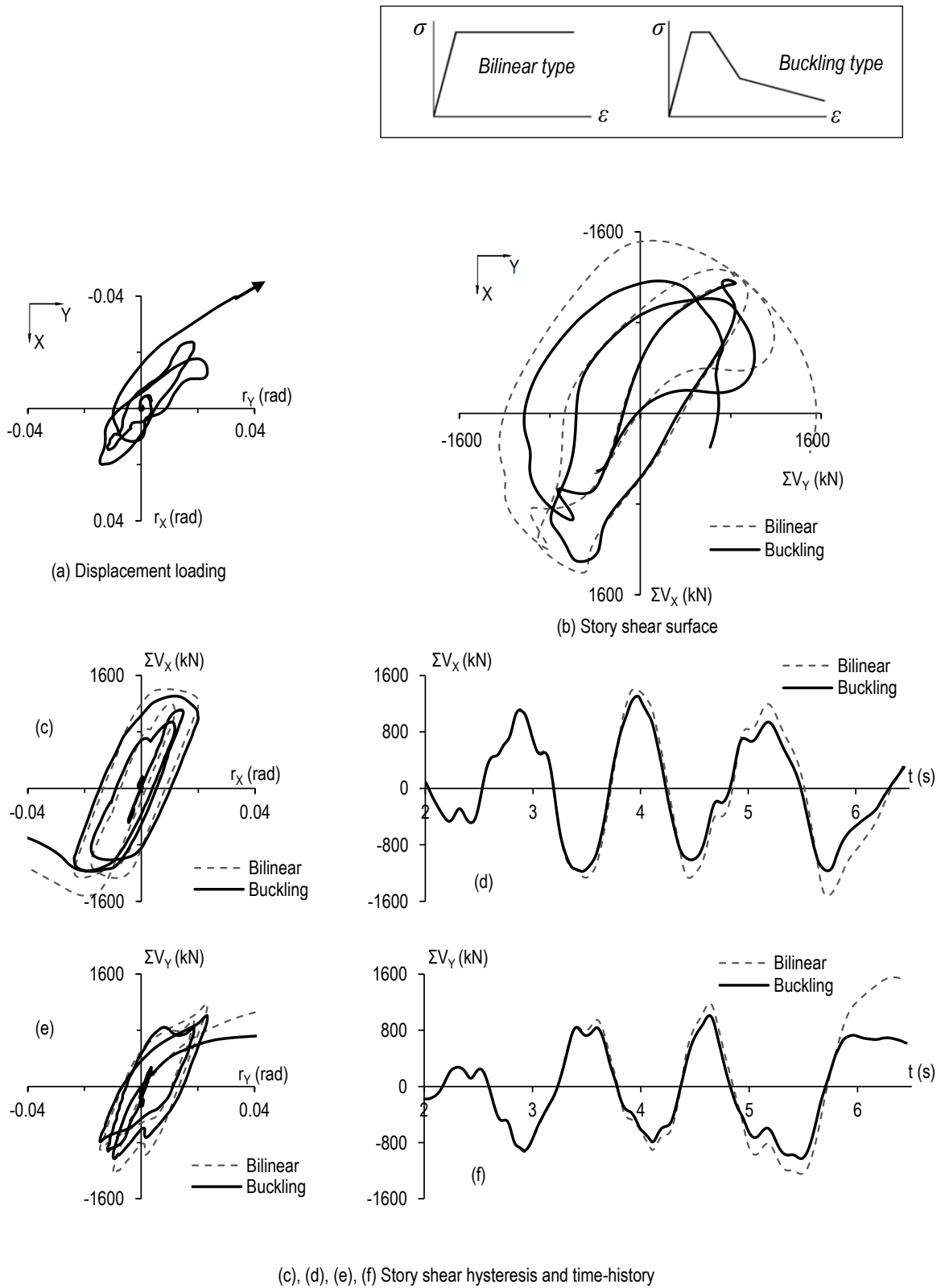
Figure 6.9 Analytical results of story shear by two types of bilinear and buckling fiber hinge model applying the Takatori load scheme.
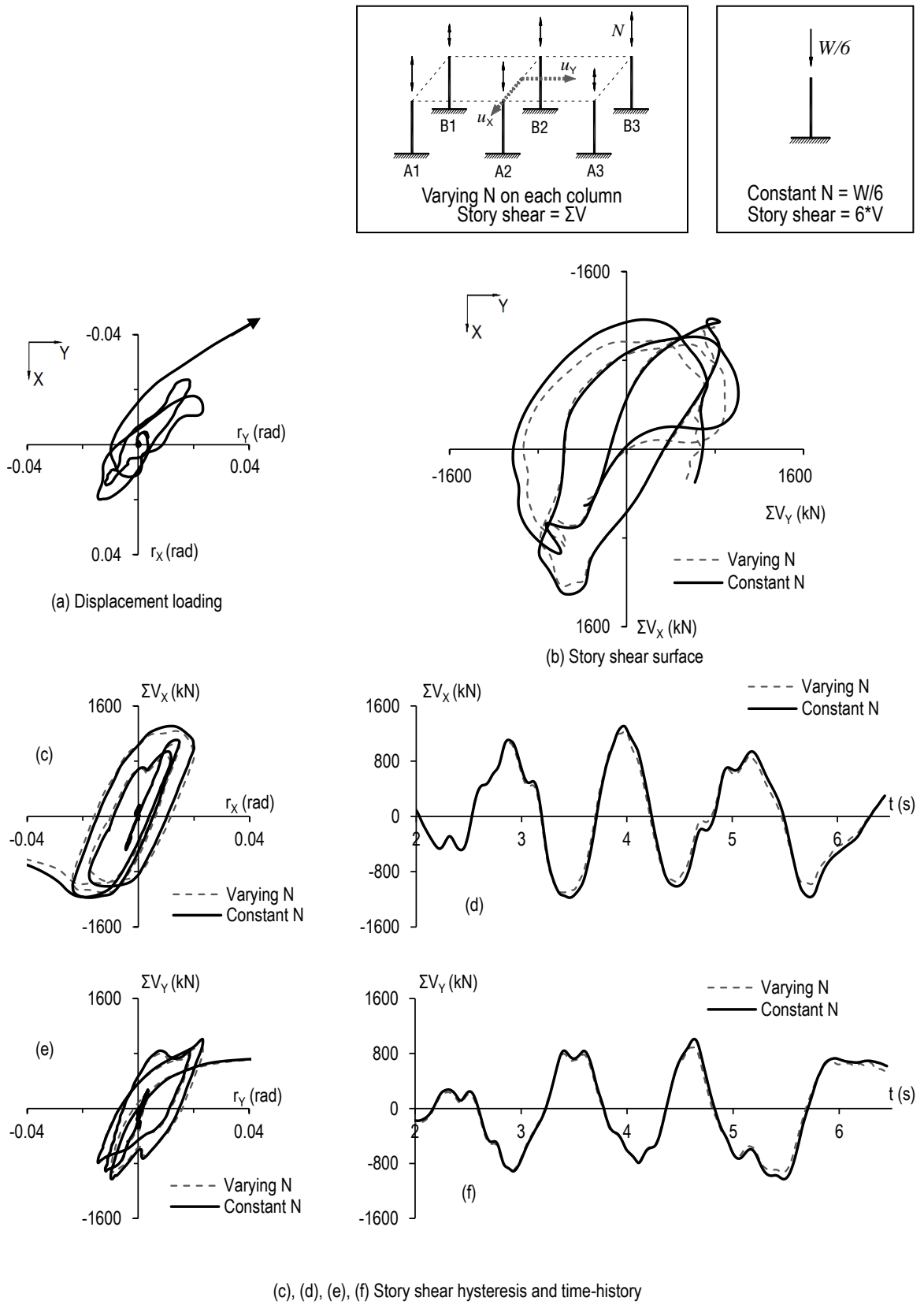
(a) Displacement loading

(b) Story shear surface

(c), (d), (e), (f) Story shear hysteresis and time-history

Figure 6.10 Comparison between the approaches considering constant average axial load and varying axial load per column.

Furthermore, the simulated results of story shear applying the displacement loading scheme derived from the frame shaking test are plotted in Figure 6.9, showing the similar reduction of story shear capacity with consideration of column's local buckling. Finally, Figure 6.10 compares the analytical story shear using the single cantilever column considering the average constant axial load (represented by solid line) with the one obtained by summation of member shear forces from six individual column models subjected to their own axial force histories as recorded in the test (represented by dashed line). The results show a fairly close agreement between two cases. It thereby suggests the applicability of the simplified analytical approach considering average constant axial load in predicting the building's dynamic responses.

6.5 Summary

This chapter characterizes for cyclic deteriorations of columns and soft story, on some aspects such as cyclic moment-deformation hysteresis shape, two-directional correlative deterioration, effect of varying axial load condition, and the soft story behavior.

- The fiber hinge element method simply specifies local properties of fibers but is able to control the global column moment-rotation hysteresis shape in good agreement with the experimental response. Although the method has different approach, it shows certain compatibility with the skeleton approach like Yamada *et al.* [40].

- The uniaxial-bending skeleton approach appears to hardly explain the moment response under random biaxial bending, because the individual skeleton curves of M_X and M_Y outrace the experimental envelop skeleton curve. Therefore, the study proposed a general rule for creating a mixed skeleton curve including both M_Y and M_X in order to interpret the two-directional correlative deteriorating sequence.

- Simulation results indicated that the fiber stress-strain responses under

the variation of axial force condition can automatically generate the column moment response, in compatibility with the skeleton approach.

- The cyclic story shear response involving two-directional column's deterioration due to local buckling can be approximated and closely simulated by the simplified analytical column model considering average constant axial load as the building weight divided by number of columns.

CHAPTER 7

CONCLUSION

Chapter 7

CONCLUSION

This dissertation reported a synthesis of experimental and analytical studies on the dynamic collapse test of a full-scale four-story steel building, addressing column behavior under varying axial load and biaxial bending moment, two-directional deteriorations due to local buckling, and consequent building collapse in soft-story manner. Some concluding remarks can be drawn as follows.

1. The Takatori input motion applied to the building specimen was predicted to be much more damaging in the Y direction than in the X direction based on the inelastic response spectra. This was consistent with the building response observed in the test, in contrast with the elastic response spectra predicting equal peak responses in both the X and Y directions.

2. Along with the increase in the scaled Takatori motions, the building's natural period also increased due to the yielding of frame components. Concentration of the drift in the first story occurred at the 60% Takatori level, involving significant inelastic deformation of the panel zones and columns. In contrast, the beams remained nearly elastic throughout the tests because their overstrength due to the composite action of the concrete slab is approximately 1.5 times the bare beam strength. At 100% Takatori motion level, the panel zones experienced strain hardening, and their capacity exceeded the local buckling capacity of the columns. As the story drift continued increasing, deterioration of the first-story columns occurred due to local buckling at the ends. Panel zones were unloaded

and returned to be elastic, causing more drift demand to the deteriorated first-story columns. A soft-story mechanism was initiated, and the building collapsed.

3. The 100% Takatori motion initially caused greater excitations in the X direction; however, the main shaking in the Y direction later determined the most significant damage to the structure and caused the largest translational displacement and collapse in that direction, as indicated by the inelastic spectra mentioned above. The sudden increase in the damage in the Y direction could be explained based on input energy, which depends on not only ground motion but also response velocity. Although the total accumulated input energies were very similar in both directions, a large amount of instantaneous input energy in the Y direction had to be dissipated within a short time by the frame with limited strength due to deterioration, thereby resulting in the rapid translational response of the first story. As the P-δ effect increased, the building consequently lost stability and eventually collapsed. Therefore, the maximum instantaneous earthquake input energy should be of greater interest in predicting structural response in seismic design.

4. Fiber hinge element that consists of fibers discretizing the column cross section was used to model the buckling zone at the column end, thereby simulating the building collapse. Compared to the continuum (shell or solid) elements, the fiber hinge element certainly is more convenient, but requires an empirical calibration considering the existing prediction rule for local buckling and FEM verification. However, the fiber hinge element is efficiently able to clarify the physics of accumulated column damage by characterizing the complex three-dimensional deformation of the local buckling behavior based on the approximate uniaxial stress-strain hysteretic relation of each fiber.

5. The fiber hinge element proved its advantage in the column analyses and was verified by the FEM simulations. Some static cyclic bending analyses

of cantilever columns considering different constant axial loads, as well as the nonlinear cyclic analyses of isolated particular cantilever columns applying two-directional lateral displacement histories and varying axial forces derived from the frame shake table tests, showed the efficiency of fiber hinge element method in simulating the column response under sophisticated axial load conditions. The analyses also clarified that any deterioration of column moment due to local buckling in the X direction, for instance, may limit the capacity of moment in the Y direction, and vice versa, which can be explained based on the shrinkage of moment yield surface.

6. The fiber hinge element method simply specifies local properties of fibers but is able to control the global column moment-rotation hysteresis shape in agreement with the experimental response, as well as compatibility with the skeleton approach. The cyclic story shear response involving two-directional column's deterioration due to local buckling can be approximated by the simplified analytical column model considering average constant axial load as the building weight divided by number of columns

7. Due to the effects of complex seismic loading on the columns, such as the alternately applied compressive and tensile axial load induced by overturning moment, additional high frequency axial force caused by vertical accelerations, and the cycle-by-cycle shifting of the biaxial bending moment's principal direction, a 3D analytical model as presented in this study could prove its appropriateness and advantages rather than 2D analytical approaches in simulating the building response in this full-scale three-directional collapse test.

8. The analytical building model utilizing fiber hinge elements closely simulated the building responses throughout small to large excitations, showing agreement with experimental responses on variety of quantities in not only global perspective such as story drift ratios, accelerations,

base shear, energy dissipation, but also local member responses. The analytical model was able to simulate the deteriorating behavior due to the coupled axial load and two-directional bending moment of particular columns whose relative magnitudes differ significantly by their locations. On the other hand, the accumulated deteriorations in accordance with the cycle-by-cycle shifting of the principal direction of the two-directional bending moments causing the earlier damage of column section in the X direction and subsequently reducing the resistant capacity in the Y direction were successfully reflected by the analytical model. The progress of column deteriorations was visualized and detailed via the stress-strain hysteretic relations of column-end fibers. The eventual soft-story collapse mechanism induced by the weakening of the first-story column ends was also well simulated.

9. The analytical model using fiber hinge element has some notable advantages compared to FEM approach, such as: simplification of modeling without too much concern on member discretization; time saving in running analysis; and convenient to obtain global responses (floor acceleration, velocity, displacement, etc.) as well as local responses (force, stress, deformation, etc.).

10. The analytical model can predict the hypothetical responses of the building which were not tested or measured in the experiment, such as the presence/absence of vertical input accelerations is predicted not to cause any significant effect on the building collapse response, or the correlative activity of two-directional input motions causes more damages to the structure than the single one. Moreover, the approach as adopted in this study combining simple line, truss, spring and fiber hinge elements rather than finite elements indicated the extent to which the simplified analysis can simulate the structural instability.

APPENDIX A

A.1 Load-deformation skeleton curve

The method of plotting skeleton curve (adopted from Yamada *et al.* [30]) is shown in Figure A.1 and described as follows: before the column reaches its maximum strength, the skeleton curve consists of the monotonic part and the consecutive parts after the Bauschinger parts in the successive cycles; after maximum strength was reached, the skeleton continues with the degrading part and unloading part until the load returns to zero, then again continues with the consecutive loading–degrading–unloading parts in the subsequent cycles.
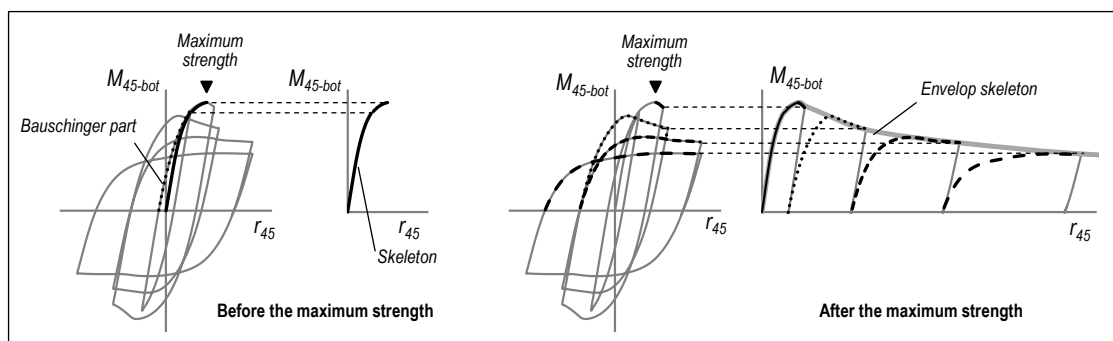

Figure A.1 Technique of plotting load-deformation skeleton curve adopted from [30].

A.2 FEM model properties

The FEM analytical model is shown in Figure A.2(a). The column body is divided with 4-node shell elements [38] while the loading jig at the top of column is done with 2-node rigid beam elements. Flat parts and curved corner parts in the cross section are divided into 8 elements and 4 elements respectively. In the longitudinal direction, the shell elements are arranged for the grid in the flat parts to become square except the top row. As a result, total numbers of nodes, shell elements and degrees of freedom are 2306, 2256, 12260. 2x2 Gauss integration on the surface and 7 Newton-Cotes integration in the thickness direction of each shell element are used.

It has been corroborated that the present mesh size is small enough to simulate local buckling behavior accurately though the detailed description is omitted. The column bottom is fixed, and both vertical force and horizontal constraint displacement are applied to the top of the model (Point A). For the material nonlinearity with complex hardening behavior like the Bauschinger's effect, the sublayer model [39] in which 14 virtual layers are considered at the above integration points is used to the model as shown in Figure A.2(b).

(a) FEM model

(b) Stress-strain curve by sublayer model
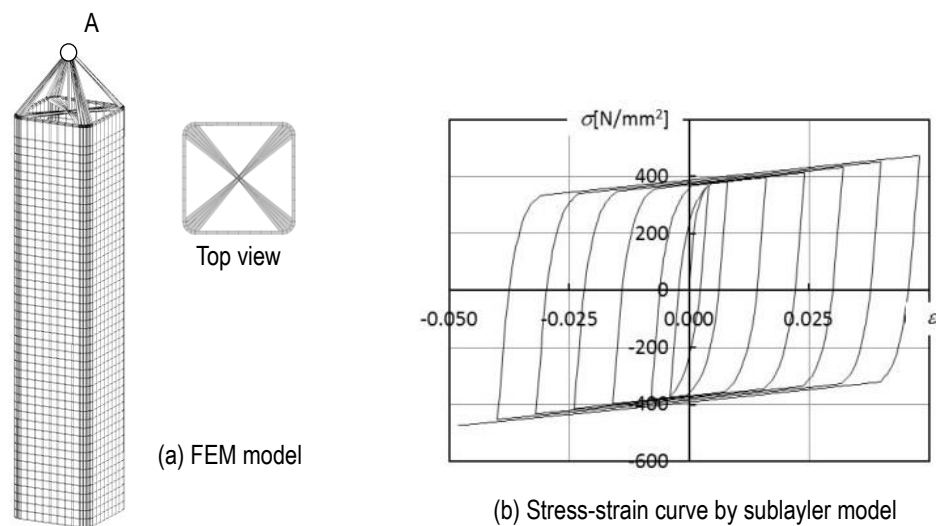
Figure A.2 Analytical model and material property in FEM.

A.3 Energy equations

The energy equation for a viscous damped n-story structure subjected to horizontal earthquake ground motion can be derived from the following equation of motion:

$$\mathbf{M}\ddot{\mathbf{u}}_{\mathbf{tot}} + \mathbf{C}\dot{\mathbf{u}} + \mathbf{f_s} = \mathbf{0} \tag{A1}$$

where $\mathbf{M}$, $\mathbf{C}$ and $\mathbf{f_s}$ represent the diagonal mass matrix, diagonal viscous damping matrix and restoring force vector, respectively. Note that $\mathbf{f_s}$ may be expressed as $\mathbf{Ku}$ for a linear elastic system ($\mathbf{K}$ is a diagonal stiffness matrix). The vector $\mathbf{u_{tot}} = \mathbf{u} + \mathbf{1}u_g$ represents absolute displacement in either the X or Y direction, in which the vector $\mathbf{u}$ corresponds to the relative displacement with respect to the shake table, $\mathbf{1}$ is a unit vector, and u_g is the shake table displacement. By letting $\ddot{\mathbf{u}}_{\mathbf{tot}} = \ddot{\mathbf{u}} + \mathbf{1}\ddot{u}_g$, Equation (A1) may be rewritten as

$$\mathbf{M}\ddot{\mathbf{u}} + \mathbf{C}\dot{\mathbf{u}} + \mathbf{f_s} = -\mathbf{M1}\ddot{u}_g \tag{A2}$$

Integrating Equation (A2) with respect to vector $\dot{\mathbf{u}}^{\mathrm{T}}$, we can obtain the energy equation

$$\int \dot{\mathbf{u}}^{\mathrm{T}}\mathbf{M}\ddot{\mathbf{u}}dt + \int \dot{\mathbf{u}}^{\mathrm{T}}\mathbf{C}\dot{\mathbf{u}}dt + \int \dot{\mathbf{u}}^{\mathrm{T}}\mathbf{f_s}dt = -\int \dot{\mathbf{u}}^{\mathrm{T}}\mathbf{M1}\ddot{u}_g dt \tag{A3}$$

expressed in terms of

$$E_k + E_d + (E_s + E_y) = E_{in} \tag{A3'}$$

where the first term on the left side of Equation (A3) is the kinetic energy (E_k):

$$E_k = \int \dot{\mathbf{u}}^{\mathrm{T}}\mathbf{M}\ddot{\mathbf{u}}dt = \int \sum_{i=1}^{n} \dot{u}_i m_i \ddot{u}_i dt = \frac{1}{2}\sum_{i=1}^{n} m_i \left(\dot{u}_i\right)^2 \tag{A4}$$

The second term on the left side of Equation (A3) is the energy dissipated by viscous damping (E_d). The third term is the sum of the energy dissipated by the recoverable strain energy (E_s) and yielding (E_y) in the structure. Note that $\mathbf{C}\dot{\mathbf{u}} + \mathbf{f_s} = -\mathbf{M}\ddot{\mathbf{u}}_{\mathbf{tot}}$ based on Equation (A1); therefore,

$$E_d + (E_s + E_y) = \int \dot{\mathbf{u}}^T \mathbf{C} \dot{\mathbf{u}} dt + \int \dot{\mathbf{u}}^T \mathbf{f_s} dt = \int \dot{\mathbf{u}}^T \left(\mathbf{C} \dot{\mathbf{u}} + \mathbf{f_s} \right) dt$$

$$= -\int \dot{\mathbf{u}}^T \mathbf{M} \ddot{\mathbf{u}}_{\mathbf{tot}} dt = -\int \sum_{i=1}^{n} \dot{u}_i m_i \ddot{u}_{tot,i} dt \qquad \text{(A5)}$$

The right side of Equation (3) is the earthquake input energy (E_{in}), where m_i is the lumped mass associated with the ith floor and $\dot{u}_i$ is the relative velocity at the ith floor.

$$E_{in} = -\int \dot{\mathbf{u}}^T \mathbf{M} \mathbf{1} \ddot{u}_g dt = -\int \sum_{i=1}^{n} \dot{u}_i m_i \ddot{u}_g dt \qquad \text{(A6)}$$

The energy dissipated by the hysteretic relationship between story shear and story drift deformation, namely, E_h, is calculated as follows

$$Q_{acc,i} = -\sum_{j=i}^{n} m_j \ddot{u}_{tot,j} \qquad \text{(A7)}$$

$$E_h = \sum_{i=1}^{n} \int Q_{acc,i} d \left(u_i - u_{i-1} \right) = \sum_{i=1}^{n} \int \left(-\sum_{j=i}^{n} m_j \ddot{u}_{tot,j} \right) \left(\dot{u}_i - \dot{u}_{i-1} \right) dt$$

$$= -\int \sum_{i=1}^{n} m_i \ddot{u}_{tot,i} \dot{u}_i dt = -\int \sum_{i=1}^{n} \dot{u}_i m_i \ddot{u}_{tot,i} dt \qquad \text{(A8)}$$

where, $Q_{acc,i}$ is the inertial force-based story shear associated with the ith story, and $(u_i - u_{i-1})$ is the corresponding story drift displacement.

Equations (A5) and (A8) prove that the total hysteretic and viscous dissipated energy E_h equals the sum of the second and third terms on the left side of Equation (A3). Based on these energy quantities, the following equation expresses the energy balance for the system:

$$E_{in} = E_k + (E_d + E_s + E_y) = E_k + E_h \qquad \text{(A9)}$$

APPENDIX B

This appendix presents the experimental behavior of composite beams throughout small to large excitation levels. Strain sensors are instrumented for all beams in the 2nd and 3rd floors, and for front-side beams in the 4th and roof floors (Figure B.1). Three locations of beam sections: *Y-directional exterior, X-directional exterior,* and *X-directional interior* are selected to show strain variation at the time of peak moment in Figures B.2–B.4, respectively. Moreover, the experimental neutral axis positions of those three beam section types at various shaking levels (estimated by least squares technique, Section B.1) are shown in Figures B.5–B.7, respectively.
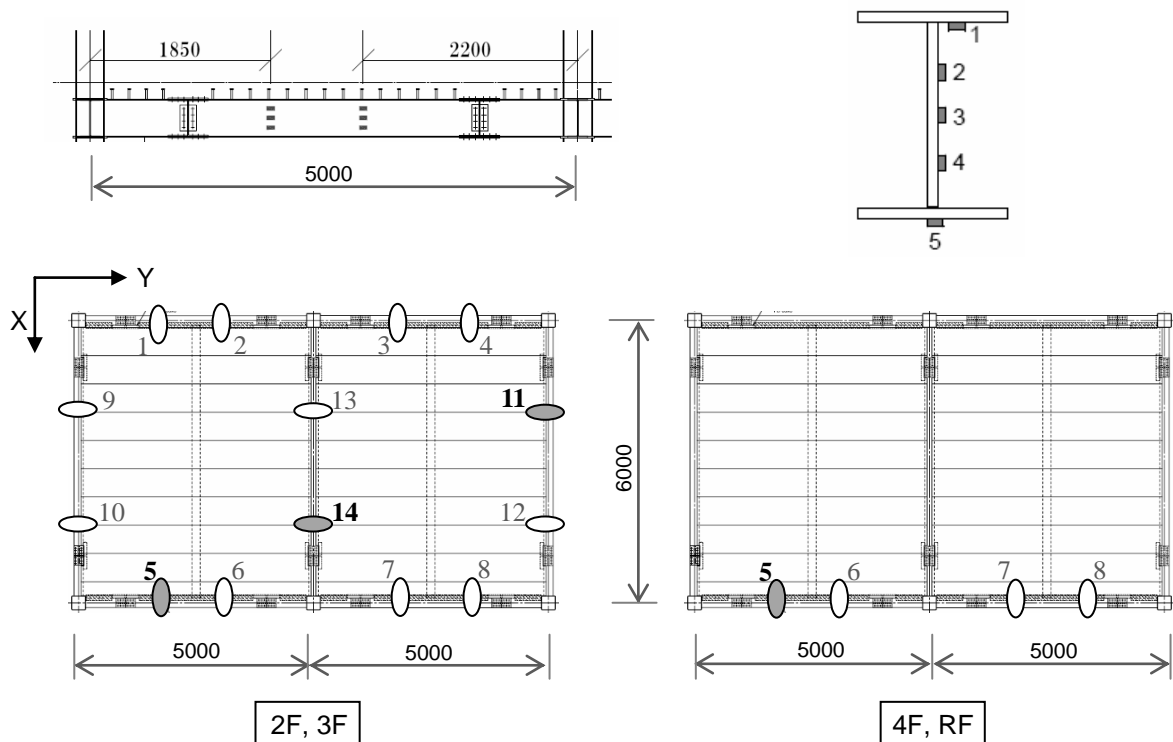
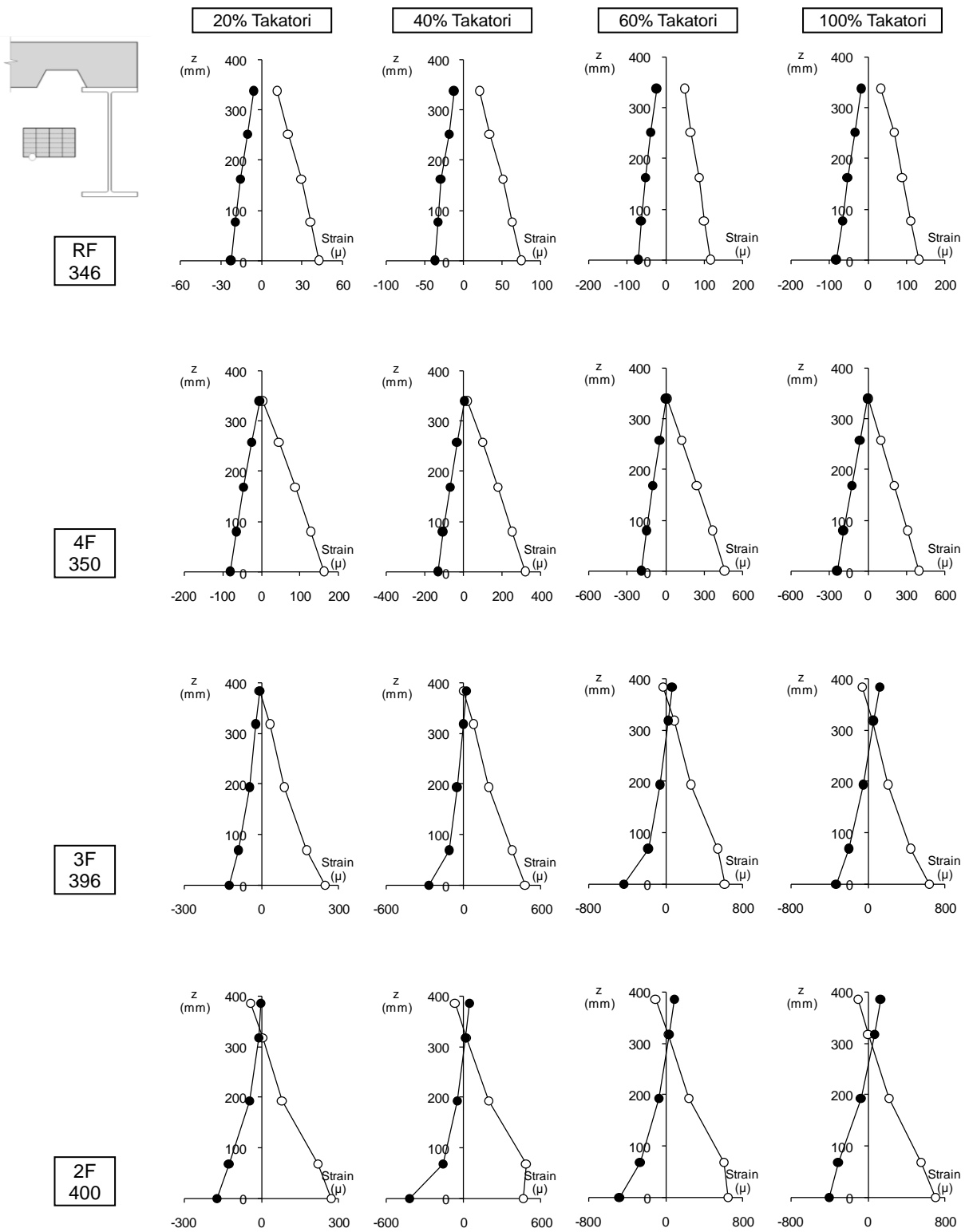**Figure B.1** Beam strain sensor allocation

Figure B.2 Beam strain variation at the time of peak moment (location #5 – exterior)
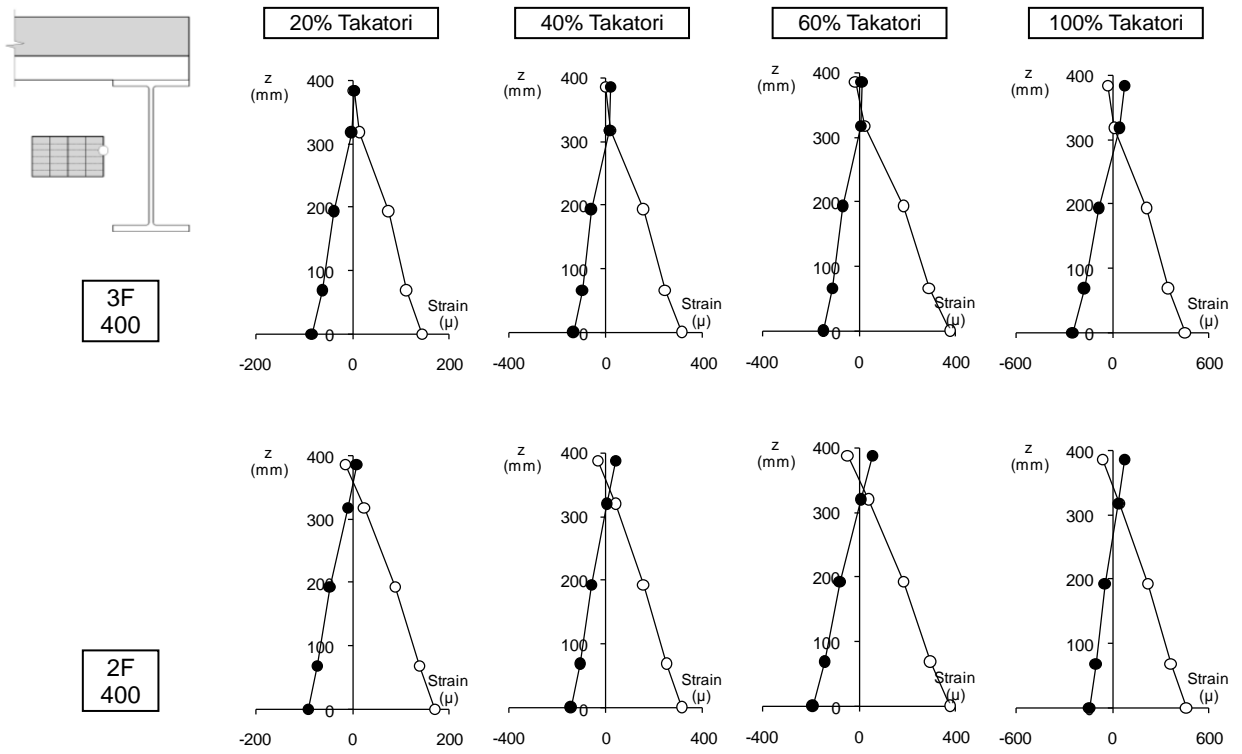
Figure B.3 Beam strain variation at the time of peak moment (location #11 – exterior)
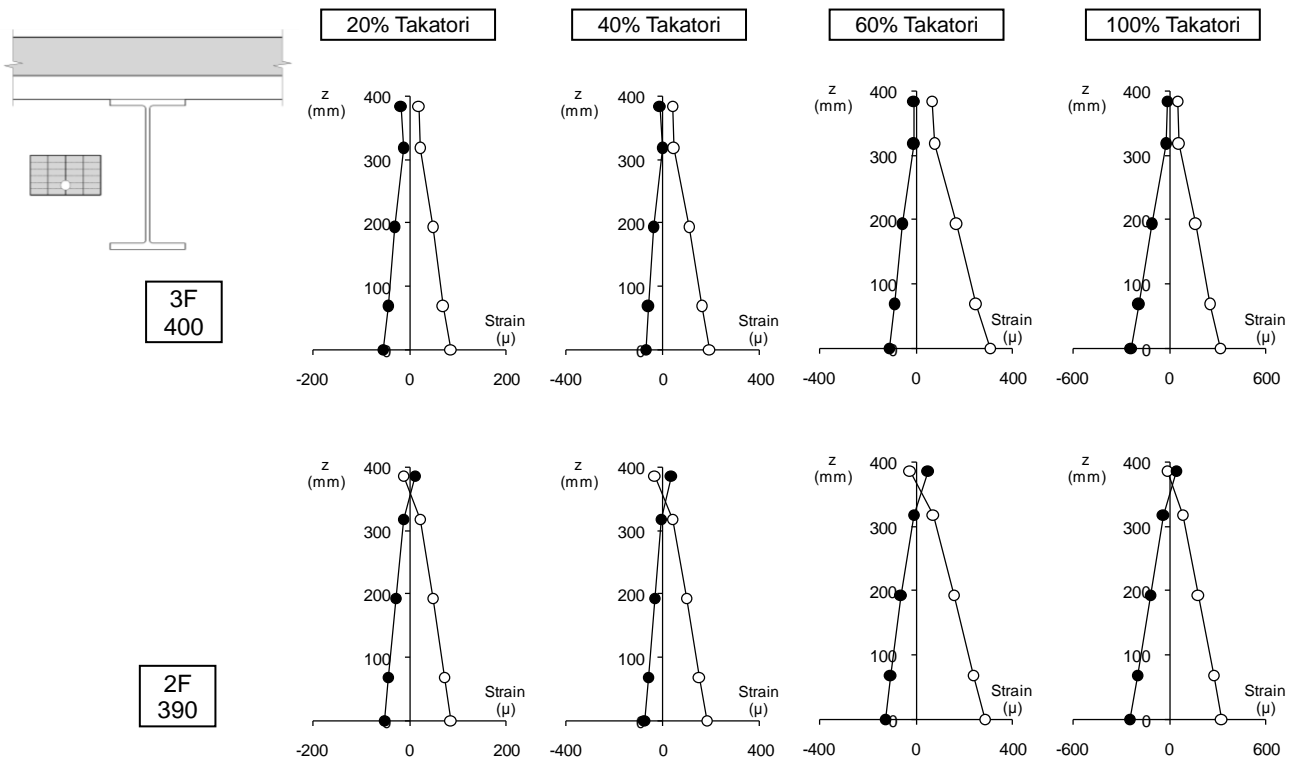
Figure B.4 Beam strain variation at the time of peak moment (location #14 – interior)
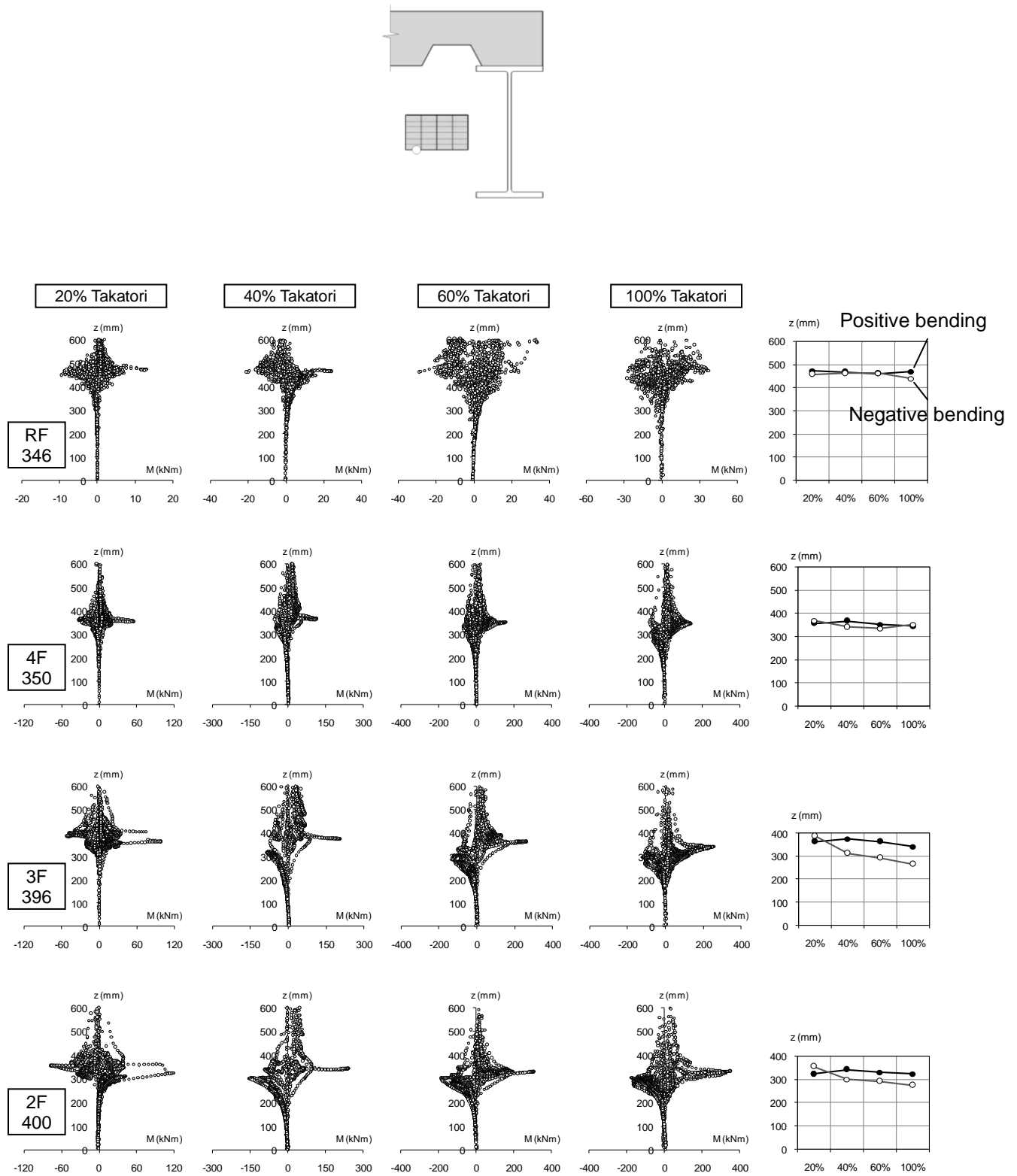
Figure B.5 Neutral axis position vs. beam moment, and neutral axis position at the time of peak beam moment (location #5 – Y-directional exterior).

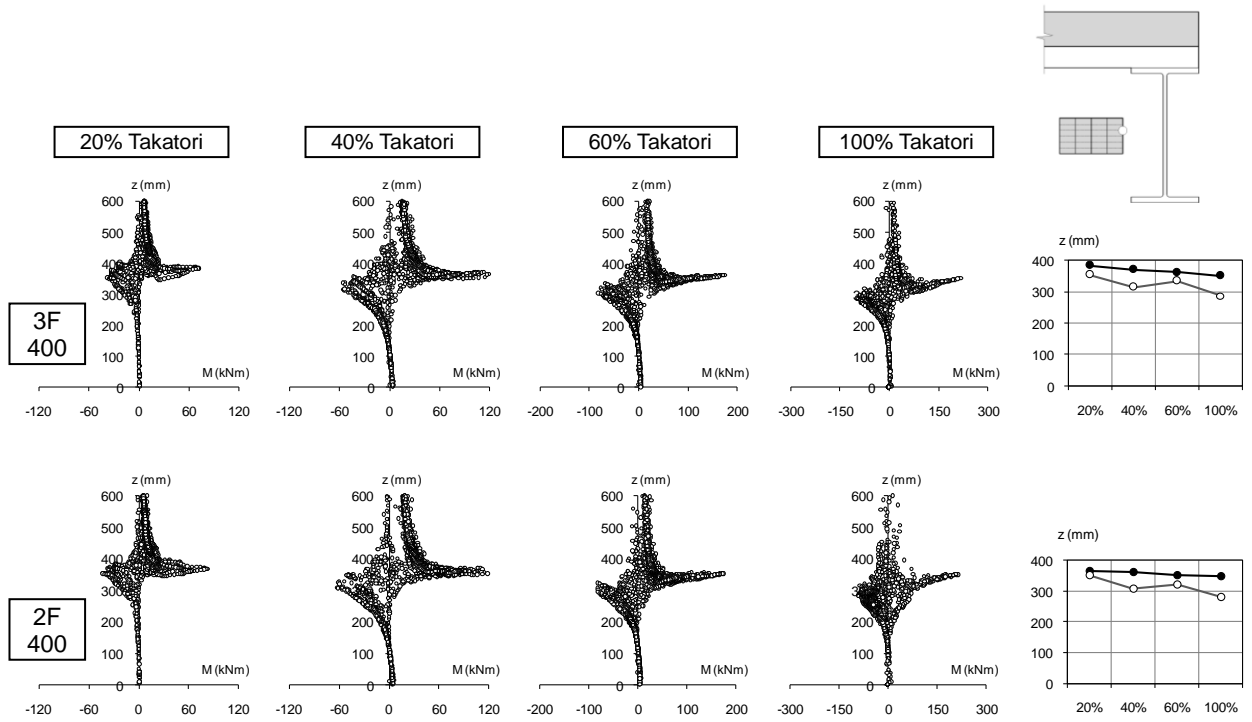**Figure B.6** Neutral axis position vs. beam moment, and neutral axis position at the time of peak beam moment (location #11 – X-directional exterior).
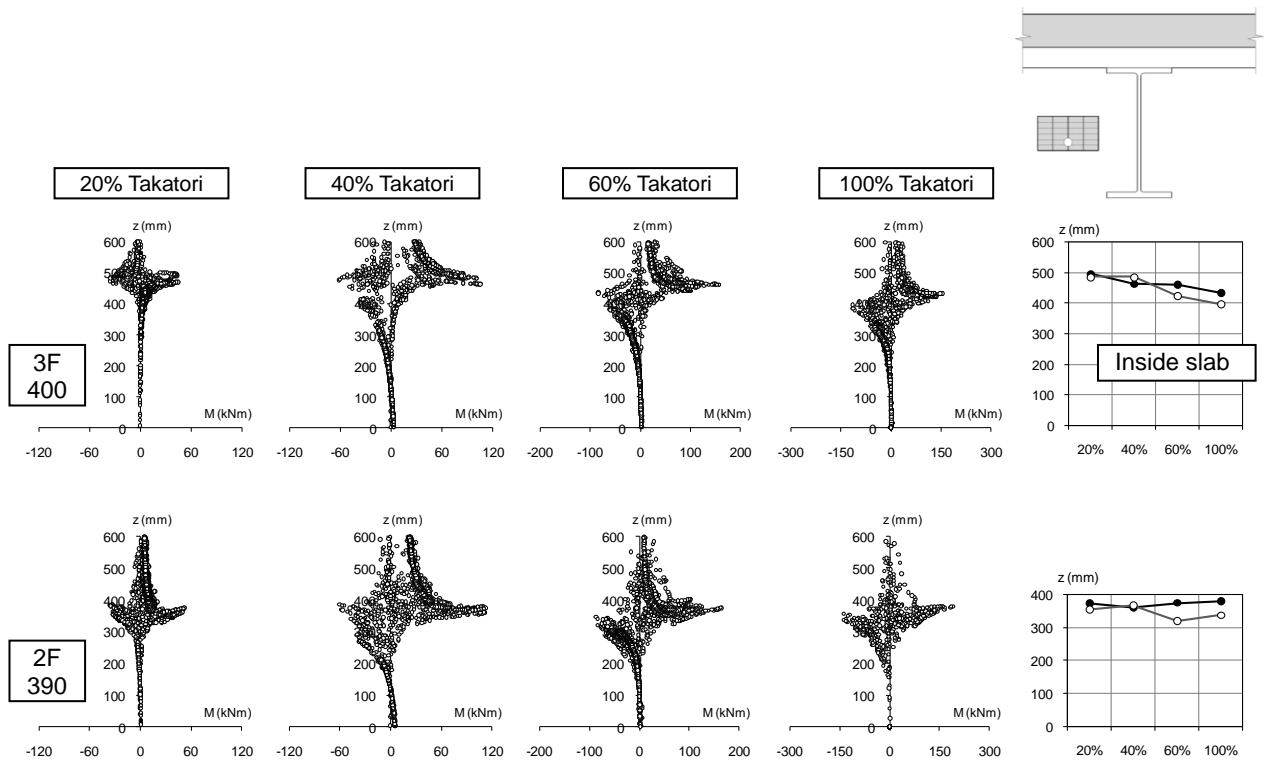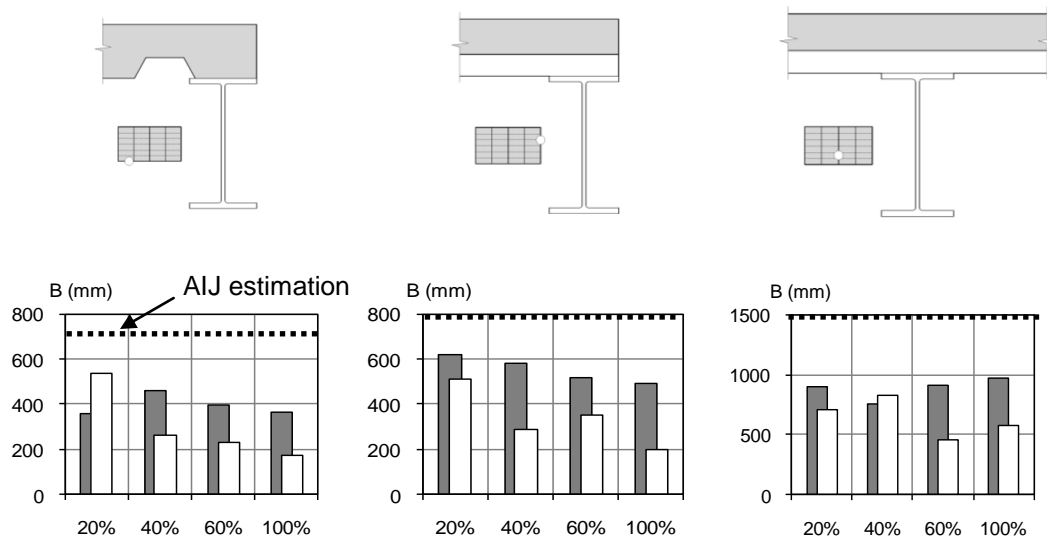

Figure B.7 Neutral axis position vs. beam moment, and neutral axis position at the time of peak beam moment (location #12 – X-directional interior).

Figure B.8 Effective width at the time of peak beam moment

Figures B.5–B.7 show that the experimental neutral axis position almost remained stable throughout the test. Neutral axis positions in case of negative bending were quite high, nearly same as in case of positive bending. Neutral axis positions of upper-floor beams were higher than those of lower-floor beams.

Figure B.8 shows the experimental composite beam's effective width (described in Section B.2) much smaller than the design value given by AIJ specification [37]. The beam sections in orthogonal direction with respect to the deck's longitudinal direction had larger effective width than those in parallel direction. For the same location of beam section, stiffness factors (defined as ratio I_{cn}/I_s, described in Section B.2) of upper-floor beams are larger than those of lower-floor beams (Table B.1).

Table B.1 Stiffness factor ϕ (location #5, all floors)

Excitation level	2F	3F	4F	RF
20%	2.44	2.81	3.05	3.08
40%	2.68	2.95	3.19	3.31
60%	2.53	2.81	2.99	2.98
100%	2.46	2.55	2.90	2.85

B.1 Experimental neutral axis estimated by least squares method
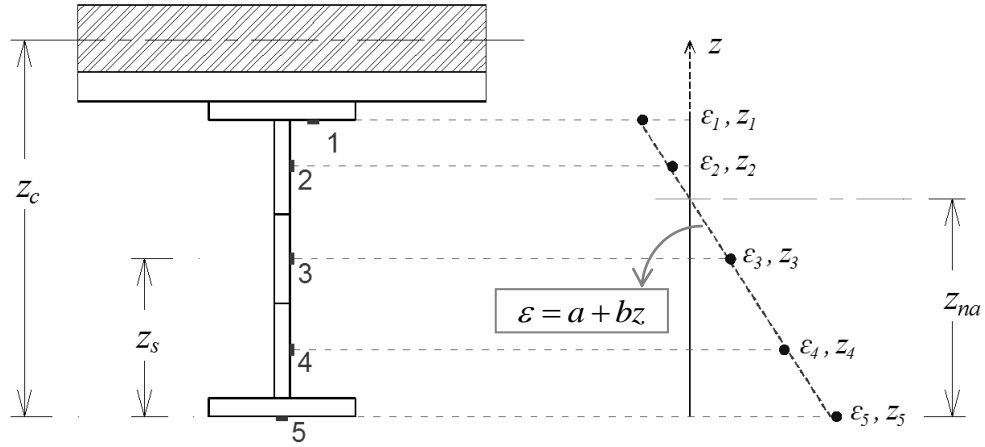
Figure B.9 Beam strain measured by sensors

The least-squares line uses a straight line

$$\varepsilon = a + bz \tag{B1}$$

to approximate the given set of data, (z_1, ε_1), (z_2, ε_2),..., (z_n, ε_n), where $n \geq 2$. The best fitting curve f(z) has the least square error, i.e.,

$$\Pi = \sum_{i=1}^{n}\left[\varepsilon_i - f(z_i)\right]^2 = \sum_{i=1}^{n}\left[\varepsilon_i - (a + bz_i)\right]^2 = \min \tag{B2}$$

Note that a and b are unknown coefficients whereas all z_i and ε_i are given. To obtain the least square error, the unknown coefficients a and b must yield zero first derivatives.

$$\begin{cases} \dfrac{\partial \Pi}{\partial a} = 2\sum_{i=1}^{n}\left[\varepsilon_i - (a + bz_i)\right] = 0 \\[4mm] \dfrac{\partial \Pi}{\partial b} = 2\sum_{i=1}^{n}z_i\left[\varepsilon_i - (a + bz_i)\right] = 0 \end{cases} \tag{B3,4}$$

Expanding the above equations, we have:

$$
\begin{cases}
\displaystyle\sum_{i=1}^{n}\varepsilon_i = a\sum_{i=1}^{n}1 + b\sum_{i=1}^{n}z_i \\[4mm]
\displaystyle\sum_{i=1}^{n}z_i\varepsilon_i = a\sum_{i=1}^{n}z_i + b\sum_{i=1}^{n}z_i^{\,2}
\end{cases}
\tag{B5,6}
$$

The unknown a and b can therefore be obtained, where $\displaystyle\sum\cdots$ stands for $\displaystyle\sum_{i=1}^{n}\cdots i$

$$
\begin{cases}
a = \dfrac{\left(\sum\varepsilon_i\right)\left(\sum z_i^{\,2}\right) - \left(\sum z_i\right)\left(\sum z_i\varepsilon_i\right)}{n\sum z_i^{\,2} - \left(\sum z_i\right)^{2}} \\[5mm]
b = \dfrac{n\sum z_i\varepsilon_i - \left(\sum z_i\right)\left(\sum\varepsilon_i\right)}{n\sum z_i^{\,2} - \left(\sum z_i\right)^{2}}
\end{cases}
\tag{B7,8}
$$

Then, the experimental neutral axis position z_{na} where $\varepsilon = 0$ can be obtained:

$$
z_{na} = -\frac{a}{b}
\tag{B9}
$$

B.2 Experimental effective width of composite beam
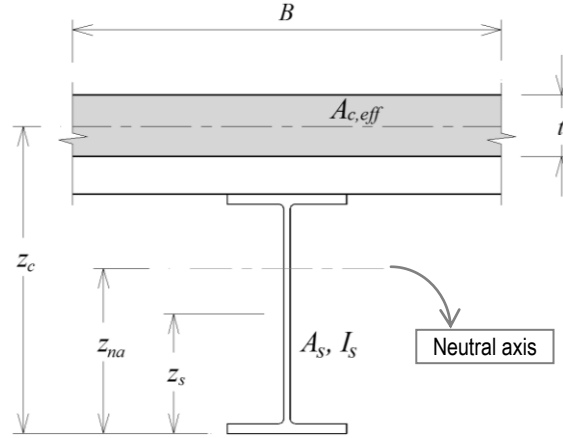
Figure B.10 Composite beam section

Neutral axis position z_{na} is defined as:

$$z_{na} = \frac{A_s z_s + A_{c,eff} z_c}{A_s + A_{c,eff}}, \quad A_{c,eff} = \frac{Bt}{n} \tag{B10,11}$$

where $n = E_s / E_c$ is the Young's modulus ratio of steel to concrete (n ≈ 7).

Effective beam width B is calculated from the experimental neutral axis position:

$$B = \frac{n A_s \left(z_{na} - z_s \right)}{t \left(z_c - z_{na} \right)} \tag{B12}$$

Moment of inertia can be estimated using the experimental B and z_{na}:

$$I_{cn} = \frac{1}{n} \left[\frac{Bt^3}{12} + Bt \left(D - z_{na} - \frac{t}{2} \right)^2 \right] + I_s + A_s \left(z_{na} - z_s \right)^2 \tag{B13}$$

Stiffness factor is defined as ratio of I_{cn} to moment of inertia of bare steel beam I_s:

$$\phi = \frac{I_{cn}}{I_s} \tag{B14}$$

REFERENCES

[1]   Kasai K, Ooki Y, Motoyui S, Takeuchi T, Sato E. E-Defense tests on full-scale steel buildings Part 1 - Experiments using dampers and isolators. *Proceedings of Structural Congress*, ASCE, Long Beach, 247-17, 2007.

[2]   Foutch DA, Goel SC, Roeder CW. Seismic testing of full-scale steel building - Part 1, *Journal of Structural Engineering* 1987; **113**(11): 2111–2129.

[3]   Lignos DG, Krawinkler H, Whittaker AS. Shaking table collapse tests of two scale models of a 4-story moment resisting steel frame. *Proceedings of the 14th World Conference on Earthquake Engineering*, Beijing, 2008.

[4]   Tada M, Ohsaki M, Yamada S, Motoyui S, Kasai K. E-Defense tests on full-scale steel buildings Part 3 - Analytical simulation of collapse. *Proceedings of Structural Congress*, ASCE, Long Beach, 247-19, 2007.

[5]   Nakamura Y, Uehan F, Inoue H. Waveform and its analysis of the 1995 Hyogo-ken Nanbu earthquake information (in Japanese). *Report No. 23d*. Railway Technical Research Institute, 1996.

[6]   Suita K, Matsuoka Y, Yamada S, Shimada Y, Tada M, Kasai K. Experimental procedure and elastic response characteristics of shaking table test – Complete collapse test of full-scale 4-story steel building Part 1 (in Japanese). *Journal of Structural and Construction Engineering, Transactions of AIJ* 2009; **635**:157–166.

[7]   Yamada S, Suita K, Matsuoka Y, Shimada Y. Elasto-plastic responses and process leading to a collapse mechanism – Complete collapse test of full-scale 4-story steel building Part 2 (in Japanese). *Journal of Structural and Construction Engineering, Transactions of AIJ* 2009; **644**:1851–1859.

[8]   Shimada Y, Suita K, Yamada S, Matsuoka Y, Tada M, Ohsaki M, Kasai K.
        Collapse behavior on shaking table test – Complete collapse test of full-scale 4-
        story steel building Part 3 (in Japanese). *Journal of Structural and
        Construction Engineering, Transactions of AIJ* 2010; **653**:1351–1360.

[9]   Matsuoka Y, Suita K, Yamada S, Shimada Y, Akazawa M, Matsumiya T.
        Evaluation of seismic performance of exterior cladding in full-scale 4-story
        building shaking table test (in Japanese). *Journal of Structural and
        Construction Engineering, Transactions of AIJ* 2009; **641**:1353–1361.

[10]   Yamada S, Shimada Y. Collapse behavior and ultimate earthquake resistance
        of weak column type multi story steel frame under bi-axial ground motion (in
        Japanese). *Journal of Structural and Construction Engineering, Transactions
        of AIJ* 2011; **662**:837–844.

[11]   Tada M, Tamai H, Ohgami K, Kuwahara S, Horimoto A. Analytical simulation
        utilizing collaborative structural analysis system. *Proceedings of the 14th
        World Conference on Earthquake Engineering*, Beijing, 2008.

[12]   Pan P, Ohsaki M, Zhang J. Collapse analysis of 4-story steel moment-resisting
        frames. *Proceedings of the 14th World Conference on Earthquake Engineering*,
        Beijing, 2008.

[13]   Miyamura T, Yamashita T, Akiba H, Ohsaki M. Dynamic FE simulation of
        four-story steel frame modeled by solid elements and its validation using
        results of full-scale shake-table test. *Earthquake Engineering & Structural
        Dynamics* 2014; DOI: 10.1002/eqq.2526

[14]   Isobe D, Han WS, Miyamura T. Verification and validation of a seismic
        response analysis code for framed structures using the ASI-Gauss technique.
        Earthquake Engineering & Structural Dynamics 2013; **42**(12):1767–1784.

[15]   Yu YJ, Tsai KC, Weng YT, Lin BZ, Lin JL. Analytical studies of a full-scale
        steel building shaken to collapse. *Engineering Structures* 2010; **32**:3418–3430.

[16]   Chen X, Han X, Jack C, Lin S, Mao G. Dynamic inelastic numerical simulation

for a shaking table test of a full scale steel moment frame structure based on OpenSEES. *Proceedings of the 14th World Conference on Earthquake Engineering*, Beijing, 2008.

[17]   Maison BF, Kasai K, Deierlein G. ASCE-41 and FEMA-351 evaluation of E-Defense collapse test. *Earthquake Spectra* 2009; **25**(4):927–953.

[18]   Lignos GD, Hikino T, Matsuoka Y, Nakashima M. Collapse assessment of steel moment frames based on E-Defense full-scale shake table collapse test. *Journal of Structural Engineering* 2013; **139**:120–132.

[19]   Uriz P, Filippou FC, Mahin SA. Model for cyclic inelastic buckling of steel braces. *Journal of Structural Engineering* 2008; **134**(4):619–628.

[20]   Spacone E, Filippou FC, Taucer FF. Fibre beam-column model for non-linear analysis of R/C frames: Part I. Formulation. *Earthquake Engineering & Structural Dynamics* 1996; **25**(7):711–726.

[21]   Liang QQ, Uy B, Liew JYR. Nonlinear analysis of concrete-filled thin-walled steel box columns with local buckling effects. *Journal of Constructional Steel Research* 2006; **62**(6):581–591.

[22]   Hajjar JF, Gourley BC. Representation of concrete-filled steel tube cross-section strength. *Journal of Structural Engineering* 1996; **122**(11):1327–1336.

[23]   Varma AH, Ricles JM, Sause R, Lu LW. Seismic behavior and modeling of high-strength composite concrete-filled steel tube (CFT) beam–columns. *Journal of Constructional Steel Research* 2002; **58**(5):725–758.

[24]   Uy B. Local and post-local buckling of concrete filled steel welded box columns. *Journal of Constructional Steel Research* 1998; **47**(1):47–72.

[25]   Kunnath SK, Heo Y, Mohle JF. Nonlinear uniaxial material model for reinforcing steel bars. *Journal of Structural Engineering* 2009; **135**(4):335–343.

[26]   Monti G, Nuti C. Nonlinear cyclic behavior of reinforcing bars including

buckling. *Journal of Structural Engineering* 1992; **118**(12): 3268–3284.

[27]   Architectural Institute of Japan. Japanese architectural standard specification JASS 6, steel work (in Japanese). AIJ: Tokyo, 1996.

[28]   Kasai K, Murata S, Kato F, Hikino T, Ooki Y. Evaluation rule for vibration period, damping, and mode vector of buildings tested by a shake table with inevitable rocking motions (in Japanese). *Journal of Structural and Construction Engineering, Transactions of AIJ* 2011; **670**:2031–2040.

[29]   Architectural Institute of Japan. Recommendation for design of connections in steel structures (in Japanese). AIJ: Tokyo, 2006.

[30]   Yamada S, Ishida T, Shimada Y, Matsunaga T. Cyclic loading test on RHS columns under bi-directional horizontal forces (in Japanese). *Journal of Structural and Construction Engineering, Transactions of AIJ* 2013; **683**:203–212.

[31]   Chopra KA. *Dynamics of Structures: Theory and Applications to Earthquake Engineering, 4th Edition.* Prentice Hall: Englewood Cliffs, New Jersey, 2012.

[32]   Uang C, Bertero VV. Evaluation of seismic energy in structures. *Earthquake Engineering and Structural Dynamics* 1990; **19**:77–90.

[33]   PERFORM. *Components and elements for PERFORM-3D and PERFORM-Collapse, Version 4.* CSI (Computers Structures) INC, 2006.

[34]   Black RG, Wenger WA, Popov EP. *Inelastic buckling of steel struts under cyclic load reversals.* UCB/EERC-80/40, Earthquake Engineering Research Center, Berkeley, California, 1980.

[35]   Yamada S, Akiyama H, Kuwamura H. Post-buckling and deteriorating behavior of box-section steel members (in Japanese). *Journal of Structural and Construction Engineering, Transactions of AIJ* 1993; **444**:135–143.

[36]   Maison BF. *PC-ANSR: A computer program for nonlinear structural analysis.*

National Information Service for Earthquake Engineering, NISEE/Computer Applications, University of California, Berkeley, 1992.

[37]   Architectural Institute of Japan. *Recommendation for limit state design of steel structures* (in Japanese). AIJ: Tokyo, 2010.

[38]   Dvorkin EN, Bathe KJ. A continuum mechanics based four-node shell element for general nonlinear analysis. *Engineering Computations* 1984; **1**:77–88.

[39]   Motoyui S, Taranishi M. Macroscopic evaluation method of the sublayer model composed perfect elasto-plastic layer for multi-axial stress field. *Journal of Structural and Construction Engineering, Transactions of AIJ* 2014; **695**:67–74.

[40]   Yamada S, Ishida T, Shimada Y. Hysteresis model of RHS columns in the deteriorating range governed by local buckling (in Japanese). *Journal of Structural and Construction Engineering, Transactions of AIJ* 2012; **674**:627–636.

[41]   Ishida T, Yamada S, Shimada Y. Analytical model of RHS columns under random bi-directional horizontal forces (in Japanese). *Journal of Structural and Construction Engineering, Transactions of AIJ* 2013; **691**:1631–1640.

[42]   Ishida T, Yamada S, Shimada Y. Simulation of hysteretic behavior of RHS columns under bi-directional horizontal forces and variable axial force (in Japanese). *Journal of Structural and Construction Engineering, Transactions of AIJ* 2014; **699**:641–650.

[43]   Yamada S, Akiyama H, Kuwamura H. Ultimate behavior of box-columns under varying axial force (in Japanese). *Journal of Structural and Construction Engineering, Transactions of AIJ* 1994; **461**:115–122.

[44]   Inoue I. *Theory and design of steel structures* (in Japanese), Kyoto University Press, 2003.